INKJET PRINTED AU NANOPARTICLE FILMS FOR MICROELECTROMECHANICAL SYSTEMS

by

ROBERT CHRISTOPHER ROBERTS

Submitted in partial fulfillment of the requirements

For the degree of Doctor of Philosophy

Dissertation Advisor: Dr. Norman C. Tien

Department of Electrical Engineering & Computer Science

CASE WESTERN RESERVE UNIVERSITY

August 2012

We hereby approve the thesis/dissertation of

Robert Christopher Roberts ,

candidate for the Doctor of Philosophy degree*.

Norman Tien
Prof. Norman C. Tien, Committee Chair

Mehran Mehregany
Prof. Mehran Mehregany, Dept. of Electrical Engineering & Computer Science

Christian Zorman
Prof. Christian Zorman, Dept. of Electrical Engineering & Computer Science

Arthur Heuer
Prof. Arthur Heuer, Dept. of Material Science & Engineering

Date: 8 June 2012

* We also certify that written approval has been obtained for any proprietary material contained herein.

To my parents

Table of Contents

List of Tables

List of Figures

Acknowledgements

I owe my deepest gratitude to Dr Norman Tien for serving as my mentor and advisor over these past six years. The insights and opportunities he provided me throughout my degree program have been transformational in my development. Dr Tien has a knack for knowing when to pose the right questions and inject fresh ideas, all while affording adequate freedom to develop these ideas into reality. The training and skills I have developed under his direction will serve me well as I look towards future endeavors.

I would also like to acknowledge and thank my committee members, Dr Arthur Heuer, Dr Mehran Mehregany, and Dr Christian Zorman, who each contributed greatly to my graduate training by dedicating their time to my research activities and personal development. I am grateful to each of them for allowing access to their unique expertise and providing me with ideas, advice, and research tools. I would further like to thank Dr Zorman for generously opening both his office and laboratory doors to me over the years, affording me a deep understanding of the microfabrication capabilities available at the university and abroad.

I am very grateful to each of the faculty in the Electrical Engineering and Computer Science department who have all been supportive in my research experience and have acted as teachers, role models, colleagues, and friends. Among them, I would like to acknowledge Dr Wen Ko, a true pioneer in engineering, who always offered insightful discussions to a young graduate student. I would also like to thank both Dr Joe Potkay and Dr Philip Feng, who allowed me unfettered access to observe their budding research careers, all while acting as outstanding role models and colleagues. I would

further like to acknowledge Dr Stuart Rowan and Justin Fox, who provided invaluable support during the ink synthesis phase of my research.

I am indebted to the many staff members at Case Western Reserve University who make the life of a researcher possible. Among them, I am grateful for all of the staff of the Electrical Engineering and Science department who provided daily support, logistics, and friendship over the years. I would especially like to thank Heidi Fanta, who kept my research career on track and on the agenda. I am grateful to Ron Jezeski and Ed Jahnke for their training, expertise, and support in the Microfabrication Laboratory, and David Greer in the Electronics Design Center. The staff of the Swagelok Center for Surface Analysis of Materials (SCSAM) should also be acknowledged for the training, expertise, and enthusiasm they supplied me. I must also acknowledge the many maintenance, custodial, and security personnel of the university who thanklessly made my research possible. Their friendly conversations during long nights and weekends were a welcomed break.

I offer sincere gratitude to the many colleagues in my research group who have served as excellent friends and collaborators including Dr Haixia Yu, Andojo Ongkodjojo Ong, Dr Dachao Li, and Dr Andy Liu. Over my many years at Case I was extremely lucky to have been continuously surrounded by very smart colleagues and friends who selflessly provided advice, expertise, and an extra hand when necessary. Among them, I would especially like to acknowledge Casey Kearns, Hari Rajgopal, Andrew Barnes, Dr Allison Hess, Jeremy Dunning, Dr Michael Suster, Dan Howe, Dr Jeremy Marvel, Dr Brian Taylor, Joe Zarycki, Shem Lachmann, Rocco Parro, Andy Allen, and Jaesung Lee.

I am forever grateful to my family who has shared in my graduate experience from the beginning and provided love and support throughout the process. My mother and father have both fostered, and endured, my development as an engineer. From the beginning they instilled into me the confidence, curiosity, and work ethic that have enabled me to achieve my dreams. I would also like to thank my brothers Patrick and Andrew for their unwavering support and humor throughout graduate school. Finally, I would like to thank Mariangela D'Agostino for the love, patience, and support she has shown me throughout my work; it has made all the difference.

Abstract

Jet Printed Au Nanoparticle Films For

Microelectromechanical Systems

Abstract

by

ROBERT C. ROBERTS

The field of microelectromechanical systems (MEMS) was born out of the integrated circuit (IC) industry by adapting semiconductor materials and their associated processing techniques to realize sensors and actuators which rely, in part, upon the mechanical characteristics of materials originally developed for their electrical properties. Unfortunately, semiconductor fabrication facilities can also act as a hindrance for MEMS development, as the per-unit cost of the methods and materials used are extremely high for small production volumes. Just as the original MEMS researchers found inspiration in the IC industry, one only needs to look at recent advances in printed electronics for potential opportunities in MEMS. Inkjet printing, due to its selective nature, represents one form of additive manufacturing with potential to enable microsystems manufacturing. The realization of microelectromechanical systems using additive inkjet printing requires a fundamentally different approach when compared to conventional subtractive microfabrication techniques.

One promising precursor ink for the development of gold microsystems consists of hexanethiol-encapsulated gold nanoparticles (Au-NP) suspended in α-terpineol. This Au-

NP ink requires post-deposition thermal steps which drive off the organic encapsulant material, and subsequently sinters the nanoparticles into a coherent conductive gold film. This dissertation develops the techniques and processes required to fabricate sintered inkjet printed gold films suitable for microelectromechanical systems.

A custom inkjet deposition system has been realized for the controlled patterning of Au-NP ink. The electrical and mechanical characteristics of printed gold films under varied sintering conditions are measured in order to gain insight to the appropriate sintering and deposition conditions necessary for printed microsystems. To enable multilayer devices, an aerosol deposited dielectric is studied for use in printed MEMS applications. Sintered gold films can exhibit process-dependent properties as shown by measurements of the temperature coefficient of resistance (TCR) for different printed films. A prototype jet-deposited gold microfabrication process is presented and demonstrated through the development of printed gold passive RF devices, demonstrating the viability of inkjet printed hexanethiol-encapsulated gold nanoparticle ink as a candidate precursor for gold microelectromechanical systems.

1. Inkjet Printing

1.1 – Motivation: Why Printed MEMS?

The field of microelectromechanical systems (MEMS) was born out the integrated circuit (IC) industry by adapting semiconductor materials and their associated processing techniques to realize sensors and actuators which rely, in part, upon the mechanical characteristics of materials originally developed for their electrical properties. The microfabrication techniques adapted by MEMS researchers greatly reduced the minimum repeatable feature size realizable for sensors and actuators, and offered the potential for the rapid scaling of manufacturing using semiconductor fabrication facilities. These attributes, among others, allowed for the creation of several disruptive technologies and the MEMS field had grown into a $6.9 billion industry by 2009 [1].

Unfortunately, semiconductor fabrication facilities can also act as a hindrance for MEMS development, as the per-unit cost of the methods and materials used are extremely high for small production volumes. As a result, only a handful of MEMS markets currently offer the demand necessary for cost effective commercialization, namely the automotive, cellular telecommunications, and video display industries. This hurdle poses a great challenge for MEMS practitioners, as it limits the number of potential markets, and necessitates high volumes to achieve profitability. Therefore, alternative microfabrication techniques which can lower production costs are needed, as this will enable the commercialization of MEMS devices at smaller production volumes and open up many new opportunities.

Just as the original MEMS researchers found inspiration in the IC industry, one only needs to look at recent advances in electronic manufacturing for potential opportunities in

MEMS. The field of *printed electronics* has emerged to greatly lower the production cost of electronics for lower performance applications such as displays and RFID tags [2, 3]. Printed electronics are manufactured using one or more printing techniques (inkjet, screen printing, gravure, flexography, etc.) which selectively deposit conducting, insulating, and semiconducting materials onto a substrate into patterned structures and devices [4]. Furthermore, printing-based deposition is typically performed at ambient or mildly elevated temperatures, enabling the use of low-cost flexible polymeric substrates. These attributes of printed electronics greatly lower fabrication costs, making them highly attractive for many electronics applications. This is supported by the fact that the printed electronics field is rapidly expanding and is expected to grow from $200 million in 2010, to almost $2 billion by 2015 [5].

Inkjet printing, due to its selective nature, represents one form of additive manufacturing. The term *additive manufacturing* refers to a manufacturing process or processes which selectively form raw material into a final product or component. In contrast, many traditional machining techniques are forms of *subtractive manufacturing*. With subtractive techniques, manufacturing begins from an oversized volume of bulk material and portions of the bulk are subsequently removed to form the final product. For complex products, 90% of the starting material may end up as waste, greatly increasing manufacturing costs [6].

One popular additive manufacturing technique for macroscale mechanical components is fused deposition modeling (FDM) which sequentially fuses patterned molten polymer layers together to form three dimensional structures [7]. This technique is commonly referred to as rapid prototyping or 3-D printing, as it allows a user to

quickly go from computerized design file to completed mechanical component. Another technique, selective laser sintering (SLS) can be used to directly form metal and ceramic structures from a computer model by successively sintering patterned layers together from a precursor material via laser [8]. With both techniques, the raw material used in manufacturing is minimized, reducing associated material costs. Further, as products are manufactured directly from a computer model, designs can be rapidly customized to meet evolving market needs without expensive retooling [6].

Recently, there has been keen interest in the United States to revitalize its manufacturing capabilities in order to remain competitive globally. As a result, The President's Council of Advisors on Science and Technology (PCAST) has issued a report recommending this be accomplished though innovations in advanced manufacturing, which they define as [9]:

> *…a family of activities that (a) depend on the use and coordination of information, automation, computation, software, sensing, and networking, and/or (b) make use of cutting edge materials and emerging capabilities enabled by the physical and biological sciences, for example nanotechnology, chemistry, and biology. This involves both new ways to manufacture existing products, and especially the manufacture of new products emerging from new advanced technologies.*

The recommendation from PCAST squarely places additive manufacturing as an attractive potential paradigm to ensure future manufacturing innovation in the United States. Further refinement and maturation of technologies such as selective laser sintering and fused deposition modeling will create new manufacturing capabilities with the potential to reduce costs and increase manufacturing agility for macroscale mechanical

products.

While the field of microelectromechanical systems currently enjoys a more than $6.9 billion market using conventional techniques, manufacturing costs have driven many facilities overseas. Just as there is a need to pursue innovation in advanced manufacturing for mechanical components, alternative microfabrication technologies should be developed to reduce costs and increase agility to ensure domestic relevance in the manufacturing of MEMS. Therefore, the advancement of inkjet printed fabrication for microelectromechanical systems is a prime opportunity to ensure further manufacturing innovation in the United States.

Just as the traditional MEMS designers took inspiration from the materials and techniques developed for the IC industry, the field of printed MEMS needs only to examine the growing area of printed electronics [10]. The emerging materials and processes from the printed electronics industry offer great potential for MEMS to similarly lower cost. Many MEMS devices rely solely upon surface micromachining, depreciating the importance of the substrate, making them well suited for migration over to an inkjet printed manufacturing scheme. Furthermore, as printed electronic devices continue to grow in popularity and complexity, so will the need for compatible sensors and actuators in order to meet consumer demand for low-cost complex electronic systems. Just as required by conventional MEMS, in order to realize printed microfabricated devices as a viable advanced additive manufacturing technology, further study of the electromechanical properties of printed electronic materials is necessary to enable viable printed MEMS design and fabrication.

1.2 – Subtractive versus Additive Manufacturing for MEMS

The realization of microelectromechanical systems using additive inkjet printing requires a fundamentally different approach when compared to conventional subtractive microfabrication techniques. Conventional MEMS microfabrication uses processes such as sputtering, chemical vapor deposition (CVD), and oxidation to form a conformal layer of material onto a substrate [11, 12]. A masking material is then applied onto the conformal layer and patterned using lithography. Next, the masked substrate is exposed to either a dry or wet chemical etchant, which selectively removes any material not protected by the masking layer. The masking material is then removed as the process is repeated for successive layers of material. Figure 1 illustrates the cross-sectional view of a simple MEMS cantilever structure fabricated using both conventional subtractive methods and additive inkjet printing to demonstrate the stark contrast between the two manufacturing paradigms.

With conventional manufacturing, a conformal sacrificial material (red) is deposited onto a substrate and then a masking material (blue) is lithographically patterned onto it. The sacrificial material is then etched, removing any material not protected by the mask. After etching, the mask is removed and the process repeats for a second device layer (gold). Here, a second mask is required to apply a different pattern before the device layer is etched. Once the device layer is patterned, the second mask is also removed from the device. Finally, the sacrificial layer is etched away yielding a conventionally microfabricated cantilever beam. This subtractive process requires nine process steps and two lithographic masks. A cantilever-based hydrogen gas sensor fabricated using conventional micromachining techniques is detailed in Appendix A.

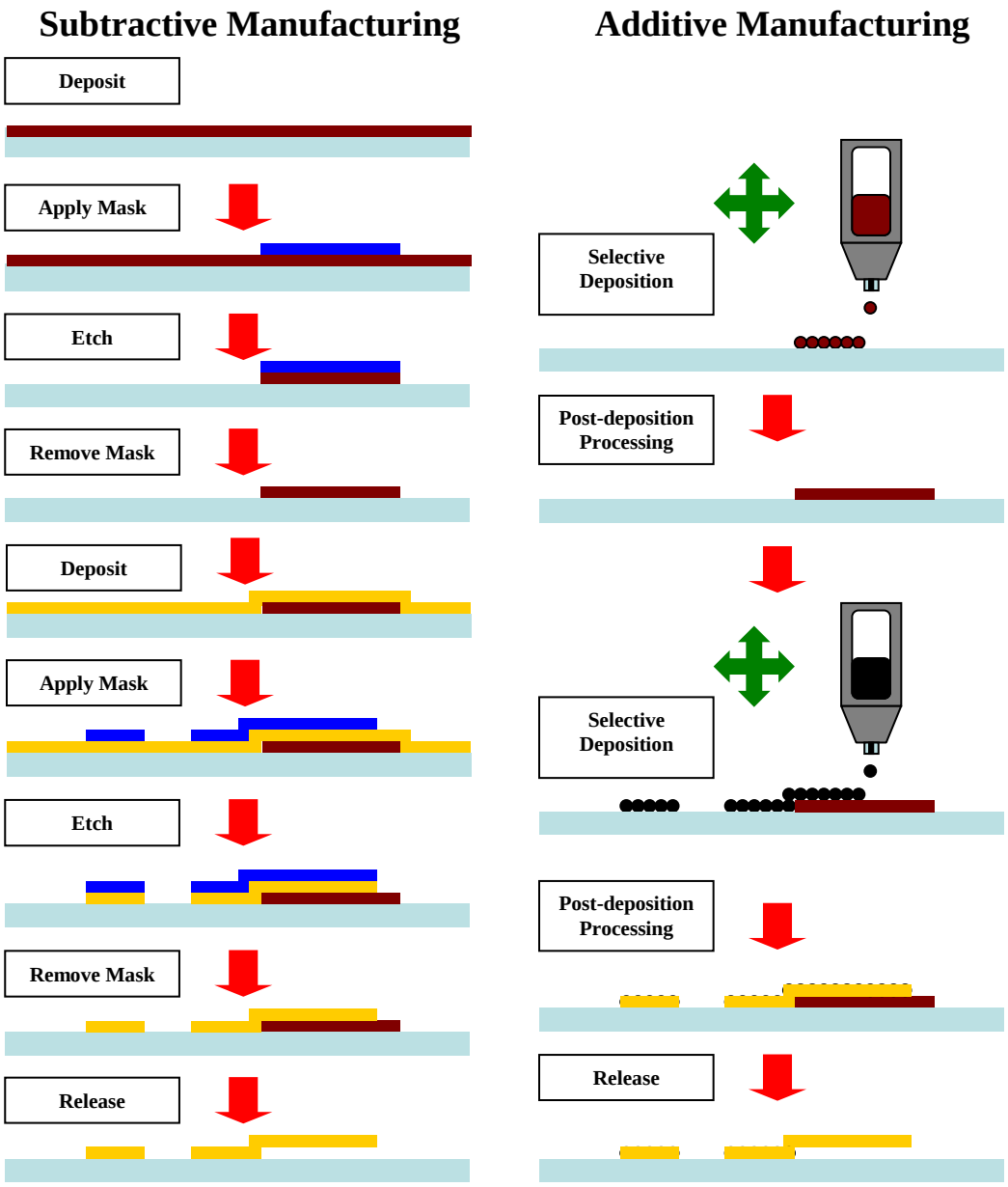

Figure 1 - Subtractive versus Additive manufacturing: Prototype MEMS cantilever process flow.

In contrast, to realize a cantilever using additive inkjet printing, five process steps are necessary. First, a sacrificial material (red) is selectively deposited into its desired geometry. Once deposited, this material is processed to solidify the material. Next, the

device layer material (black) is selectively deposited onto the substrate. This material must also be processed (black → gold) to render desirable material properties. Finally, the patterned sacrificial material is etched away to yield an inkjet-printed cantilever structure. As inkjet printing is entirely digitally computer controlled, no lithographic masks are required during manufacturing. Figure 1 also demonstrates that vastly different precursor materials may be needed to build printed microfabricated structures. The success of inkjet printing as a microfabrication technology hinges, in part, on the formulation of jettable inks which can be transformed into usable electrical and mechanical materials. Before exploring candidate inks for microfabrication, however, it is important to understand the inkjet printing process in more detail.

1.3 – Inkjet Printing Basics

For the purposes of this document, the generic term *inkjet printing* refers specifically to drop-on-demand inkjet printing technology. Drop-on-demand printing offers many advantages over competing printing techniques as an ink droplet is only generated when needed for deposition. This results in far less wasted ink and allows for motion synchronized droplet deposition, desirable traits for developing microfabricated devices.

In inkjet printing an ink is dispensed from a print head, which contains one or more print nozzles, each individually computer controlled to dispense an ink droplet on command. The print head is typically mounted onto some form of robotic motion stage, enabling the printing of patterned structures. For large substrates, such as paper, the print head is often made to raster scan across the substrate while the substrate feeds underneath the print head. A simpler approach suitable for small substrates is to fix the print head while moving the substrate underneath. This fixed approach is used herein, as it greatly

simplifies operation.

There are two types of drop-on-demand inkjet print heads found commercially; thermal and piezoelectric [13]. Thermal inkjet utilizes a brief thermal spike which causes a portion of the ink solvent to vaporize, generating a bubble which ejects ink out of an adjacent nozzle. While lower cost, thermal inkjet heads offer less control over droplet ejection, and expose the ink to repeated thermal spikes, making them undesirable for temperature sensitive nanoparticle based inks.

On the other hand, piezoelectric inkjet heads eject ink by applying a voltage to a piezoelectric material, which typically deforms the ink channel, forcing said ink out of the nozzle. This method is preferable for our application for two reasons. First, the ink does not experience heating, which could degrade the nanoparticles and cause nozzle clogging. Second, complex voltage waveforms can be applied to the piezoelectric material, giving far greater control of ink ejection, resulting in higher quality droplet ejection [14]. A piezoelectric print head is used in this work, and is detailed in Chapter 3.

1.4 – Central Hypothesis

A precursor ink consisting of hexanethiol-encapsulated gold nanoparticles (Au-NPs) suspended in α-terpineol has been identified from the printed electronics literature as a candidate printed gold MEMS structural material. This Au-NP ink requires post-deposition thermal steps which drive off the organic encapsulant, and subsequently sinters the nanoparticles into a conductive gold film. This dissertation develops the techniques and processes required to form this Au-NP precursor ink into gold films suitable for microelectromechanical systems development. While thin-film printed structures using this Au-NP ink have been demonstrated in the literature as conductors

for electronics, no research has been found on the process conditions required to yield continuous gold films with suitable electrical and mechanical characteristics for microfabricated sensors and actuators. It is hypothesized that the physical and mechanical properties of the Au-NP based gold films are dependent on the post-deposition thermal steps, and that care must be taken to yield structurally reliable and repeatable gold films for MEMS. Therefore, it is necessary to develop suitable deposition and sintering parameters for hexanethiol-encapsulated gold nanoparticle inks which yield coherent gold films suitable for printed microsystems.

This will be accomplished by first synthesizing the Au-NP ink and building a suitable inkjet deposition system. After finding stable jetting parameters, the electrical and mechanical characteristics of gold films formed under varied sintering conditions will be measured and compared in order to gain insight to the appropriate sintering and deposition conditions necessary for printed microsystems. A complementary dielectric material must be identified and developed to complement the gold film. Compatibility with the Au-NP sintering process must be demonstrated as this material will enable multiple the isolated metal layers often required in MEMS. Finally, a prototype hexanethiol-encapsulated gold nanoparticle inkjet microfabrication process must be developed and demonstrated through the realization of functional printed microsystems, to validate the suitability of the sintered gold films towards, and enable future development of inkjet-printed gold microelectromechanical systems.

1.5 – Organization of Document

The remainder of this document is organized to guide the reader through the many aspects of inkjet printed gold microsystems explored in this research. Chapter 2 first

provides a literature review of relevant topics to contextualize this work and identify the current state of the art. Chapter 3 then introduces the hexanethiol gold nanoparticle ink and custom inkjet deposition system developed for this work, along with the process development performed to enable stable jet printing of the Au-NP formulation. A novel aerosol-based high-temperature enamel is introduced in Chapter 4 for use as a structural dielectric material and to act as substrate pretreatment for printed metal MEMS. Chapter 5 explores the sintering of hexanethiol gold inks and examines the electrical and physical characteristics of the resulting gold films as they related to sintering conditions. Sintered gold films on Corning 0215 glass were found to be interesting microstructures and the temperature coefficient of resistance (TCR) of this film is explored in Chapter 6 toward printed gold temperature sensors. Now that suitable process conditions have been identified to enable printed gold microstructures on enamel, Chapter 7 presents a prototype printed gold MEMS fabrication process using shadow-masked aerosol dielectric layers. This fabrication process is demonstrated through the realization of passive radio frequency (RF) components towards more complex microelectromechanical systems. Finally, Chapter 8 gives concluding comments on this work and lays out future work which should be performed to advance the area of inkjet-printed microelectromechanical systems.

2. Review of the Literature

This chapter presents a literature survey on the two important topics with relevance to this dissertation. A survey of the small but growing field of inkjet printed MEMS is presented to show the state of the art in printed MEMS process techniques. Next, the published literature pertaining to alkanethiol-encapsulated gold nanoparticles as they pertain to use as an ink for electronic or electromechanical structures is examined to contextualize the current understanding of the process techniques and resulting material properties of the resulting gold films.

2.1 – Inkjet Printed MEMS

To date, most inkjet-printed microstructures are simple polymeric [1, 2] or metal [3] arrays for use in manufacturing of larger components. The inkjet printing of solder droplets has been developed for microelectronic manufacturing [4]. Inkjet printing is popular for the deposition of functional materials and has been used to realize solid state sensors such as aqueous ammonia sensors [5], or gold chemiresistors [6].

The vast majority of more complex inkjet-patterned microfabricated metal structures are for conductors in printed electronics such as the work performed by C.M. Hong at Princeton, who developed a copper nanoparticle deposition process [7,8,9]. Silver has been studied extensively for printed electronics [10, 11], and its use has been incorporated in polymer MEMS switches [12]. Gold has recently proven popular for metal patterning of printed conductors, such as the work to build all-printed RFID tags by Subramanian *et al*; this will be expanded upon in the next section [13].

Fuller *et al.* first demonstrated the concept of inkjet-printed metal MEMS when they

used colloidal gold and silver inks to fabricate a variety of microfabricated structures in 2002 [14]. They deposited their metals at 300ºC and used poly-methyl-methacrylate (PMMA) as a sacrificial material, and a polyketone resin as an insulator. Using these materials they demonstrated a planar resonant inductive coil, and an electrostatic drive motor. The first inkjet printed MEMS actuators were presented in the form of both vertical and horizontal gold "heatuators" which deformed as current passed through them.

More recently, Lam, *et al.* have demonstrated cantilevers and a pinwheel accelerometer proof mass using inkjet-printed colloidal silver ink and a laser trimming process [15]. In their work, they performed point-force deflection measurements of their microcantilevers using a Tencor P-10 profilometer to extract the Young's modulus using both a PMMA sacrificial material [15], and an amorphous silicon sacrificial layer [16]. Cruz *et al.* have also reported development of a hot wire anemometer fabricated using inkjet-printed nanoparticle ink with a minimum line width of 100µm [17]. Silver nanoparticle-based ink has also be used by Duoss *et al.* in the fabrication of wire bonds and 3D antennas with 10µm resolution using a micro-extrusion-based "direct write" process [18].

The use of alkanethiol-encapsulated gold inks for microfabrication has also been reported. Demko *et al.* have used gold nanoparticle ink to form high resolution, high aspect ratio microstructures via micromolding techniques [19]. Also, inkjet printing of hexanethiol-encapsulated gold nanoparticles to form high aspect structures has been demonstrated by Ko *et al.* [20]. In this work, out-of-plane pillars and bridges were formed by repeatedly printing in one location to slowly accumulate a material, much like stalagmite formation in geology.

As this survey shows, there is a great deal of opportunity in the advancement of inkjet printed metal MEMS. Current work is at the fundamental level, producing basic structures in order to gain the necessary processing expertise to produce more complex geometries. Work by Lam *et al.* is focusing on developing silver nanoparticles for microfabrication, making it complimentary to the work proposed herein. In the next section, a survey of thiol-encapsulated gold nanoparticles is presented to examine what has been done with this material previously.

2.2 – Thiol-Encapsulated Gold Nanoparticles

Thiol-encapsulated gold nanoparticles have proven very popular for a variety of applications, especially in the areas of medicine and biology where they have been used as fluorescent biological markers for applications such as protein detection [21]. This is due to the fact that Au-NPs do not oxidize, can be synthesized with a controlled size, as explored by Maye *et al.* [22], and are encapsulated with a thiol group monolayer. This organic thiol group can then be functionalized in order to perform specific functions, and enables the gold to be made into colloidal suspensions [23]. Two interesting biological applications of gold nanoparticles include contrast enhancement for magnetic resonance imaging [24], and for destroying tumors via hyperthermia [25].

Thiol-encapsulated gold nanoparticles also enable gold to sinter well below the melting point of bulk gold [26], making it an attractive material for inkjet printing. While several techniques exist to synthesize gold nanoparticles [21], Hostetler *et al.* demonstrated the synthesis process which has proven popular for thiol-encapsulated gold nanoparticles used for printed electronics [27].

As mentioned previously, Fuller *et al.* demonstrated the use of thiol-encapsulated Au-NPs to form proof-of-concept MEMS structures [14]. More recently, the use of thiol-encapsulated gold nanoparticles has been of great interest from Vivek Subramanian's group at the University of California at Berkeley, as part of their efforts to develop ultra-low-cost electronics and RFID tags [13, 28]. Molesa *et al.* developed a custom inkjet printer system and synthesized alkyd thiol-encapsulated gold nanoparticle ink using toluene and α-terpineol solvents [29]. Toluene has a higher volatility, enabling smaller feature sizes, but also results in potential nozzle clogging issues. Work with the Au-NP ink was quickly refined as Huang *et al.* reported on the sintering conditions required to turn gold nanoparticles with a variety of thiol groups in air and dry nitrogen into conductive gold thin films for printed electronics and RFID applications [30]. This work focuses only on very thin films suitable for conductive electronics. Soltman *et al.* studied the inkjet printing deposition parameters in order to realize smooth lines for printed electronics using the Au-NP ink [31]. Redinger *et al.* then used the gold nanoparticle ink to realize printed RFID tags using polyimide dielectric [32]. In their efforts they have found that printed gold is not as conductive as bulk gold, and have explored printing copper and silver nanoparticles as an alternative to gold to lower sheet resistance [33]. In an effort to lower the sheet resistance, Chung *et al.* explored the resistivity of gold metal films using a laser sintering process [34].

Gold pillars and bridges have been demonstrated using hexanethiol-encapsulated Au-NP ink [20]. The use of microfluidic molding techniques by Demko *et al.* [19] allows for high fidelity fabrication, but concern has been expressed that there are sintering issues with the high aspect ratios structures, as a gold film forms on the outside of the structure

first, preventing the sublimation of all organic material at the core [35].

While the conductivity of gold films printed from hexanethiol-encapsulated gold nanoparticle films has been reported previously [14, 19, 30, 34], this research has primarily focused on thin films for printed electronics applications. No instances of the mechanical properties of inkjet-printed gold films were found in the literature. As the mechanical properties of a material are of great importance for MEMS fabrication, this presents an important area of study in order to advance the field of inkjet printed MEMS using alkanethiol-encapsulated gold nanoparticle ink.

3. Jet Printed Gold Nanoparticle Ink

This chapter details the necessary materials, tools, and processes to realize gold nanoparticle films patterned via inkjet printing. First, a background on hexanethiol-encapsulated gold ink is presented and ink synthesis described. Next, the custom inkjet deposition system built for this work is detailed. Finally, process development to determine suitable jetting and motion parameters is presented which yield patterned jet-printed gold nanoparticle lines usable for microsystems development. Chapter 5 will extend this work to explore the post-deposition techniques required to yield gold films suitable for printed microsystems.

3.1 – Gold Nanoparticle Ink Formulation

The key technology which enables low-temperature printed metal micromachining is the presence of metal-bearing liquid precursors (i.e. metal inks) suitable for jet deposition. Metal ink development is an active area of research seeking to produce low-cost conductors for applications such as organic electronics [1]. Unlike conventional metal deposition techniques, which deposit the desired material directly onto the surface, many metal inks are based on metal nanoparticles encapsulated with an organic modifier. The organic modifier is necessary to enable nanoparticle solubility in a carrier solvent for deposition. For printed electronics, material cost and film resistivity are critical parameters, so both copper (Cu) and silver (Ag) inks have been studied due to their favorable electronic properties [2,3,4]. The most popular metal ink found in the literature is silver nanoparticle based, as it is commercially available from manufacturers including the Cabot Corporation [5]. For MEMS, one drawback of copper and silver is

that these materials readily oxidize, affecting device performance [6]. Further, the use of a metal ink which forms a stable oxide may require more post-deposition processing steps to yield a highly-conductive metal film [7].

Gold (Au) is an attractive metal for MEMS fabrication as it does not oxidize under ambient conditions [8]. Therefore, developing a gold ink for printed MEMS deposition is of great interest. Alkanethiol-encapsulated gold nanoparticles are an attractive material for use as gold inks currently under development for printed electronics [9, 10, 11]. Alkanethiol ligands form an organic self-assembled monolayer (SAM) around a gold core in order to enable formation of a stable colloidal suspension in a carrier solvent. Further, changing the synthesis concentration and molecular length of the alkanethiol SAM has been shown to change nanoparticle size and metal sintering temperature [12]. These parameters are important for tuning the ink to enable proper inkjet dispensing.

Due to the large surface area to volume ratio, gold nanoparticles sinter at temperatures well below that the melting point of bulk gold [13], and have been shown to sinter below 200ºC for hexanethiol-encapsulated nanoparticles [12]. This low sintering temperature, coupled with the lack of a metal oxide to complicate processing, makes alkanethiol-encapsulated gold nanoparticles attractive for printing gold microstructures.

However, to realize the continuous gold film, post-deposition steps are required to drive off solvents, decompose encapsulating organics, and sinter the gold nanoparticles together. For alkanethiol-encapsulated gold nanoparticles, this post-processing can be accomplished simply by heating the deposited ink in air as shown in Figure 2 and described below.

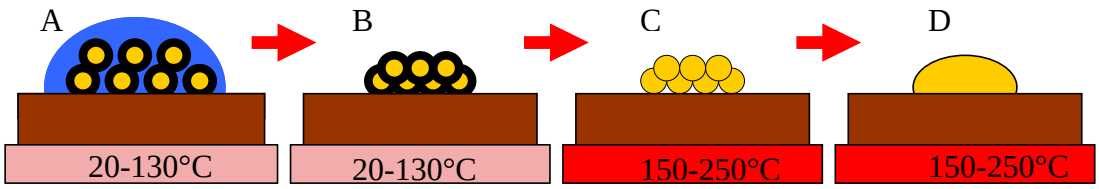

Figure 2 – Gold Ink Curing Process: solvent (blue), alkanethiol-encapsulate (black).

First, (Step A) the alkanethiol-encapsulated gold nanoparticles are suspended in a carrier solvent and inkjet deposited onto a substrate. If possible, the substrate is heated below the sintering temperature of the nanoparticles to aid in solvent evaporation. Next, (Step B) the carrier solvent is allowed to evaporate, leaving only the encapsulated gold nanoparticles. The temperature is increased (Step C), causing the alkanethiol-encapsulated SAM to sublimate. Finally (Step D), once the SAM has sublimated, the gold nanoparticles sinter together into a continuous gold film. In the literature, this sintering process is typically measured visually or by a large decrease in film resistance [14]. Once this change occurs, sintering is then stopped. Visually, the printed film transforms from black in color to gold in color as the organic SAMs sublimate. This visual change has been shown to correspond to a rapid decrease in film resistance as the gold nanoparticles come into contact and sinter into a more coherent microstructure [15]. Observing this process, it becomes apparent that sintering conditions will have an influence on the properties of the resulting gold film. The influence these sintering conditions play on the resulting gold films is presented in Chapter 5.

3.2 – Gold Nanoparticle Ink Synthesis

A previously selected gold ink formulation was selected to minimize chemistry process development. Gold nanoparticles encapsulated with hexanethiol ligands have

been used in the literature for inkjet printed electronics and exhibit favorable jetting performance and sintering temperatures of 200ºC or better [1, 10, 14, 15, 16]. These nanoparticles are then suspended in a heavy alcohol, α-terpineol, to form a precursor ink. α-terpineol is desirable as a solvent due to its low volatility which helps prevent inkjet nozzle clogging during deposition. Published gold ink recipes suspend hexanethiol gold nanoparticles to a concentration of 10-15% by weight ratio in α-terpineol to form a jettable ink [14, 15, 16].

Hexanethiol-encapsulated gold nanoparticles have been successfully synthesized using the two-phase Brust synthesis [17] as described by Huang *et al.*, with one minor addition [12]. After drying the nanoparticles in a rotary evaporator and suspending them in ethanol, the solution was placed in a freezer overnight to allow the nanoparticles to agglomerate in order to increase yield during the final drying step. Without this step, it was not possible to extract the gold nanoparticles from solution using the prescribed vacuum filtering method. A complete nanoparticle synthesis description is found in Appendix B. All precursors chemicals used were laboratory grade or better. Aside from the gold source, hydrogen tetrachloroaurate(III) hydrate (99.9% pure, Strem Chemicals, Newburyport, MA), precursors were sourced from Acros Organics and consisted of 1-hexanethiol (97%), tetraoctylammonium bromide (98%), and sodium borohydride (98%). All solvents used during this research were sourced from Fisher Scientific. Once dried using vacuum filtration, the gold nanoparticles were immediately suspended in α-terpineol (97%+ Acros Organics) by weight in an air-tight container to form the precursor ink. The container was agitated vigorously for 5 minutes to ensure that all nanoparticles were suspended in solvent before each use. Initial studies with a 60μm diameter nozzle

was used with 10% by weight nanoparticle inks, but this was increased to 15% by weight to improve printing performance with the 30µm nozzle, to improve resolution, used for the majority of this research. Work using 10% by weight nanoparticle ink is summarized in the literature [18].. An image of the hexanethiol-encapsulated gold nanoparticle ink used in this work is shown in Figure 3.

Figure 3 - Synthesized gold nanoparticle ink used in this work.

3.3 - A Prototype Research Inkjet Deposition System

Once a promising metal ink had been identified for the development of inkjet printed microelectromechanical systems, a complementary deposition system was needed for process development. Commercially available consumer-grade inkjet printers are not well suited for this work for many reasons. The inkjet heads have high variability and are constructed with low-cost materials suitable for the water-based inks used for document printing. These materials do not stand up to the harsh solvents used for metal nanoparticle ink development. Further, the motion systems are designed for low cost and typically raster scan the inkjet head across the substrate as the substrate is fed by rollers. This

results in reduced motion repeatability and higher droplet placement errors. Additionally, the consumer inkjet printer industry has developed a business model where the printer is sold at a subsidized cost and profit is made from the sale of ink. As a result, at least one manufacturer (Epson), has built-in protections against the use of "counterfeit" ink, such as those used for this work. These limitations make the use of a consumer-grade inkjet printer infeasible, so a custom inkjet deposition system was developed for this work.

To simplify the design, an X-Y motion stage was selected with a laterally fixed deposition head. This enables stationary optics to be used and simplifies wire/tubing routing during development. The deposition system used in this work was built with the following attributes which are further detailed in the following sections.

- Three axis motion system with sufficient travel to handle an 100mm wafer with a resolution of 5µm
- Ability to heat the substrate platen and ink reservoir
- Camera for observing ink droplets.
- Resilient low-dead volume ink reservoir to minimize ink waste.
- Full control over all print head and motion parameters for maximum flexibility.
- Compact footprint for enclosure in a glove-box or other environmental chamber

The custom inkjet deposition system has been constructed for this work and is shown in Figure 4. The system can be decomposed into two major components: the motion system, and the deposition system. The next sections will now detail these components of the inkjet deposition system used throughout this research for the development of jet-printed gold microelectromechanical systems.

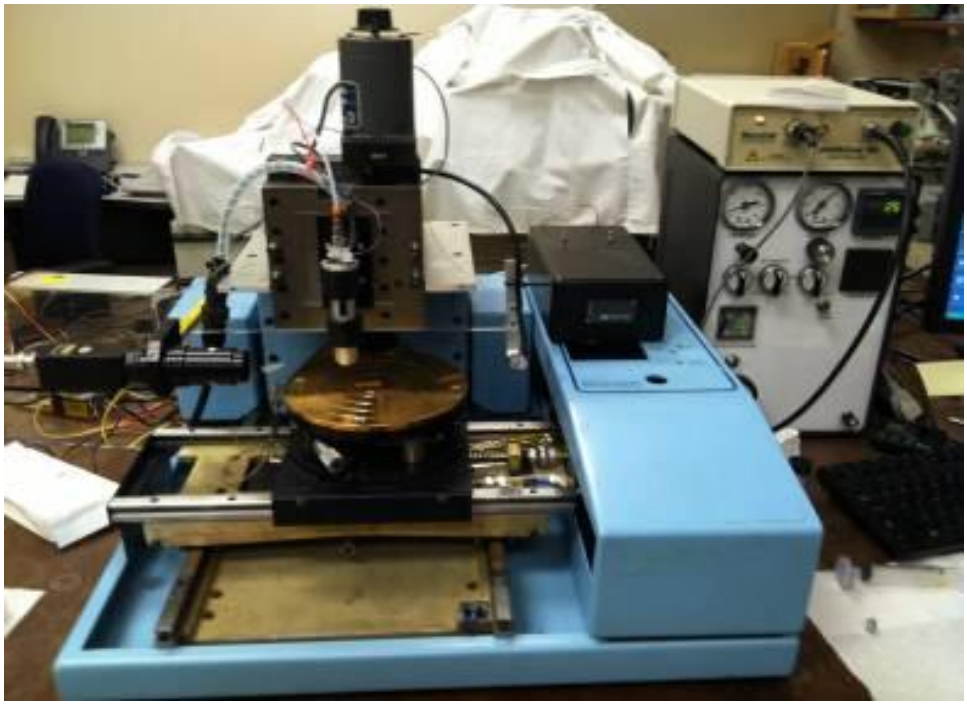

Figure 4 - Custom inkjet deposition system to be used in this research.

3.3.1 - Motion System Overview

The motion system is constructed from a heavily-modified Wentworth AWP1050 automatic wafer probe station due to its attributes and ready availability. This system provides a 6-inch diameter vacuum chuck on an X-Y motion stage with six inches of travel on each axis. The use of a motion control system designed for microelectronics ensures that all mechanical tolerances are suitable for micromachining purposes. Further, the rigid microscope mount of the system provides an ideal location to affix the print head to the system. The compact footprint of the AWP1050 is desirable for this application as the system can be placed in a fume hood to provide ventilation when using potentially harmful solvents and inks.

Motion Control Configuration

While the Wentworth AWP1050 provides an excellent base as a research-grade motion system for inkjet deposition, three key modifications were performed to further enhance its capabilities for this work. First, the stock stepper motor drivers have been removed and replaced with modern microstepping motor drivers (Part: IM483-PB1, Intelligent Motion Systems, Inc) in order to increase the motion resolution of the system to ±5µm. Second, a high-resolution Z-axis was added to the microscope mount to provide automated print head placement during operation. The Z-axis allows for precise control of the print head-to-substrate distance during printing and also allows the system to rapidly move the print head away from the hot platen after operation. An Aerotech, Inc linear stage (Model: ATS-302M) was selected for this task and mounted vertically using a commercial adapter (Aerotech HDT3M) to provide a Z-axis resolution of 1µm or better. Finally, the control system of the AWP1050 was removed and the stepper drivers were connected directly to a Linux control PC via the parallel port to enable complex motion control.

Heated Platen

One critical capability of a research-grade inkjet deposition system is to provide temperature regulation of the vacuum platen for samples. The ability to heat substrates and hold them at an elevated temperature is important in order to control print resolution by evaporating carrier solvents at an increased rate. Unfortunately, the stock vacuum platen provided on the AWP1050 is an unheated anodized aluminum plate, so modification was required.

The stock platen was removed and a T-type thermocouple (Omega Engineering Inc.)

was embedded into the aluminum platen to provide temperature feedback. A four inch diameter polyimide heater (Part: KHR-4/5-P, Omega Engineering Inc.) was then affixed to the bottom of the platen using the included pressure sensitive adhesive. A PID temperature controller (Part: PXR3, Fuji Electric) was then connected between the heater and the thermocouple to provide closed-loop control. The temperature controller was tuned and provides substrate heating up to 150ºC with a variation of ±3ºC. The maximum platen temperature is limited by the pressure sensitive adhesive supplied with the heating element for mounting.

Motion Control Software

The final piece of the motion control system is the software to translate digital geometry files into coordinated motion. A commercially available solution was sought to minimize development time. A free software package, the Enhanced Machine Controller (EMC2), was identified and utilized in this work. EMC2 is an open-source machine control program originally developed by the National Institute of Standards and Technology (NIST) for driving computer numerically controlled (CNC) machining equipment such as milling machines, drill presses, and lathes [19]. The EMC2 software package reads in a digital path file written using G-Code commands, an industry standard, and translates the commands into corresponding motion paths. EMC2 was selected for this purpose as existing CNC software tool paths exist which can take a 3-D CAD model and generate an appropriate G-Code file for manufacturing. The use of EMC2 allows for rapid modifications to the motion system to accommodate the inkjet print heads, and provide simple motion path generation. A screenshot of EMC2 graphical user interface is shown in Figure 5. The interface gives the user manual control over all aspects of the

system and provides a real-time graphical representation of the file as it is executed, both highly desirable features for development applications.

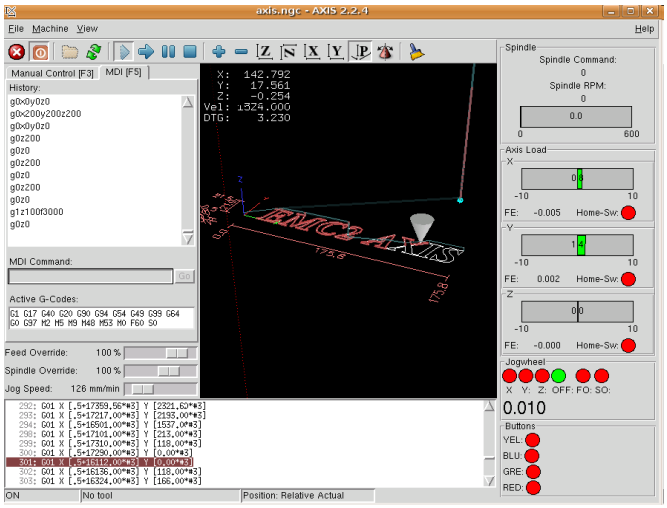

Figure 5 - Screenshot of the EMC2 User Interface

3.3.2 –Custom Jet Deposition System

The drop-on-demand inkjet print nozzles selected for this work are a commercially available piezoelectric system from MicroFab Technologies, Inc. in Plano, TX. The print nozzle is constructed from a borosilicate glass capillary tube, which is drawn to a point and back-polished to the desired nozzle diameter. Initial studies used a 60µm diameter nozzle (Model: MJ-AL-01-060), while a majority of work was performed using a 30µm diameter nozzle (Model: MJ-AL-01-030) to achieve smaller minimum features. An annular lead zirconate titanate (PZT) piezoelectric crystal is adhered to the glass capillary and then the nozzle is mounted into a stainless steel housing which interfaces to an ink reservoir via a Luer Lock fitting. A mesh filter (5.0µm pore size) is installed between the nozzle and Luer Lock fitting to minimize nozzle clogging. The use of a Luer Lock fitting enables a small medical-grade syringe to be used as an ink reservoir, creating small dead

volumes and enabling the use of harsh solvents for deposition. The print nozzle and ink reservoir then mount in a heated aluminum enclosure forming the print head. Air pressure and vacuum are plumbed to the ink reservoir to facilitate unclogging of the print nozzle and to control the ink meniscus shape. The print head was mounted onto the Z-Axis of the motion system along with a video camera to enable real-time print nozzle monitoring during all phases of operation as shown in Figure 6. The print nozzle is driven by a piezoelectric waveform generator and amplifier (Jetdrive™ III, MicroFab Technologies) which is controlled via computer over an RS-232 serial connection.

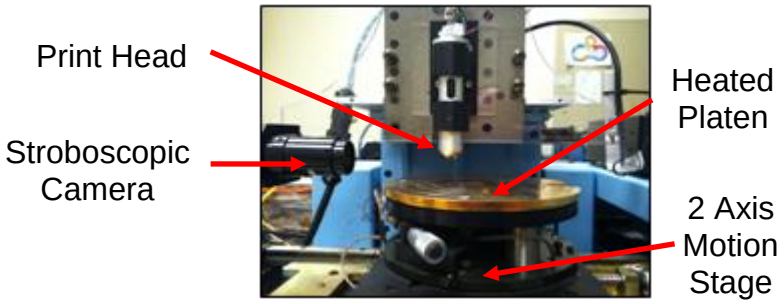

Figure 6 - Placement details of important deposition subcomponents.

Stroboscopic Camera System

A digital video camera (Sentech STC-400HOL) and LED light source are mounted orthogonal to the print nozzle with a 200mm focal distance, enabling real-time monitoring the print nozzle during deposition as demonstrated in Figure 7. High-speed imaging is achieved by pulsing, or strobing, the LED backlight with a controlled delayed from the droplet triggering pulse. The delayed illumination captures the droplet state at that time after initiation of droplet formation. The camera is of critical importance for development as ink jetting size, velocity, and stability can be monitored in an effort to optimize the print nozzle drive waveforms. Further, the camera enables the detection of

ink clogs in real-time and facilitates nozzle cleaning. The camera system is directly interfaced with the print nozzle control software.

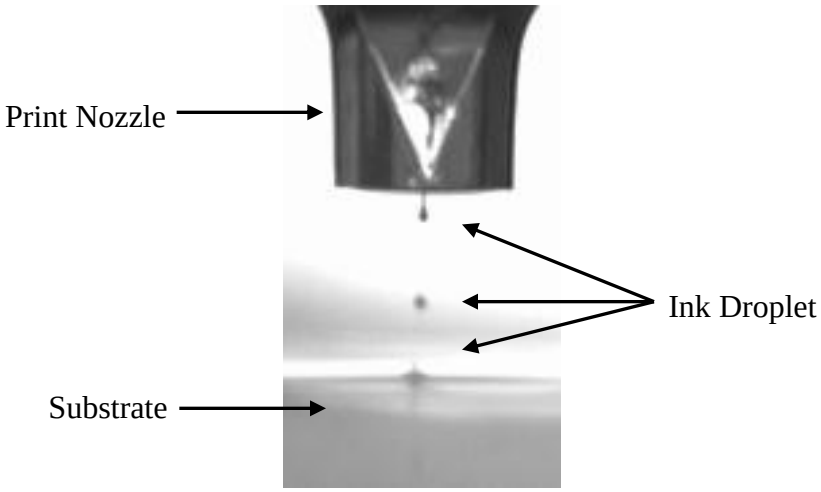

Figure 7 – Stroboscopic camera image showing droplet formation and flight.

Print Nozzle Control Software

MicroFab Technologies produces their JetServer™ software to complement their drop-on-demand print heads and waveform generator. JetServer™ provides full control over the drive waveform shape and repetition rate through a single convenient graphical user interface as illustrated in Figure 8. The software supports three types of drive waveforms: bipolar, sinusoidal, and arbitrary.

The software interfaces with the stroboscopic camera to provide two important functionalities. The first is the ability to sweep the strobe LED delay for the camera strobe in order to visualize droplet development and trajectory on the camera. This is important for identifying suitable drive parameters for fluid jetting. Additionally, the JetServer™ software interfaces with the third party Aphelion™ image processing software package to quantify droplet size, trajectory, and velocity from stroboscopic camera images. These parameters are critical to assess the resolution and stability of the

jetted droplet, respectively.

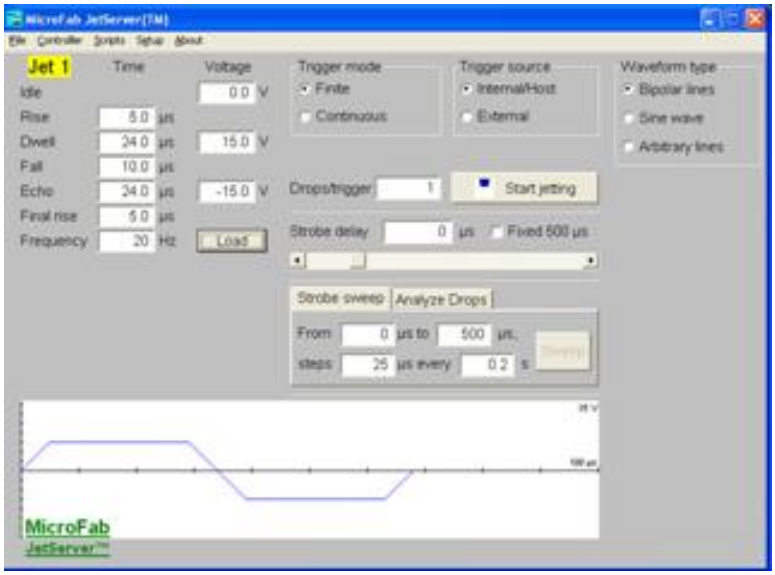

Figure 8 - MicroFab JetServer™ Graphical User Interface

The JetServer™ software package also allows the user to either use an internal or external electrical triggering pulse, where a user selectable number of droplets can be ejected for each trigger event. The external trigger accepts a 5V TTL signal from EMC2 the enable coordinated motion and deposition operations.

3.4- Stable Jetting of Hexanethiol Gold Nanoparticle Ink

Process development was performed to establish stable droplet generation of hexanethiol-encapsulated gold nanoparticles suspended in α-terpineol. These jetting parameters have been studied extensively and depend upon the geometry of the nozzle and ink properties including viscosity, surface tension, and acoustic velocity [20, 21, 22].

A bipolar drive waveform is commonly employed for droplet generation and was selected for jetting development [23]. This type of drive waveform consists of a positive voltage pulse to eject a droplet, followed by a negative voltage pulse to cancel out

residual pressure waves in the inkjet nozzle to prevent the formation of secondary "satellite" droplets [24, 25]. The formation of satellite droplets results in ink deposition at undesired locations, a phenomenon detrimental for the implementation of printed microsystems.

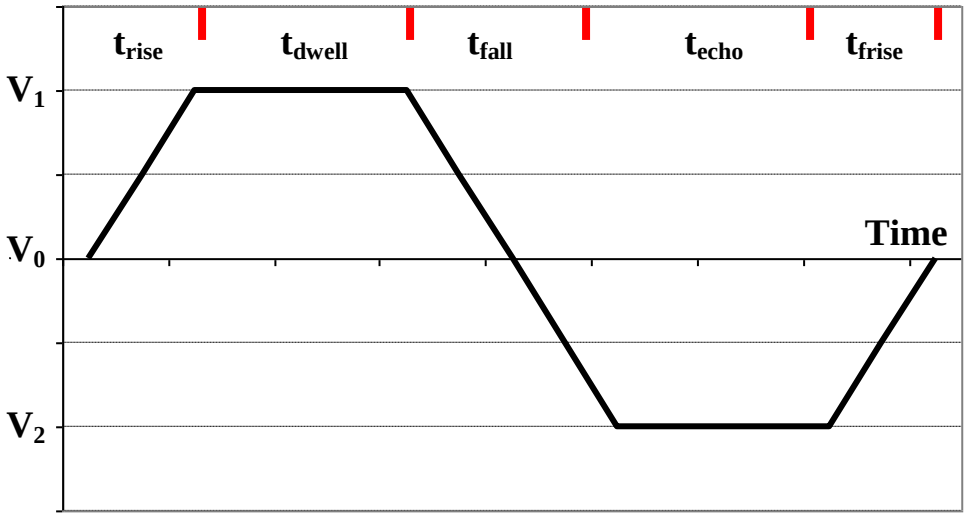

Figure 9 - Prototypical bipolar drive waveform for a piezoelectric print nozzle

A prototype bipolar voltage waveform used to drive a Microfab piezoelectric print nozzle is shown in Figure 9. During t_{rise}, a positive voltage is applied to the PZT crystal causing it to expand, which generates a pressure wave in the ink inside the nozzle cavity. This voltage is maintained for time t_{dwell} to allow the pressure wave to propagate through the nozzle. The voltage is then decreased over time t_{fall}, which contracts the print nozzle, ejecting a droplet of ink. In this bipolar configuration, the voltage swings negative during t_{fall}, and the nozzle is held in a contracted state for time t_{echo}, before returning to the starting position during time t_{frise}. As mentioned previously, this echo pulse is used to cancel out pressure waves in the inkjet nozzle to counteract satellite formation. Table 1

details the waveform parameters used in this work which were found to generate a stable stream of consistent ink droplets. Waveform generation was performed at a 1 kHz rate to allow easy drop visualization and this droplet generation rate was reduced to 20 Hz during operation.

Table 1 - Au-NP Ink Jetting Parameters

Parameter	60µm nozzle, 10%wt Au-NP ink	30µm nozzle 15%wt Au-NP ink
V_0	0 V	0 V
t_{rise}	5 µs	2 µs
t_{dwell}	24 µs	5 µs
V_1	15 V	30 V
t_{fall}	24 µs	2 µs
t_{echo}	24 µs	5 µs
V_2	-15 V	-30 V
t_{frise}	5 µs	2µs
T_{max}	40°C	35°C
rate	1kHz, 20Hz	1kHz, 20Hz

One important parameter to characterize for these deposition parameters is the maximum temperature the ink can reach before stable droplet jetting ceases. As the deposition system utilizes a heated substrate platen capable of 140°C, the print head will experience convective heating during operation. The inkjet nozzle is maintained at a 1mm gap during deposition, and the aluminum nozzle housing contains an integrated thermocouple. Passive heating of the print head was monitored during operation and the maximum operating temperature (T_{max}) of each jetting recipe is listed on Table 1.

3.5 – Substrate Selection

Once stable jetting parameters were established, identifying an appropriate substrate for development is required. When selecting a substrate for inkjet printed

applications, several material properties should be considered to ensure success. As material is patterned via a liquid ink, the wettability of the underlying substrate plays an important role in how ink behaves during deposition. One measure of the wettability of a material is by quantifying the contact angle a liquid droplet forms at the solid/liquid/gas interface [26]. Additionally, as several thermal processing steps are required to evaporate solvents and sinter nanoparticles together, the coefficient of thermal expansion (CTE) is of critical importance. If the CTE of the substrate is sufficiently large, temperature changes may cause discontinuities in printed films, or stresses and deformations may form in devices after cooling. Also, the maximum stable temperature of a material is important to ensure the substrate material can handle the temperatures necessary for thermal process steps.

For this study, two rigid and two flexible substrates were selected for investigation and a few of their properties are listed in Table 2. The goal of this experiment was to examine the visual differences of inkjet-deposited gold nanoparticles in order to select a substrate for further development. Soda lime glass (Corning 0215) was selected due to its excellent wetting properties, low-cost, and ready availability as the primary development substrate in this research. Alumina (625µm thick, non-porous, McMaster-Carr), owing to its excellent thermal, chemical, and mechanical properties, is of interest as a substrate for metrology studies of sintered gold films. Polyimide film (125µm thick, McMaster-Carr) is a high-temperature polymer which has proven popular as a low-cost substrate for flexible electronics [10]. Finally, parylene-C (25µm thick) was investigated selected as it is a popular polymer in microelectronics applications which is able to be conformally coated onto arbitrary substrates at low-temperatures [27].

All as-received substrates were first cleaned in ethanol and dried using clean dry air. Flexible substrates were attached to a clean Corning 0215 glass slide using polyimide tape to minimize film stresses and ease handling.

Table 2 - Investigated Substrate Material Properties

Material	CTE (ppm/°C)	Max Temp (°C)	Contact Angle H_20 @ 20°C	References
Parylene-C	35	290 (melts)	99±5°	[27], [28]
Corning 0215	8.9	724 (softens)	39±4°	[29], [30]
Polyimide	20	520 (decomposes)	82°	[31], [32]
Alumina	8.2	1700 (max usable)	-	[33]

All samples were positioned onto the platen, and then heated to 130ºC and allowed to stabilize for 10 minutes. After heating, one sample was aligned under the printhead and a print nozzle to substrate spacing 1 millimeter established. The 60µm diameter nozzle was installed in the system and filled with a 10% (by weight) hexanethiol-encapsulated gold ink in α-terpineol. A 20Hz bipolar waveform using timing parameters of 5/24/10/24/5µs at ± 15V was then used to print a test pattern. This process was repeated for the remaining substrates, with all other parameters being held constant. The patterned substrates were then imaged using optical microscopy (Karl Suss PM-5). The resulting patterns are shown in Figure 10.

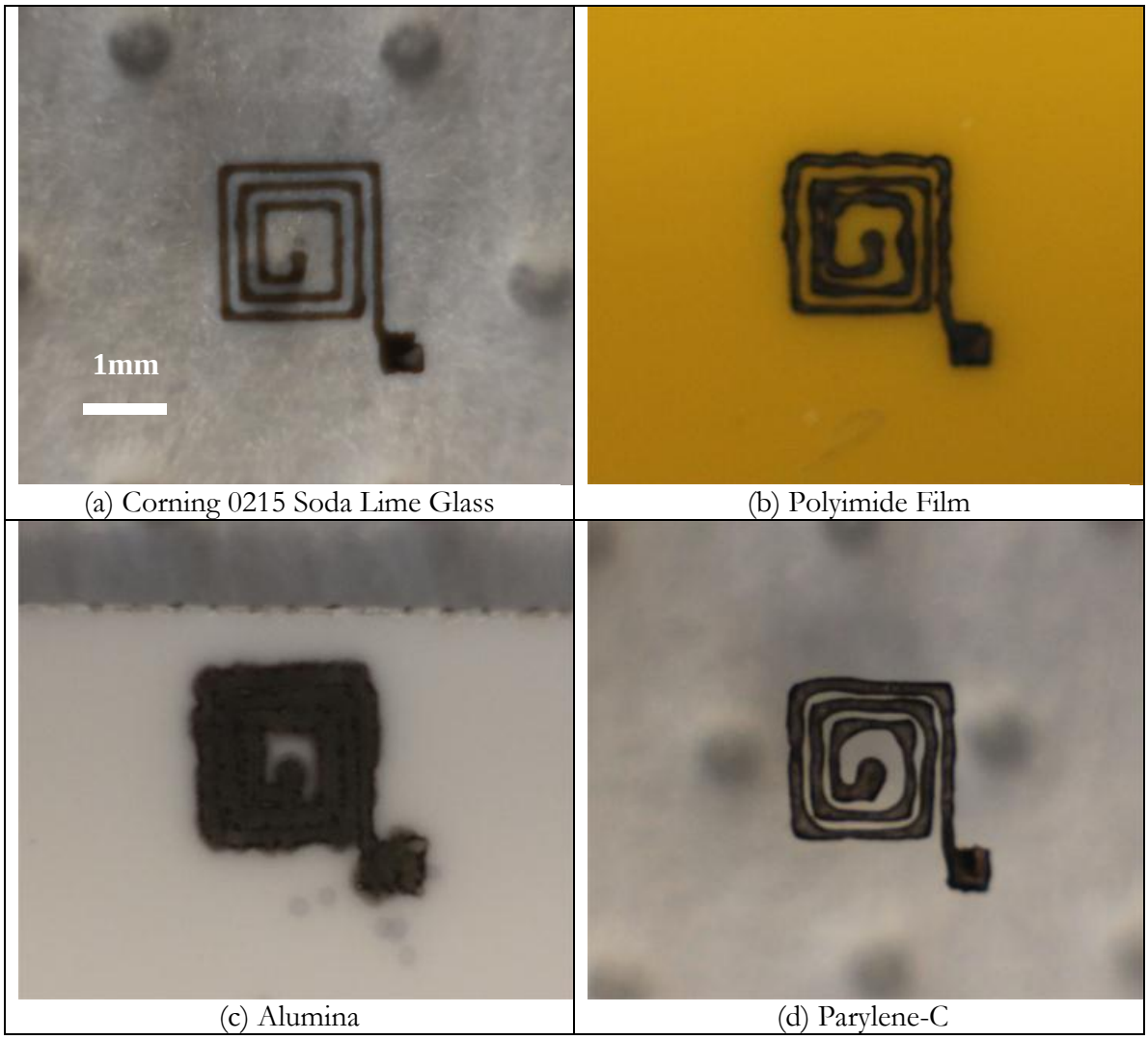

Figure 10 - Patterned Au-NP (10% wt) ink on various substrates.

Examining the test specimens, it is immediately apparent that substrate properties have a major impact on the resulting inkjet printed gold line quality under identical deposition conditions. The soda lime glass substrate produced smooth structures with a line width of 90µm. The alumina substrate produced the poorest quality features, with the printed lines spreading significantly. Both polymeric substrates produced wavy lines requiring further optimization to yield usable micro-scale printed features. This investigation demonstrates a strong dependence on substrate surface properties and

means that deposition parameters may require tuning for each substrate material. As the objective of this research is to study sintered gold films deposited via inkjet printing, one candidate substrate was selected for further development. Due the results of this study, ease of handling, and the small CTE of Corning 0215 soda lime glass, it was selected as the primary substrate for further development towards jet printed gold microelectromechanical systems.

3.6 – Droplet Resolution versus Platen Temperature

Selecting an operating temperature for the substrate during deposition is another key a parameter which influences printed line quality and resolution. Upon droplet impact, it is desirable to rapidly evaporate the carrier solvent to prevent spreading and minimize the "coffee ring" effect [34]. α-terpineol with low-volatility and a boiling temperature of 219°C requires an elevated substrate temperature to maximize printed resolution. An elevated platen temperature also increases the heating rate of the inkjet head during operation, so an appropriate platen temperature must be determined.

For this study two different substrate materials were examined to quantify printer droplet resolution versus substrate temperature. The first substrate is clean dry Corning 0215 soda lime glass slide, the standard substrate for this work. The second substrate is a clean Corning 0215 slide coated with a 25μm layer of an aerosol deposited high-temperature dielectric enamel (Rust-Oleum #248941) which is detailed further in the next chapter. The dielectric enamel was spray deposited onto a soda lime glass substrate, air dried for 10 minutes, and then hot plate cured at 250°C cure for 1 hour.

The 30μm nozzle was installed onto the print head loaded with a 15% (by weight) Au-NP in α-terpineol ink formulation. The print head was programmed to produce a

bipolar waveform using timing parameters of 2/5/2/5/2µs at ±30V for deposition. The ink temperature was monitored during deposition maintained at 30°C during all deposition procedures. Starting from room temperature (RT, ~20°C), a 3 by 3 grid of single ink droplets was deposited onto each substrate. The platen temperature was then increased and allowed to stabilize for 10 minutes before deposition is repeated. This process was performed up to the maximum platen temperature of 140°C. The droplet diameters were then measured using optical microscopy (±3µm uncertainly) and are shown in Figure 11.

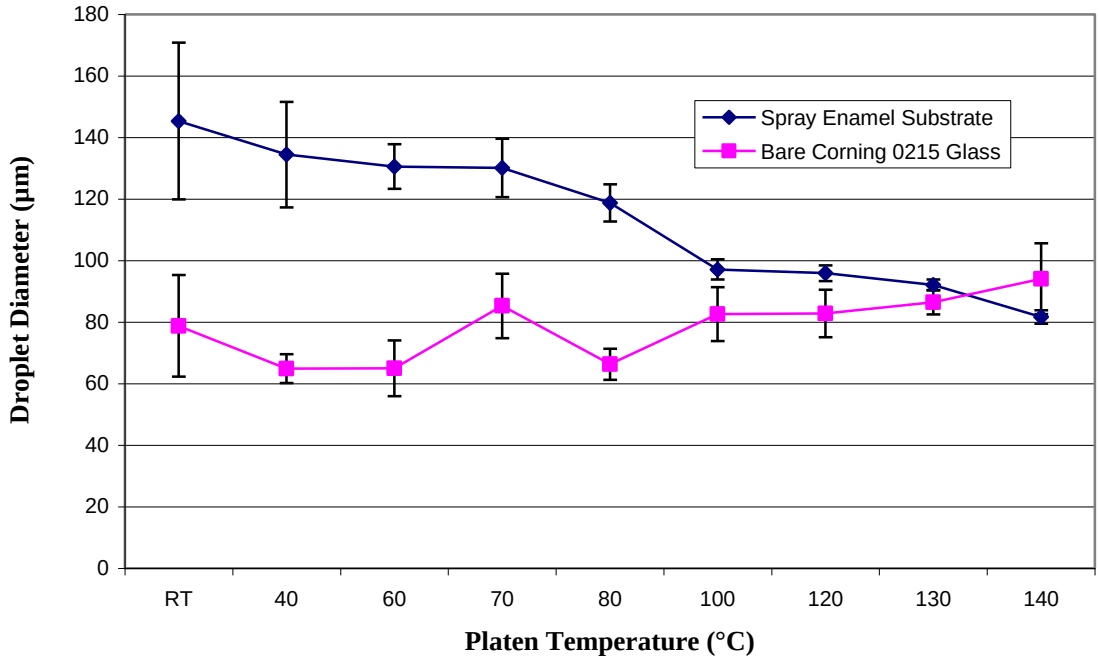

Figure 11 - Jetted Droplet Diameter versus Platen Temperature

For the bare Corning 0215 substrate, the average droplet diameter did not show a significant change with increasing platen temperatures in the conditions studied. The droplet shapes on Corning 0215 were highly irregular, as shown in the diameter variability, suggesting that significant spreading occurs upon droplet impact. This is

likely due to the hydrophilic nature of glass. In contrast the high-temperature spray enamel substrate demonstrated increasing droplet resolution with increasing platen temperature. Starting at 100°C, the shape of the droplets became quite round in nature, creating high quality droplets suitable for microfabrication. At 140°C, deposited Au-NPs on enamel exhibited smallest droplet sizes with controlled shape and high uniformity, making this temperature the best choice for high resolution features. If a slightly large line width is suitable, the platen temperature can be reduced to as low as 100°C while forming uniformly shaped nanoparticle features on the substrate.

3.7 – Summary

This chapter presented hexanethiol-encapsulated gold nanoparticles and their subsequent suspension (10-15%wt) in α-terpineol to form a jet printable gold ink. A custom inkjet deposition has been presented with sufficient resolution and control for the development of printed microsystems. Using a commercially purchased piezoelectric inkjet nozzle, stable jetting parameters were found for the Au-NP inks studied in this work. Test structures were next patterned onto soda lime glass (Corning 0215), alumina, polyimide, and parylene-C substrates, which demonstrate an influence of substrate properties on the resulting patterned Au-NP films. Corning 0215 glass was then selected as a primary substrate for this research due to favorable patterning results, low-cost, and ease of use. To quantify the dependence of substrate platen temperature of droplet resolution, Au-NP droplets were patterned onto test substrates for temperatures ranging from 20°C to 140°C. Measurements were performed on a Corning 0215 soda lime glass substrate, as well as a spray deposited dielectric enamel, detailed in the next chapter. For Corning 0215, the droplet resolution did not trend strongly with temperature and droplet

shapes remained irregular in all measurements. A printed clamped-clamped bridge structure on glass is shown in Figure 12. In contrast, the high-temperature enamel showed increasing resolution with temperature and droplets become uniform and repeatable about 100°C, with a maximum droplet resolution at 140°C. Figure 13 demonstrates the line quality of Au-NPs (15%wt) printed at 140°C on the dielectric enamel using standard print parameters.

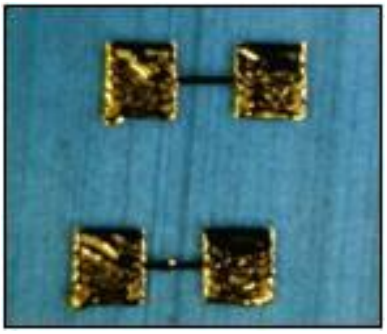

Figure 12 – Partially sintered (10%wt) 500μm long clamp-clamped bridge structures on Corning 0215 soda lime glass.

Figure 13 – As-deposited Au-NP ink (15% wt) patterned onto high-temperature enamel at 140°C platen temperature which demonstrates smooth repeatable line widths.

4. Aerosol-Deposited Dielectric Enamel

This chapter explores the use of aerosol deposited enamel as a surface coating and dielectric material for inkjet printed microsystems. Identifying a suitable dielectric structural material to complement the conducting structural material is critical for the realization of multilevel geometries found in microelectronics and MEMS devices. For conventional silicon-based MEMS structures, silicon dioxide and silicon nitride typically serve this role, allowing for the fabrication of complex three-dimensional structures [1, 2].

To identify a promising candidate structural dielectric material for inkjet printed microsystems, several material properties should be considered with respect to its thermal, chemical and electrical properties. Foremost, the material must be an excellent insulating material with usable dielectric characteristics for the development of printed electronic systems. The material must be thermally compatible with the process temperatures and durations required for device manufacturing. As hexanethiol-encapsulated gold nanoparticles sinter in the 150-230°C range, the dielectric material must be stable to these temperatures. The material must also be stable when exposed to the potentially volatile carrier solvents present during inkjet deposition to which the dielectric material will be exposed during the deposition of subsequent layers. Finally, the most attractive dielectric materials for inkjet printed applications will be dielectric materials which have the potential to themselves be selectively deposited via inkjet printing.

Additionally, as was shown in Chapter 3, the properties of the underlying substrate have noticeable effects on the resulting inkjet printed gold nanoparticle features for a given deposition recipe. This proves problematic, as process development and optimization may be required to realize equivalent inkjet printed microsystems on each different substrate. One potential solution to this issue is the introduction of a dielectric surface coating to provide consistent surface properties for inkjet deposition and to isolate the bulk substrate from the device itself. This is common practice in conventional microelectromechanical systems, where silicon nitride is often used to electrically isolate the devices from the bulk silicon substrate [3]. Towards this aim, a dielectric material with attributes sufficient for inkjet printing, but additionally able to perform as a conformal surface coating of the the bulk substrate is desirable for inkjet printed MEMS applications.

Spin coating is commonly employed for the uniform coating of polymeric materials for microsystems applications [4]. Unfortunately, the nature of this technique limits its applicability to substrates which are discrete in nature, rigid, and relatively flat. As inkjet printed microsystems are of interest for large-area flexible substrates, a dielectric deposition via spin-coating may prove impractical as substrate size is increased.

Spray coating is a technique widely used in the surface finish and adhesive industries to conformally coat surfaces of arbitrary size on topology [5]. The automobile industry, for example, uses spray coating to deposit several layers of primer and paint as a surface finish for their products using robotics [6]. On a smaller scale, aerosol-based spray coatings (e.g. spray paint) are widely used for industrial and consumer applications [7]. In fact, several manufacturers market aerosol-based photoresists for microelectronics

applications such as SU-8 Microspray™ from Microchem, Inc [8]. Additionally, as the surface finish of paint is a critical parameter, many commercially available aerosol-based surface coatings have been engineered to provide consistent surface finishes on a variety of underlying substrates [9, 10, 11]. The promise of conformal deposition with consistent surface properties on arbitrary substrates makes aerosol deposited materials attractive for substrate isolation of inkjet printed microelectromechanical systems and warrant further exploration.

While there are a multitude of commercial aerosol-based surface finishes on the market from dozens of manufacturers, many formulations cannot handle the aggressive temperatures and solvents present during inkjet printing [12]. One candidate aerosol-based surface finish is a high-temperature enamel formulated for aftermarket automotive engine applications. Manufactured by the Rust-Oleum Corporation and marketed as *Engine Enamel* (Part: 248941, Chevy Orange), this glossy surface finish is reported to be stable for temperatures up to 260°C (500°F) while resisting degradation when exposed to hydrocarbons such as octane [13]. While the competitive nature of surface coating market means that the exact surface coating chemical formulation is proprietary, information can be gleaned from published information of resins with similar characteristics [14]. The enamel is formed from 13.7 – 27.4% solids by weight blend of proprietary modified alkyd resin dissolved in a ketone/aromatic solvent mixture containing toluene, xylene and acetone [15]. Generally, the curing of coatings using modified alkyd resins occurs in two stages. First, the volatile carrier solvents evaporate forming a dry film, and then the alkyd chains oxidize, cross-linking together to form a resilient finish. [14, 16]. This oxidation process may require a chemical catalyst or

elevated temperature. For the Rust-Oleum enamel identified for study, curing may be performed at elevated or ambient temperatures [13]. The remaining portion of this chapter will explore the necessary process techniques and pertinent material properties of this high-temperature enamel towards its use as an aerosol dielectric surface coating and structural material for inkjet printed microsystems.

4.1 – Deposition and Curing Conditions

To explore aerosol deposited enamel as a structural dielectric, a baseline deposition process was required to yield an enamel substrate suitable for inkjet printing. Deposition of the enamel was performed in an open-top container (450mm W by 610mm L by 305mm H) located in a fume hood to provide adequate ventilation. Highly-absorbent low-particle wipers (Texwipe BetaWipe TX2009) were used to line the bottom of the spray box to minimize substrate contamination during spray deposition. Enamel deposition followed guidelines from the manufacturer's recommendations found in the Technical Data Sheet and were performed in the following manner [13].

- First, the substrate is cleaned and dried before placement in the center of the box. For the soda lime glass (Corning 0215) used throughout this work, the as-received glass is cleaned in acetone and ethanol, then dried using compressed-dry air.
- The aerosol can is then shaken vigorously for 2 minutes to fully homogenize the enamel resins and organic solvents.
- From a distance of 300mm, the aerosol can is actuated and then swept across the substrate at a rate of approximately twelve inches per second. Using this technique, five successive passes are performed. For Corning 0215 glass, this technique yields a visually smooth and uniform surface coating.

- The enamel is allowed to air dry at room temperature for 10 minutes before being transferred onto a hot plate at 250°C to fully cure for one hour.

This technique consistently yielded enamel films suitable for inkjet printing and is used throughout this work. The thickness of the resulting films was measured several times and varied between 15 and 20μm. During experiments it was observed that exposing the enamel to temperature of 250°C in air for several hours or more caused the film color to darken. However, the change does not appear to affect the enamel's properties for gold films deposited onto them, as measured by the resulting inkjet printed line widths.

4.2 – Stability in Solvents

Once deposition and curing techniques were established the enamel was tested in a variety of solvents it may encounter during inkjet printing to verify compatibility of the material. Enamel samples were prepared by spray coating and curing a uniform layer using the technique described in the previous section onto clean Corning 0215 soda lime glass slides. The enamel coated substrates were then scored and snapped into approximately 1cm^2 samples. A collection of solvents encountered during printing were procured and are listed in Table 3, along with the resulting observations. All solvents were laboratory grade (Fisher Scientific) with the exception of the xylene (Klean-strip, consumer grade) and the α-terpineol (Aldrich Chemical, 90% technical grade). Technical grade α-terpineol was selected for this experiment as the lower purity mixture is liquid at room temperature. 20mL of each solvent was poured into a small glass beaker, the sample submerged, and was covered to prevent solvent evaporation. All tests were kept at room temperature (20°C) throughout the duration of the experiment. The samples were

monitored regularly for signs of degradation. Samples were immersed for a minimum of 24 hours before being removed and allowed to air dry. As the enamel resin was originally dissolved in toluene and xylene in the spray can, samples were further immersed for up to one week and then removed from solvent and allowed to air dry. The soaked samples were then visually inspected and compared to an untreated control samples. As shown in Table 3, apparent degradation was only observed for the enamel in toluene after extensive immersion. For inkjet printing applications, the enamel will normally only be exposed to solvent for short durations, so the results suggest that the cured enamel is suitably robust for the application at hand.

Table 3 - Enamel Immersion Observations for Various Solvents

Chemical	Duration	Observations
α-Terpineol (90%)	24 hours	No observable change.
Isopropanol	24 hours	No observable change.
Methanol	24 hours	No observable change.
Acetone	24 hours	No observable change.
Methyl Ethyl Ketone	24 hours	No observable change.
Xylene	168 hours	No observable change.
Toluene	72 hours	No observable change.
Toluene	168 hours	Toluene discolored, enamel surface dull

4.3 – Reactive Ion Etching of Spray-coated Enamel

While the stability of the cross-linked enamel immersed in solvent is highly desirable for inkjet printed microelectromechanical systems, there may be applications when it is desirable to patterned or remove the enamel from a device. Reactive Ion Etching (RIE) is a popular dry-etching technique for the removal of both inorganic and organic materials by ionizing gases using radio frequency (RF) energy that in turn react with the material to be etched [2]. To explore the use of RIE etching for the patterning

and removal of the cross-linked enamel, a baseline etch recipe needs to be identified for comparison. One cross-linked polymer commonly used in microelectromechanical systems is polydimethylsiloxane (PDMS), which is popular for fluidic applications [17]. Dry etching of this material has been explored extensively in the literature [18, 19, 20, 21]. For purposes of establishing a baseline process to which the results can be compared to that of PDMS, the etch conditions published by S.R. Oh were selected for this reactive ion etch study [21].

4.3.1 – Experimental Procedure

All etches were performed in a March CS-1701 clam-shell RIE etcher using a 600W 13.56MHz RF generator (ENI Model# ACG-6B). The RIE etch tool is plumbed with a closed-loop water chiller (Thermo-Scientific ThermoFlex9000) which cools both the top and bottom electrode of the etch chamber. For all experiments the power was maintained at 100W and the chamber pressure was maintained at 300mTorr. The temperature of the closed-loop chiller was set to 55°F to minimize heating effects on the sample during etching. Oxygen (O_2), and ultra-high-purity grade tetrafluoromethane (CF_4), both from Airgas Inc., were supplied to the RIE tool for these experiments.

Enamel coated soda lime glass samples were prepared using the standard procedure outlined in this chapter. After curing for one hour at 250°C, the samples were allowed to cool before the substrate was scored and snapped into small samples. 1 mil thick polyimide tape (DuPont Kapton™) was next placed over a portion of each sample to mask part of the enamel to provide an etch step for measurement.

During each etch run, the sample was placed on a 100mm polished bare <100> silicon wafer to isolate the sample from the chuck of the RIE reactor. The total gas flow

rate was maintained as close to 20sccm while maintaining the desired flow ratio as described by Oh [21]. Any deviations from 20sccm were due to limitations of the March CS-1701 gas flow control to maintain the desired gas ratio. Each sample was etched for 15 minutes and then removed from the RIE tool. A delay of 15 minutes between successful runs was used to allow any components of the etch tool to return to baseline conditions.

Etched samples were then placed in an ultrasonic bath in deionized water for 10 minutes (discussed below) to remove surface particles prior to measurement. After sonication, the samples were dried using compressed dry air and the polyimide masks removed. Step height measurements were performed using a KLA Tencor P-2 Stylus Profilometer with a contact force of 10 mg. Three step-height measurements were taken for each sample to provide an indication of etch uniformity.

4.3.2 - Results

Results of the reactive ion etch experiments are shown in Table 4 and images of the corresponding samples are illustrated in Figure 15. After etching, samples were observed to turn white where exposed to the etch process (Figure 14). Inspection of thee etched samples revealed the white to be a particulate residue from the etch process. A 10 minute soak in deionized water under ultrasonic agitation removes the particulate residue. After agitation, the etch rate calculated using etched step height show that the highest etch rate for a CF_4:O_2 flow ratio of 1:1. Each sample was measured four times and an average step height computed. Table 5 compares the etch rate of the enamel in this study to that of Oh's findings for PDMS for comparison [21]. While, PDMS also exhibited a maximum etch rate under a 1:1, the etch rate behavior for the enamel vary significantly

for varied gas flows is comparison. As the percentage of CF_4 is increased, the RIE enamel etch rate decreases steadily, indicating that oxygen may play an important role and should be explored further.

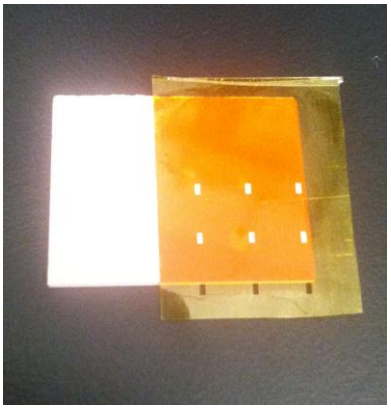

Figure 14 – 1:1 CF_4:O_2 RIE etched enamel showing polyimide mask and discoloration of where red has bleached white.

Table 4 - Enamel RIE Etch Rate for varied CF_4:O_2 flow ratios

Sample Number	Etch Rate (µm min^{-1})	Flow Ratio of CF_4:O_2	Avg Step for 15min etch (µm)	CF_4 Flow Rate (sccm)	O_2 Flow Rate (sccm)
1	0.25	All O_2	3.78 ± 0.21	0	20
2	0.52	1:1	7.85 ± 0.15	10	10
3	0.25	2:1	3.72 ± 0.25	12	6
4	0.18	3:1	2.71 ± 0.06	15	5
5	0.13	4:1	1.95 ± 0.02	16	4
6	0.09	5:1	1.28 ± 0.07	15	3
7	0.07	6:1	1.09 ± 0.13	18	3
8	0.07	7:1	1.00 ± 0.04	14	2
9	0.05	8:1	0.80 ± 0.05	16	2
10	0.00	All CF_4	Roughened	20	0

Table 5 - RIE Etch Rates of Enamel and PDMS under varied CF_4:O_2 flow ratios

Flow Ratio of CF_4:O_2	Enamel Etch Rate (μm min^{-1})	PDMS Etch Rate from [21] (μm min^{-1})
All O_2	0.25	0.1
1:1	0.52	1
2:1	0.25	0.9
3:1	0.18	0.85
4:1	0.13	0.65
5:1	0.09	0.6
6:1	0.07	0.65
7:1	0.07	0.9
8:1	0.05	0.9
All CF_4	0.00	0.4

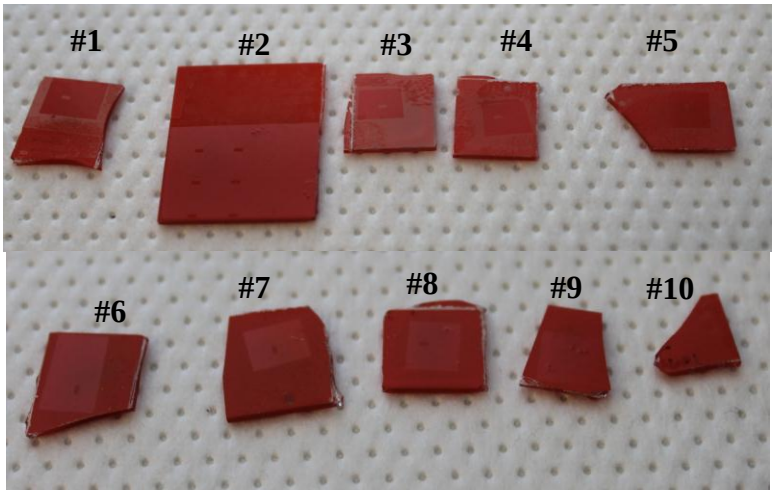

Figure 15 - Image of reactive ion etched enamel samples. Label corresponds to sample number in Table 4.

For all samples, the surface finish was roughened due to the etch process, changing its wetting properties. This phenomenon is illustrated in Figure 16, where a deionized water droplet was placed on the enamel etched for 15 minutes in pure oxygen. The etched enamel appears much more hydrophilic as the water beaded up onto this portion of the sample while retreated from the as-cured enamel. This observation

indicates that the enamel surface properties can be modified using RIE oxygen plasma, an important phenomenon for the microfabrication of other polymers including PDMS [17].

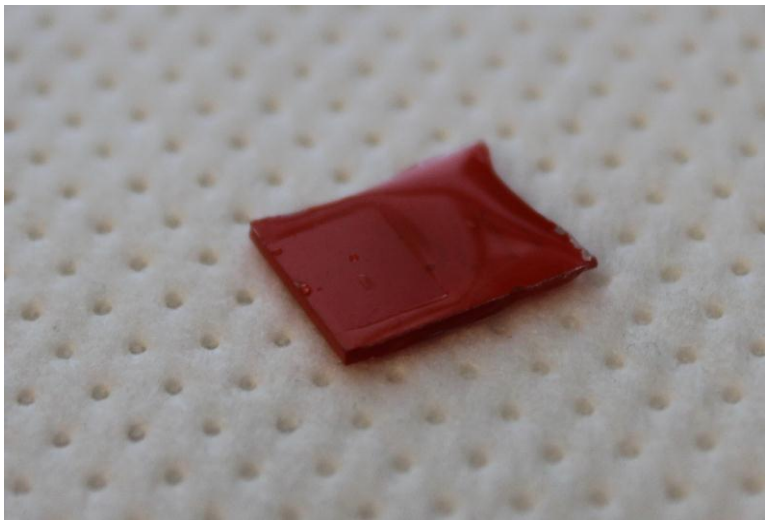

Figure 16 – De-ionized water on oxygen RIE etched enamel surface.

4.4 – Relative Permittivity Measurements

Understanding the dielectric properties of the cross-linked enamel is important for its use as a microelectronic material for applications including electronics and microelectromechanical systems [22]. The dielectric constant of a material can be expressed at the relative permittivity (ε_r) of a material, which is a unit-less constant relating the dielectric constant of a material to the permittivity of free space (ε_0 = 8.854 x 10^{-12} F/m) [23, 24]. One simple technique to measure the relative permittivity of a dielectric is to construct a simple parallel plate capacitor [23, 24, 25]. A parallel plate capacitor consists of two parallel conducting plates of area A separated by a dielectric material of thickness d. As long as the area of the capacitor A is much greater than the dielectric thickness d, the fringing fields formed along the edges of the capacitor can be

ignored [24, 26]. By neglecting these fringing field effects, the capacitance of the structure can expressed as:

$$C = \varepsilon_0 \varepsilon_r \frac{A}{d}$$

This can be rewritten to solve for ε_r such that the equation becomes:

$$\varepsilon_r = C\left(\frac{d}{\varepsilon_0 A}\right)$$

Using this relation, the capacitance can be measured for a dielectric material of known thickness placed between two conductors of known area and the unknown relative permittivity computed.

Quantifying ε_r for the high-temperature enamel under study is critical as this property will influence the electrostatic characteristics of structures realized herein. Once measured, the relative permittivity can be used for the design of the electrostatic structures realized in later chapters.

4.4.1 – Experimental Procedure

Measurement of the relative permittivity of the high-temperature enamel was performed on parallel-plate capacitors realized via a simple 3-layer shadow-mask patterning process. The area of the capacitors is nominally 10 mm by 10 mm to ease in capacitive measurements and minimize fringing field effects. Shadow masks were cut from a 125 µm thick polyester film (3M part CG3700) using a CO_2 laser system (Versalaser Inc.). The two shadow masks for the top and bottom conductive plates are identical and each consist of a 10 mm by 10 mm square plate patterned with a 750µm wide, 4.5mm trace terminated with a 1.5mm by 1.5mm square pad on one side to

facilitate probing. The third shadow mask, used for the dielectric layer, consists of a 13mm by 18.5mm rectangle to minimize the edge effects of the shadow mask on the capacitance.

Fabrication begins by cleaning as-received soda lime glass slides (Corning 0215) in acetone and ethanol before drying them using compressed air. The bottom shadow mask was then aligned to the substrate and affixed with polyimide tape. A 250nm thick layer of gold was then sputtered onto the substrate using a Cressington 108 sputtering system. After deposition, the shadow mask was removed and the gold thickness was verified using a KLA Tencor P-2 profilometer.

The dielectric layer shadow was next aligned and affixed with polyimide tape. Deposition of the aerosol enamel followed the procedure outlined in section 1 of this chapter with one modification. After spray coating the capacitors, the enamel was allowed to air dry for 10 minutes. The polyester shadow mask was then removed from the sample. The device was then placed onto a hotplate and cured at 250ºC for one hour as per the standard procedure. Removal of the mask was necessary due to thermal limitations of the polyester film and to ensure the shadow mask does not adhere to the underlying substrate. Once cured, the samples were allowed to cool to room temperature and the dielectric film thickness was verified by stylus profilometry.

Finally, the top electrode shadow mask was aligned and affixed to the substrate. A 250nm gold layer was sputtered under the same conditions as the bottom gold plate. After deposition, the shadow mask was removed, film thickness verified, yielding a parallel plate capacitor for measurement.

Lateral dimensions of the fabricated capacitors were measured using optical microscopy, and film thickness via stylus profilometry, to account for process variations and alignment issues. Electrical measurements were performed by probing the capacitor pads on a standard probe station (Karl Suss PM5). The performance of the parallel-plate capacitors were subsequently characterized using an Agilent E4980A LCR meter, and the effective permittivity and dissipation factor of the enamel computed for multiple frequencies.

4.4.2 – Measurement Results

An Agilent E4980A LCR meter was calibrated and measured against a known standard to verify proper configuration prior to performing measurements [27]. The quality factor Q as well as the capacitance and associated resistance were taken for both the series and parallel capacitance models for comparison on the unknown enamel dielectric for analysis at multiple frequencies as shown on

Table **6**. The capacitance value and capacitor dimensions were subsequently used to compute the relative permittivity of the cross-linked enamel for all measured frequencies. The dissipation factor D of the dielectric (Q^{-1}) was similarly computed.

Table 6 - Parallel Plate Capacitor Measurements at $1V_{pp}$

Property	**Measurement Frequency**			
	1kHz	**100kHz**	**1MHz**	**2MHz**
C_{series} (pF)	175.7	171.9	173.2	180.9
R_{series} (Ω)	5.9k	106	40	17
Q	152	87	23	26
D	0.007	0.011	0.043	0.038
$C_{parallel}$ (pF)	175.7	171.9	172.9	180.6
$R_{parallel}$ (Ω)	138M	807k	21k	11k
Computed ε_r	3.1	3.0	3.1	3.2

4.5 – Summary

In this chapter, a high-temperature dielectric enamel has been introduced for use with inkjet printed gold microelectromechanical systems. Suitable deposition and curing conditions were identified which yield a surface suitable for the subsequent deposition of hexanethiol gold nanoparticles immersed in α-terpineol. Films spray deposited from an aerosol precursor onto Corning 0215 glass were robust when immersed into many solvents useful for inkjet printing applications. An initial reactive ion etch study was performed which yielded a maximum etch rate of 0.53 μm min^{-1} using oxygen and tetrafluoromethane etch gases. RIE etching incompletely removed all components of the enamel, leaving behind particles which could be subsequently removed in ultrasonically agitated water. Parallel plate capacitors were realized using the high-temperature enamel and these capacitors were characterized using an Agilent E4980A LCR meter in order to determine the relative permittivity of the cross-linked films and varied between 3.0-3.2 for frequencies between 1kHz-2MHz. These characteristics are compared with two common polymers for electronics in Table 7.

Table 7 – Dielectric Properties of Polymers for Electronics

Material	**Dielectric Constant**	**Dissipation Factor**	**Reference**
Parylene-C	3.10 -1kHz 2.95 - 1MHz	0.019 -1kHz 0.013 - 1MHz	[28]
Polyimide	3.4 -1kHz	0.0018 -1kHz	[29]
Enamel (This work)	3.10 -1kHz 3.10 - 1MHz	0.007 -1kHz 0.043 - 1MHz	-

Overall, the measured characteristics of the high-temperature enamel suggest it is an attractive dielectric material for the development of inkjet printed microelectromechanical systems. Further, as the enamel can be spray coated from an aerosol precursor, the material offers further utility as a surface pretreatment to homogenize the surface properties of different base substrate materials in order to simplify the development of inkjet printed MEMS process conditions.

5. Sintered Gold Nanoparticle Films

This chapter explores the characteristics of inkjet patterned gold films deposited as hexanethiol-encapsulated gold nanoparticles and subjected to post-deposition thermal sintering processes. Recall from Chapter 2, that post-deposition thermal steps are used to evaporate the carrier solvent, sublimate the hexanethiol organic encapsulant, and sinter the nanoparticles into a coherent gold structure. The moderate heating of hexanethiol gold nanoparticles in air on a hotplate has been demonstrated as an effective means to render conductive gold films for printed electronics applications [1] and the electrical properties of Au-NPs have been characterized for printed films for electronics [2].

Other techniques including laser sintering [3], gaseous sintering in NO_2 [4], and UV irradiation [5] have also been demonstrated as a means for generating conductive gold nanoparticle films. However, these techniques require additional equipment of varying degrees of cost and complexity over a simple hotplate sintering process. As a heated platen is already required for gold nanoparticle deposition, the development of a sintering technique using a hotplate allows for straightforward sintering integration for the realization of complex inkjet printed microstructures.

In this chapter, properties of sintered gold films will be explored on both Corning 0215 soda lime glass and the aerosol deposited high-temperature dielectric material introduced in the previous chapter. Section 3.5 observed that resolution jet deposited Au-NPs depended on the underlying substrate, so it is of interest to study additional properties on both of these materials to garner an understanding of the electrical and physical properties of the resulting gold films after sintering.

Monitoring either the resistivity or the color of Au-NP films is the traditional method to determine sufficient sintering duration, and sintering is typically ceased shortly after a gold colored conductive film develops [2, 6]. In this chapter, the sintering process of inkjet printed hexanethiol gold nanoparticle films will be monitored electrically to watch resistive behavior during sintering under multiple sintering temperatures and film thickness, as well as on multiple substrates. The sintered gold films will be imaged using scanning electron microscopy to gain insight on the microstructure of the material as a result of differed sintering conditions. As the stiffness of a material is a useful design parameter for the design of MEMS, the gold films are studied using nanoindentation to gain an understanding of the evolution and stability of the stiffness for differed sintering durations. As this research seeks to develop a jet printed manufacturing process for the realization of gold microelectromechanical systems, understanding the evolution of the mechanical properties of printed gold films is critical. The measurements of the electrical, mechanical, and microstructures properties as a function of sintering conditions can be correlated to determine suitable deposition and thermal sintering conditions towards the realization of printed gold MEMS.

5.1 – Resistivity versus Sintering Conditions

This section explores the evolution of the resistivity of inkjet printed hexanethiol-encapsulated gold nanoparticles as a function of film thickness, sintering temperature, sintering duration, and substrate material. Understanding the evolution of the resulting gold films as a function of these parameters will enable the selection of an appropriate sintering condition or conditions for printed microfabrication.

5.1.1 – Resistivity versus thickness

While the sintering conditions necessary to sublime the organic precursor and sinter the nanoparticles together in order to yield conductive gold has been studied extensively by Huang *et al.* [1] for single printed layers, the sintering time for varied thicknesses has not been reported and is of interest for structural applications, as multiple layers of ink may be necessary. This study explores the conductivity of multiple thicknesses of printed gold nanoparticles over the course of a 60 minute sintering process.

Hexanethiol-encapsulated nanoparticle ink (10%wt, 60µm diameter nozzle) wires were printed between two 25µm thick silver epoxy (Chemtronics CW2400) pads spaced 10 mm apart on clean soda lime glass slides (Corning 0215). These wires were fabricated with one, two, and three deposition layers (printing passes) to vary the initial thickness. After deposition, the films were left on the printer at 130°C for 10 minutes to evaporate the α-terpineol solvent. The as-deposited films were then placed on a 200°C hotplate in air, and the film resistance between two adjacent silver pads was measured regularly using an Agilent 34401A digital multimeter until a total sintering time of 60 minutes was reached. After annealing, a Dektak 3030ST stylus profilometer was used to measure film thickness and cross section profile. Conductivity measurements of the printed wires are shown in Figure 17.

Line widths for the wires were 88, 101, and 103µm for one, two, and three passes of the printer, respectively. Initially, the resistance of the films was beyond the range of the multimeter, but dropped to ~55MΩ-cm after 1 minute of annealing. The resistance of all three films remained above 20MΩ-cm before rapidly decreasing, as expected from the literature.

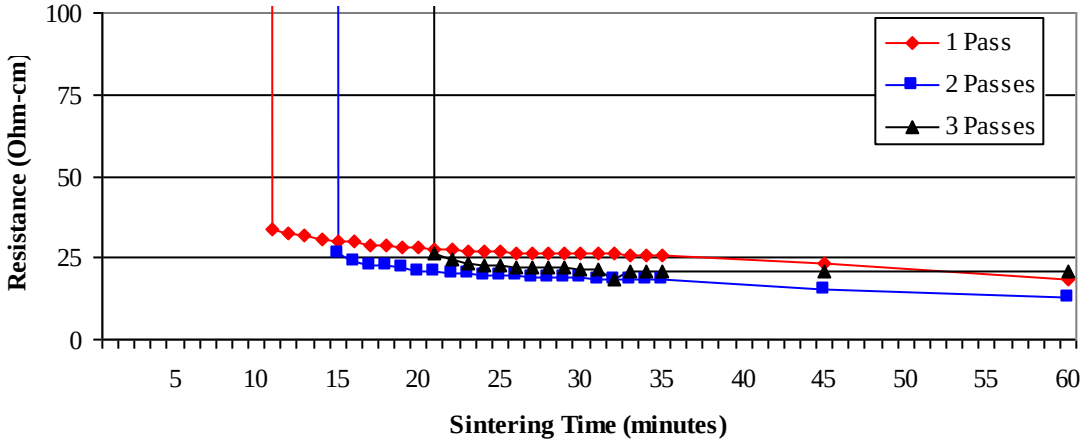

Figure 17 - Film resistance versus sintering time. Initial film resistance was measured to be >20MΩ-cm prior to the large resistance drops observed which indicate the onset of gold sintering.

For a single pass, the resistance drop occurred after 11 minutes, which agrees well with Fuller *et al*, [6]. The thicker films took measurably longer, with the resistance change occurring at 15 minutes for two passes, and 21 minutes for the three pass thick wire. Measurements were continued for 1 hour, and a slight drop in resistance was recorded, until final resistances of 18.3, 12.7, and 13.6 Ω-cm were measured for the one, two, and three layer thick films. After sintering, the film thicknesses were measured and estimated to be 340nm, 599, and 839nm for the one, two, and three layer films.

The observed increase in time before the onset of sintering for different film thicknesses is likely due to the increased time required to sublimate the hexanethiol SAM from the nanoparticles. As such, thicker films will likely require longer minimum sintering times in order to yield conductive films. It should also be noted that the resistance continues to drop slightly as sintering is continued for a full hour. This appears

to indicate that changes in the gold structure are still occurring, which may be affecting its mechanical properties.

5.1.2 – Resistivity versus Sintering Temperature

The effect of sintering temperature was next studied over a range of temperatures high enough to induce sintering, but low enough to be useful for printing on polymeric materials. Using the minimum sintering temperature necessary to yield suitable gold films is desirable in order to maximum the number of materials which are thermally compatible with the Au-NP deposition process. Also, a reduction in sintering temperature will reduce stresses imparted on the fabricated devices layers due to coefficient of thermal expansion (CTE) mismatches between the materials used in manufacturing.

An improved 4-point resistivity measurement was used for this experiment and is detailed in Section 6.1. Clean soda lime glass sides (Corning 0215) were prepared and patterned with the "H" test structure used in this technique. The test structure consists of two parallel 250nm thick sputtered gold traces measuring 600µm wide by 10mm long, spaced 900µm from one another and terminated with silver epoxy pads at each end. The sputtered hexanethiol-encapsulated gold nanoparticles (15%wt in α-terpineol) were deposited using a 30µm diameter nozzle in two passes orthogonally across the sputtered gold traces to form a Au-NP bridge. The as-deposited Au-NP ink was then placed on a hotplate in air at 140°C to allow solvent evaporation and 4 point resistivity measurements were started at a sample rate of 1Hz. After 10 minutes the hot plate was ramped to the final sintering temperature (150, 175, 200, or 225°C) and the resistivity was recorded for a total of 2 hours in air. This process was then repeated for each of the remaining samples. Results of these measurements are plotted in Figure 18. At first, the film is

highly resistive but this decreases as the hexanethiol sublimes, allowing adjacent gold nanoparticles to come into contact and conduct. As the organics leave the film a sharp decrease in resistance is observed as the gold forms a conductive structure and sinters together.

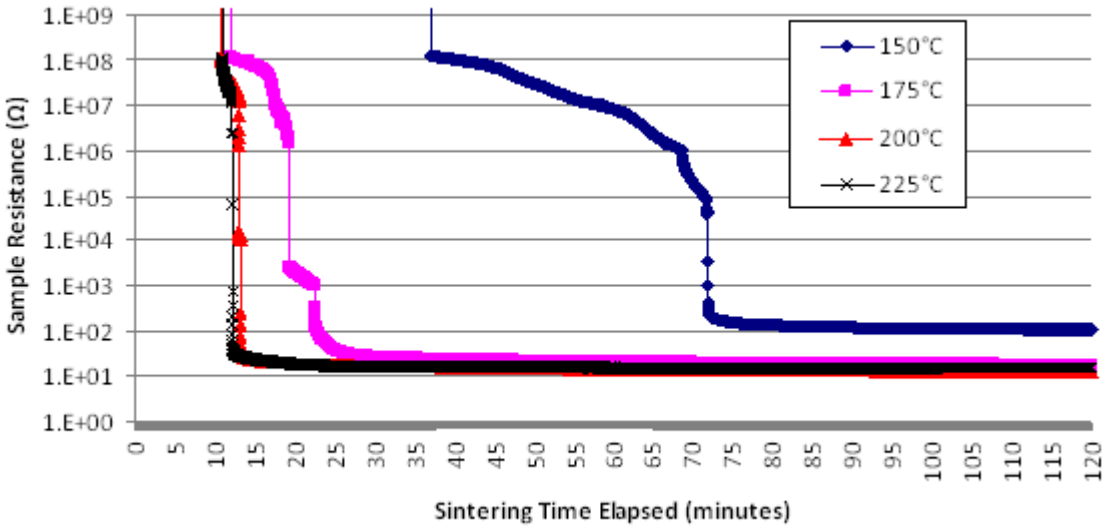

Figure 18 - Resistance versus time of Au-NP films sintered at different temperatures on Corning 0215 glass,

As the sintering temperature is decreased, the necessary time required for the sintering process to occur increases. Resistivity decreases 2 minute and 3 minutes after the hot plate is increased for 200°C and 225°C, respectively. At 175°C, an addition 15 minutes is required, while it takes an hour for the nanoparticles to undergo sintering at 150°C. The resistance of the film sintered at 150°C remains an order of magnitude higher than other films, indicating that the resulting film may not have reached the same level of change as the other gold films. It is also observed that the 175°C film

demonstrates a second plateau layer, which can also be slightly observed for the 200°C sample. It is hypothesized that this plateau is the region where the organic encapsulant material has sublimed and the Au nanoparticles are beginning to sinter together into a more conductive gold film. This experiment indicates that sintering can be performed at lower temperatures, but a longer duration is required to yield conductive gold films.

5.1.3 – Film Resistivity for Extended Sintering Durations

After the dramatic decrease in resistivity with the onset of sintering, the resistivity of the film appears relatively stable for lengthened sintering durations. As the development of printed microelectromechanical systems will require the deposition of multiple device layers, printed gold films may experience long durations of elevated temperature during the microfabrication process. To explore the long-term changes in resistance, the 200°C sample from the previous study was left on the hotplate and monitored for a total sintering time of 345 minutes in air. Results of the measurement are shown in Figure 19. The resistance of the film continues to decrease, ultimately decreasing by a factor of two compared to the line resistance at 15 minutes before stabilizing. This measurement indicates that the sintered nanoparticle films may still be evolving immediately after the large resistivity change, so an extended sintering step may be required such that all films in a complex printed device will have similar properties.

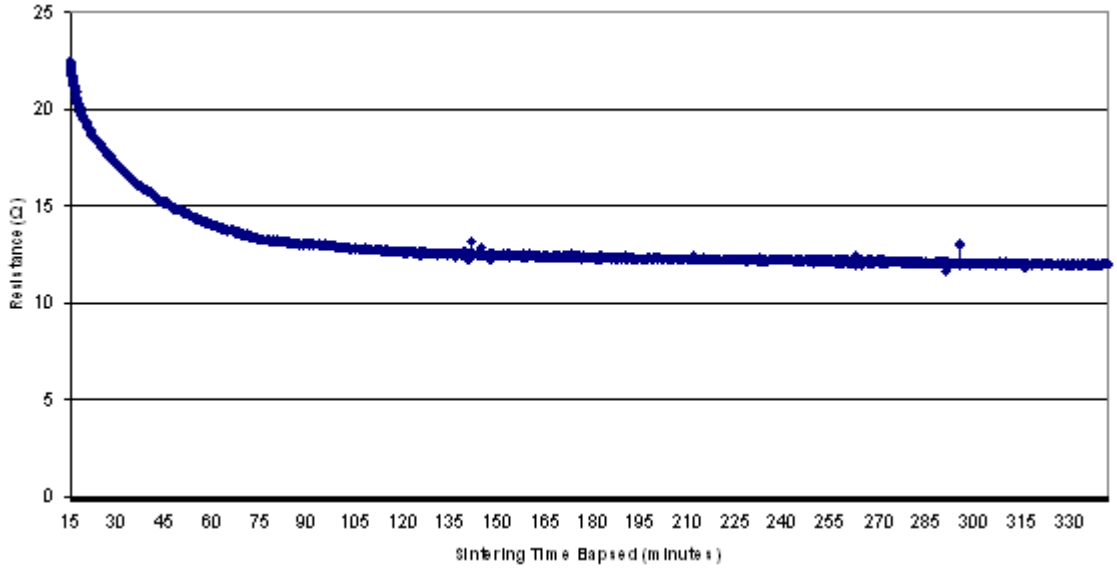

Figure 19 - 200°C Au-NP on glass resistance showing continued long term evolution of resistance to a total sintering duration of 345 minutes.

5.1.4 – Resistivity for Different Substrate Materials

The resistivity behavior during sintering was next explored for films deposited identically onto two different substrates. Two substrates were patterned with the "H" shaped test structures described in Section 6.l; clean soda lime glass (Corning 0215), and the high-temperature enamel, prepared according to Chapter 5. The test structures each consist of two 250nm thick sputtered gold traces, each 600µm apart, and spaced 900µm from one another. Hexanethiol-encapsulated gold nanoparticles (15%wt in α-terpineol) were deposited using a 30µm diameter nozzle in two passes orthogonally across the sputtered gold traces to form a Au-NP bridge. The as-deposited Au-NP ink was then placed on a hotplate in air at 140°C to allow solvent evaporation and 4 point resistivity measurements were started at a sample rate of 1Hz. After 10 minutes the hot plate was ramped to the final sintering temperature of 200°C and the resistivity was recorded for a

total of 30 minutes in air. The process was then repeated for the second sample and the results are plotted in Figure 20 and Figure 21. The gold nanoparticles printed onto enamel exhibit a sharp drop at the 12 minute mark with less time spent at the second plateau. The gold nanoparticles on Corning 0215 glass take much longer to reach the first large resistance drop and then remained at a second plateau for several seconds before proceeding to a low resistance value. This data suggests that the substrate plays a role in the necessary sintering conditions. To more fully understand these materials, these samples will be imaged using scanning electron microscopy in the next section.

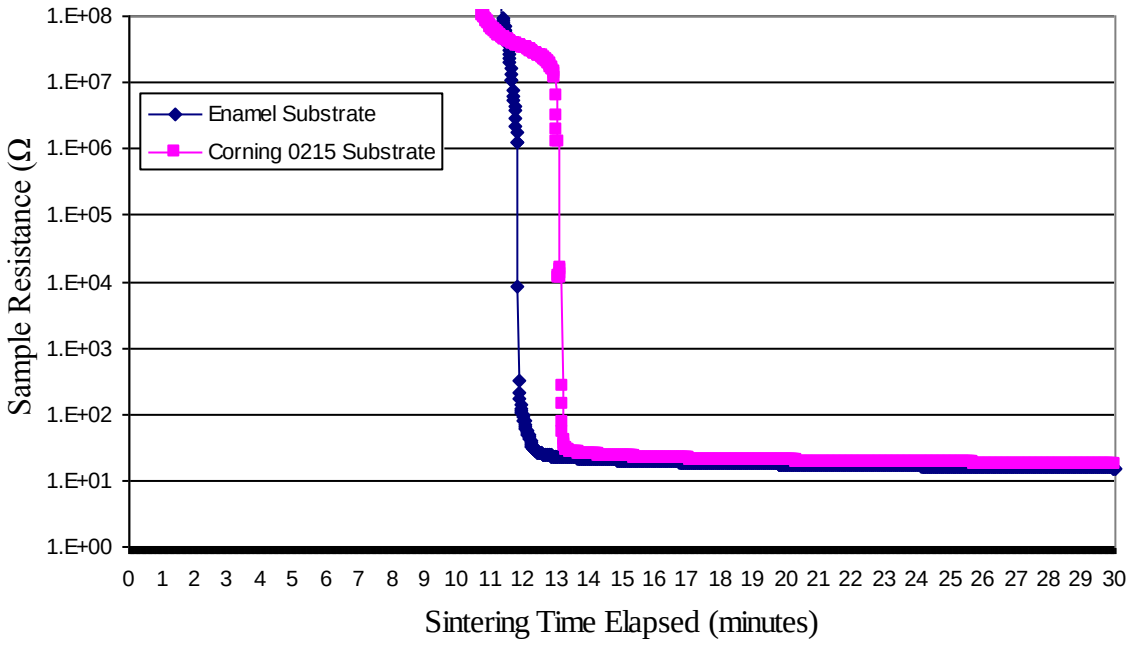

Figure 20 - Resistance evolution of Au-NP lines printed on different substrates at 200°C.

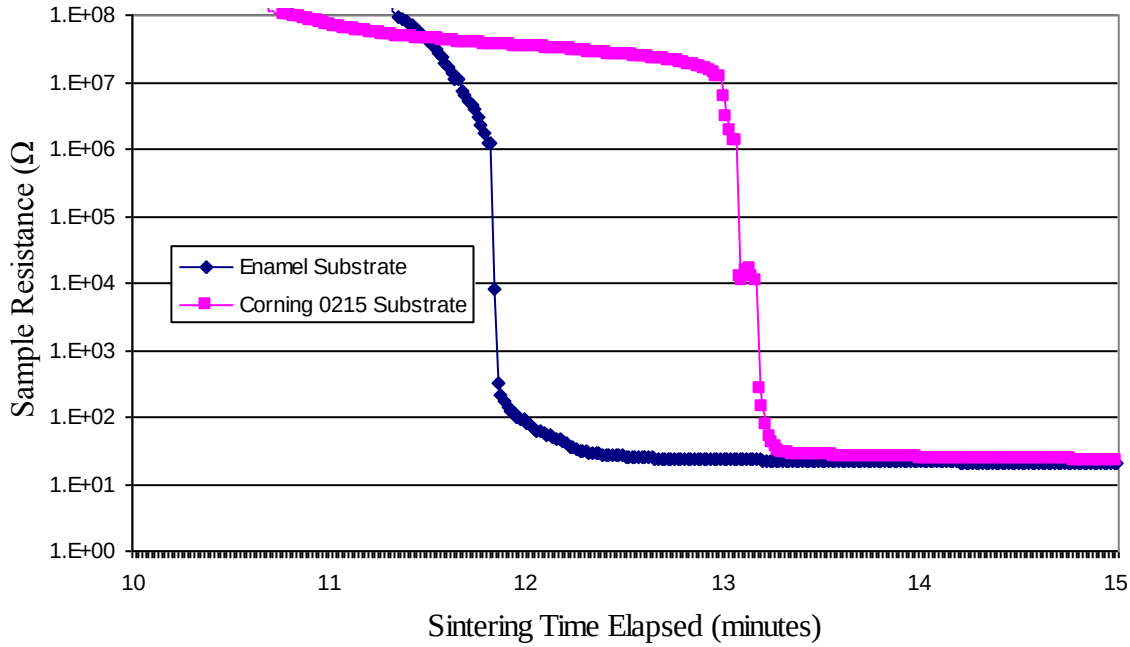

Figure 21 - Zoomed view of resistance transition period for Au-NP lines printed on different substrates sintered at 200°C

5.2 – Microstructure versus Sintering Conditions

As the nanoparticle sintering process is driven by the thermal energy provided by the hotplate, the resulting gold films may have different microstructural characteristics due to process temperature variation. In order to gain an understanding of this resulting microstructure, imaging of the samples was performed using scanning electron microscopy (Hitachi S-4500). Sintered gold samples prepared on both Corning 0215 glass and high-temperature enamel are explored.

5.2.1 – Microstructure of Sintered Au-NPs on Corning 0215 Glass

The films prepared on Corning 0215 glass for the resistivity versus sintering temperature measurements (section 5.1.2) were all sintered for a full 24 hour period at their respective temperature to normalize the sintering duration of each sample. Samples of gold sintered at 150°C, 175°C, 200°C, and 225°C were then imaged as shown in Figure 22 and Figure 23 under increasing magnification. Samples were not sputter coated before measurement to enable their reuse in further measurements.

While all films studied are electrically continuous, imaging reveals that their sintered characteristics are far from the simple solid beam of ink originally deposited onto the glass substrate. The sintering process has changed all gold films into a highly porous material. The film with the smallest pore size observed was the sample sintered at 175°C.

The mechanisms of sintering and coalescence of gold nanoparticles films has been studied extensively [7-14]. These observations match the description put forth by Eggersdorfer *et al*., who explain that during the sintering process, gold nanoparticles undergo a transformation to reduce free energy through multiple mechanisms [15]. In doing so, the gold nanostructures transform into "fractal-like" shapes, which can be readily observed in the repeating pores observed in all sintered films imaged in this study.

From an engineering standpoint, while these gold films form conductive gold films, their porous nature makes them highly undesirable for use as a mechanical or structural material. On the 225°C sample, the printing system did not shut off the nozzle immediately at the end of the printing run, resulting in a large pool of ink at the end of the line. Upon further inspection of this region (Figure 24 and Figure 25), the sintered gold

formed into a more dense gold film suitable for microfabrication applications. The printed Au-NP inks undergo measurable volume contraction as the organic encapsulant sublimed, the as-printed film which appeared solid prior to sintering had insufficient gold nanoparticles to form into a dense printed gold layer. To develop printed Au-NP on Corning 0215 films into a suitable material for printed MEMS, further process development is needed to deposit sufficiently thick films to yield dense gold structures.

The soda lime glass substrate may play an important role in the results of this study. Conventional gold films exhibit poor adhesion when deposited onto glass and require the use of a thin adhesion promoting seed layer such as titanium or chromium deposition. Au-NP films deposited onto a glass substrate with an adhesion promoter should be explored to see if the morphology of the sintered gold films can be improved. One candidate material shown to adhere readily to Corning 0215 glass is the aerosol deposition enamel introduced in the previous chapter and is imaged in the next section.

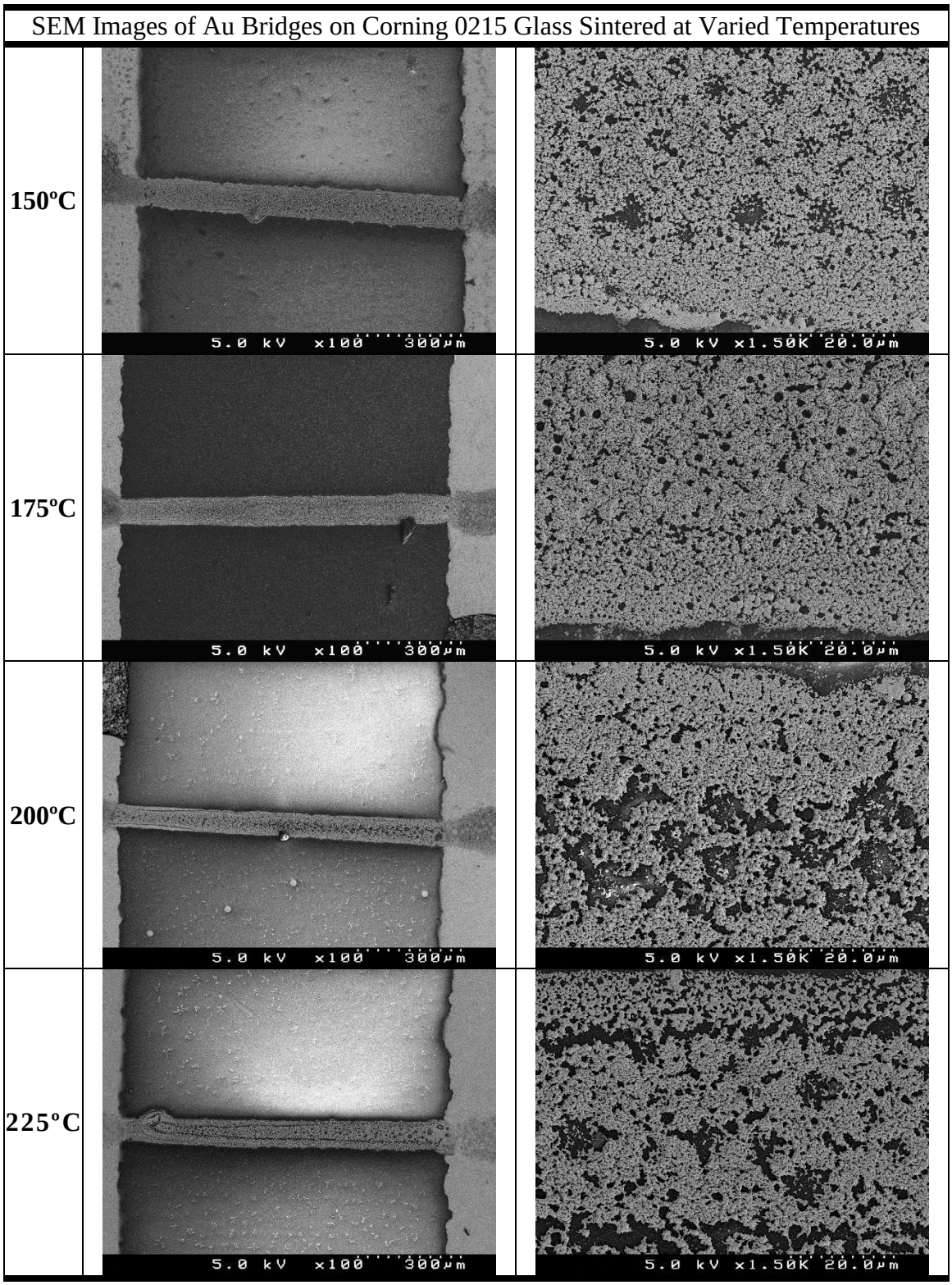

Figure 22 - SEM Images of Sintered Au-NPs on Corning 0215 Glass after 24 hours at varied temperatures (1 of 2).

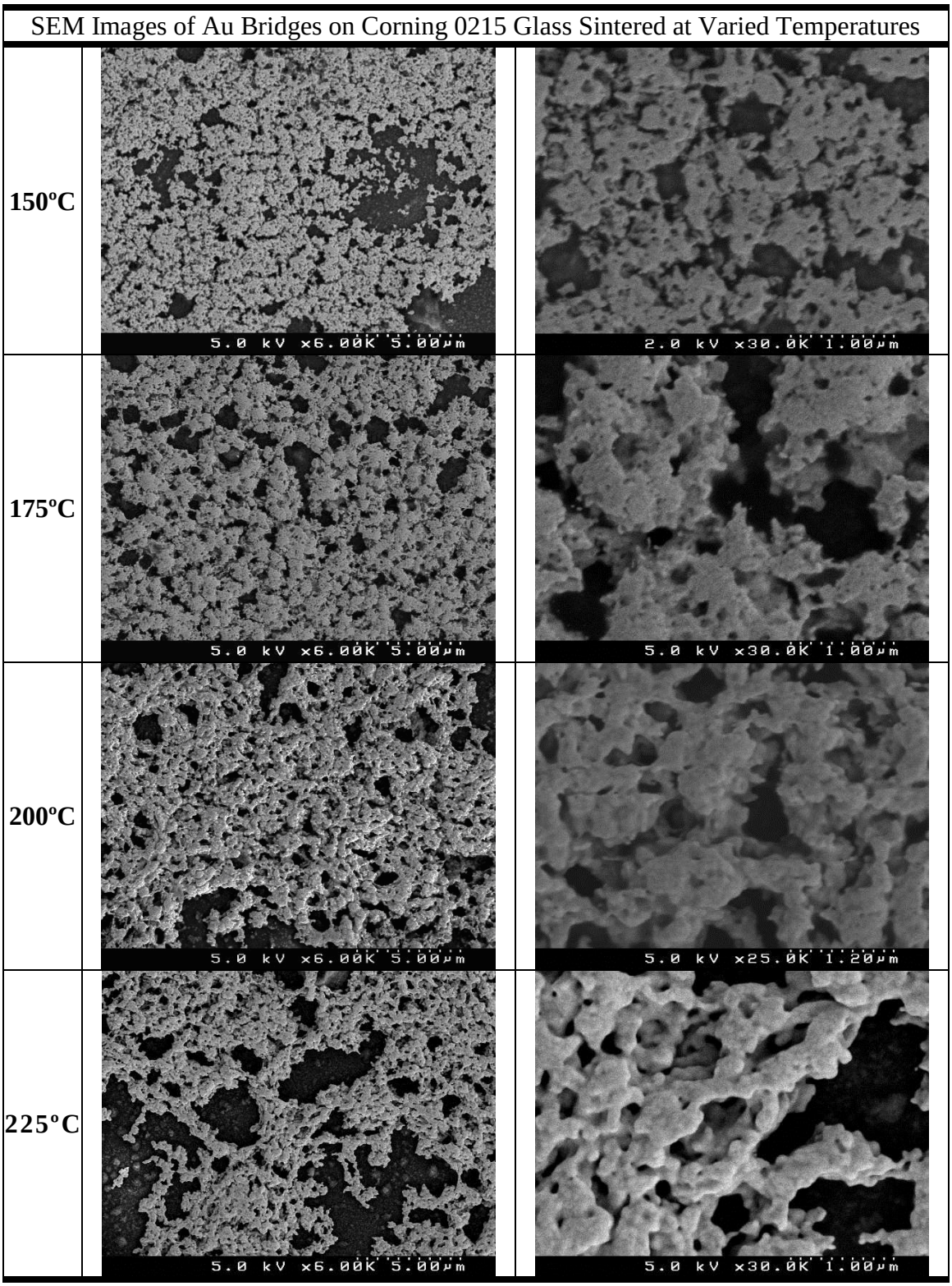

Figure 23 - SEM Images of Sintered Au-NPs on Corning 0215 Glass after 24 hours at varied temperatures (2 of 2).

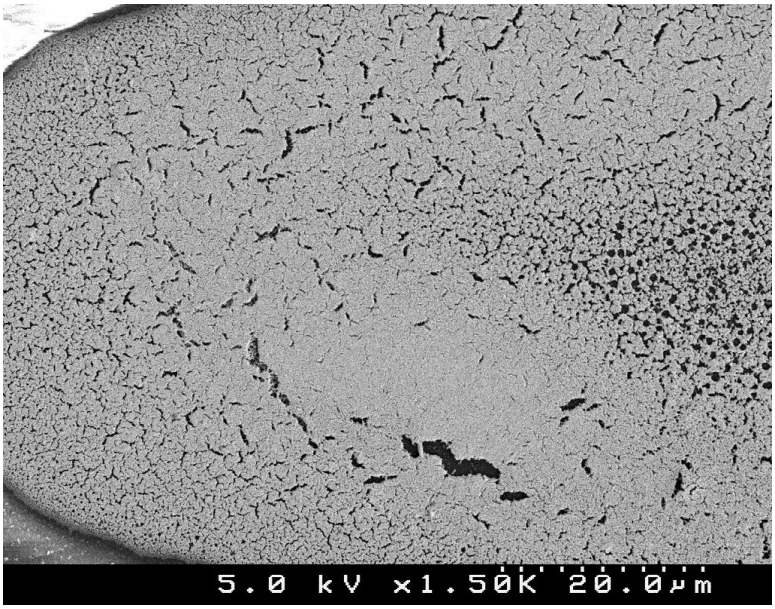

Figure 24 - Thick sintered gold film sintered at 225°C.

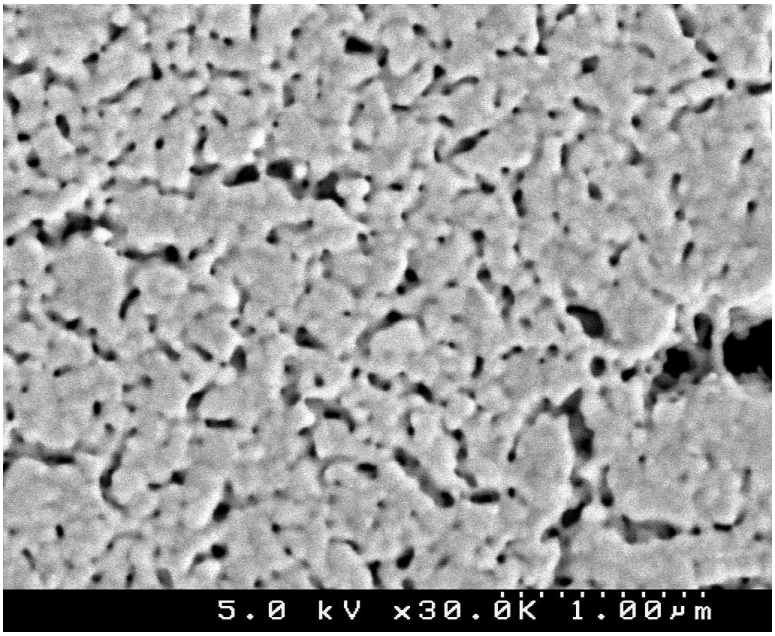

Figure 25 – Close-up of thick sintered gold film sintered at 225°C.

5.2.1 – Microstructure of Sintered Au-NPs on Enamel

As the aerosol deposited enamel introduced in chapter 4 is of interest as a surface treatment and dielectric material for inkjet deposited MEMS, sintered gold films deposited onto it were examined. Hexanethiol-encapsulated gold nanoparticles were synthesized and suspended in α-terpineol (15%wt) forming the ink which was subsequently loaded into an inkjet head with a 30μm diameter piezoelectric nozzle. The print-head was driven with a 20Hz bipolar waveform (Chapter 3) using 2/5/2/5/2μs timing parameters at ±30V. Each gold layer in the processed film is patterned through two successive passes onto a 140°C platen yielding a film thickness of 1.9μm and a line width of 80±10μm. The motion velocity of the printer was set to overlap two consecutive droplets by 50%. After deposition the bottom gold structures were held at 140°C for 30 minutes to fully drive off solvent and then ramped to 200°C and held for 60 minutes in air to sinter the Au-NPs into a gold film. Scanning electron microscopy images of the resulting sintered Au-NP film on enamel are shown in Figure 26. (a) Shows a trace deposited onto an 18μm thick dielectric material which was cured on a hotplate for 1 hour at 60°C prior to Au-NP deposition. The holes in (a) appear to be vents formed to exhaust solvent vapors. (b)-(d) are SEM images of increased magnification on (a) to highlight the structure of the sintered gold film. (e)-(f) show the porous edges found along the length of the printed feature on (a). (g) shows a portion of the sintered gold film which was deposited on enamel which was cured for 1 hour at 250°C. This films lacks the vents found in (a) and appears dense on the surface as shown in (h). Sintering of Au-NPs on aerosol enamel generates a film which is promising candidate material for the realization of inkjet printed gold MEMS and its properties should be further characterized.

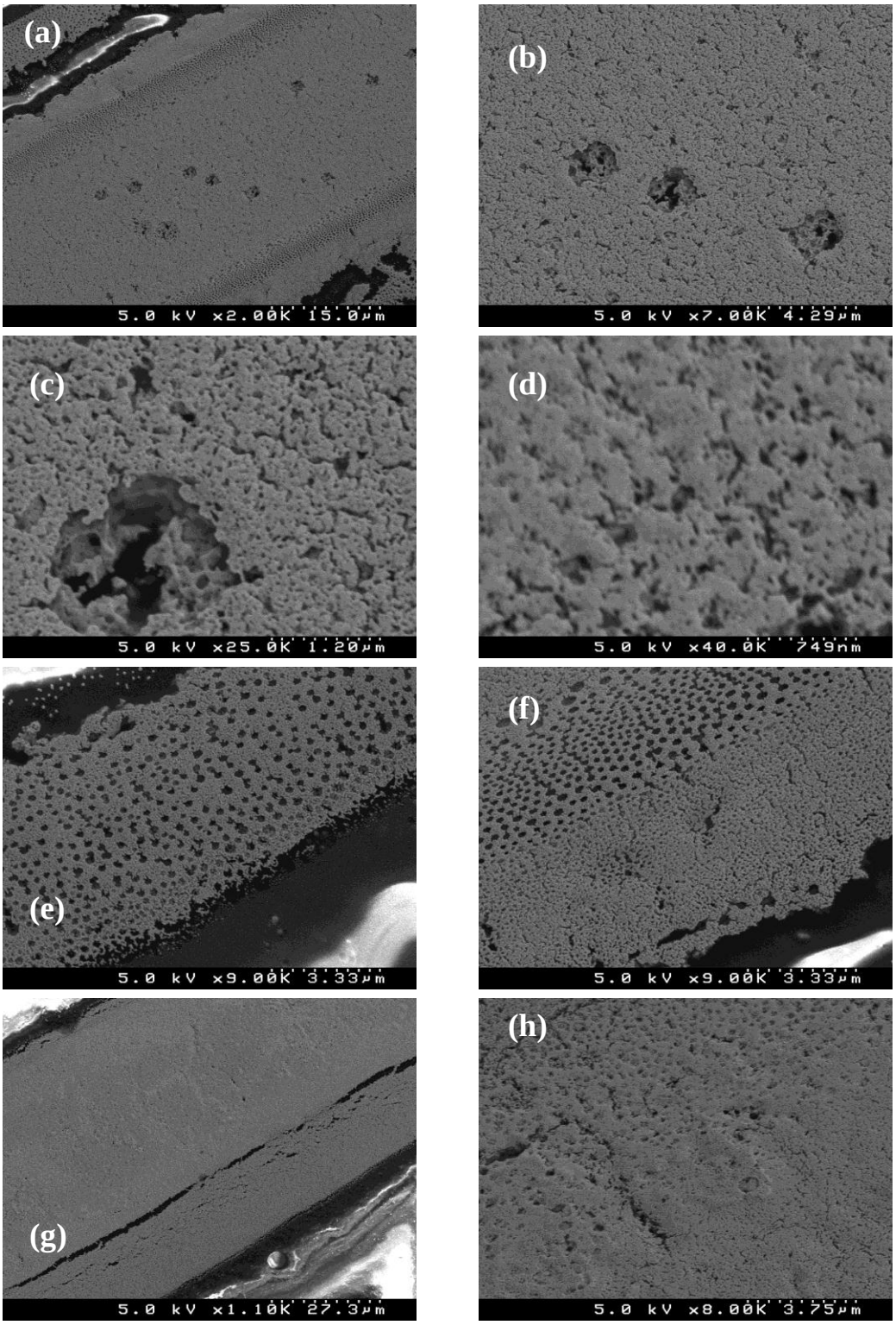

Figure 26 - SEM images of sintered Au-NP on enamel. Refer to text on previous page for details.

5.3 – Stiffness versus Sintering Conditions

In order to gain an understanding on the evolution of the mechanical characteristics of gold films realized by sintering hexanethiol-encapsulated gold nanoparticles, initial stiffness studies of sintered Au-NP films are detailed in Appendix C. There, continuous stiffness measurement (CSM) nanoindentation measurements are detailed for sintered gold films patterned onto <100> silicon and dielectric enamel substrates then sintered for multiple durations of up to an hour. These measurements indicate a trend of increasing stiffness of the sintered Au-NP films as the sintering duration is extended beyond the onset of sintering. This trend follows that of the film resistance during sintering. It is advisable to sinter gold nanoparticles for an extended period of time beyond the onset of sintering as observed by a color or conductivity changes as is currently suggested in the literature in order to minimize material variation due to subsequent temperature process steps. Accordingly, an extended sintering duration of one hour at 200°C is selected for further development.

5.4 – Summary

This chapter has explored the characteristics of gold films realized from an inkjet deposited hexanethiol-encapsulated Au-NP ink and sintered on a hotplate in air. Resistance measurements of gold films of different thicknesses, sintered at different temperatures, and on different substrates were performed, revealing that all of these parameters affect the resistance profile during the sintering process. Additionally, this chapter extended the sintering duration to find that the resistance of the gold film continues to change well after the rapid change in resistivity due to the onset of sintering is observed. Initial CSM nanoindentation measurements were performed revealing a

trend of increasing stiffness of sintered gold which continues for beyond the onset of sintering.

The microstructure of sintered gold films was examine using scanning electron microscopy which reveal vastly different films defending on substrate type for given parameters. The high-temperature enamel yielded a coherent looking gold structure, while gold printed on Corning 0215 soda lime glass formed highly porous microstructures. The highly porous film that resulted under these conditions is not suitable for MEMS structural materials, but its properties will be explored in the next chapter. The gold on enamel microstructure presents a promising set of process materials and conditions useful for the realization of inkjet printed gold microsystems.

6. TCR of Printed Au Thin Films

This chapter presents the thermoresistive characteristics of hexanethiol-encapsulated gold nanoparticles (NPs) inkjet printed onto both Corning 0215 soda lime glass and high-temperature enamel. Printed gold films differ from other common semiconductor and MEMS deposition techniques in that they are formed from metallorganic nanoparticle having undergone thermal steps to sublimate organics and induce NP sintering. The resulting films can have microstructure which differs greatly from other metal deposition techniques, giving rise to unique material characteristics. Exploiting the unique properties of sintered NP films may enable new sensors and actuators, making it of keen interest for the field of printed microsystems.

Resistive sensors using alkanethiol-encapsulated gold nanoparticles have been widely studied in the literature for unsintered gold films. The encapsulated nanoparticles have shown promise as chemical sensors for both liquid and gaseous species [1, 2, 3]. Leung *et al*. also demonstrated that thin strands of unsintered gold nanoparticles are useful for temperature sensing [4]. A drawback of these devices is that the organic encapsulant breaks down over time, degrading sensor performance. While unsintered gold nanoparticles have shown utility for resistive sensing, no examples of sintered gold nanoparticle films were found in the literature, further motivating the need for a measurement of the thermoresistive response towards inkjet printed sintered gold sensors.

6.1 – 4-Point Measurement Configuration

Four-point, or Kelvin probe, resistance measurements are commonly employed to minimize measurement error due to the resistivity of the test setup. In this technique, a current source is used to energize the sample while a voltage meter measures the voltage drop across a known geometry. As the voltage meter draws very little current, errors such as spreading and contact resistance are minimized [5]. In conventional subtractive microfabrication, a collinear probe is commonly used to measure the four-point sheet resistance on just deposited materials prior to lithographic patterning [6]. For inkjet printed microfabrication, accurate measurement of film resistance is of high importance. However, for printed applications, the use of a conventional collinear Kelvin probe may prove challenging. Microfabricated cross structures have been realized for four-point measurements as an alternative to a collinear probe [7, 8]. Simple microfabricated bridge structures have also been developed for the measurement of sheet resistance [8, 9]. For inkjet printing, a simple bridge structure can be formed through the deposition of a straight line. To interface with this bridge for measurement, a test structure is needed to allow measurement using a 4-point bridge morphology.

A microfabricated “H” test structure has been developed which readily allows for 4-point measurements bridges formed of inkjet deposited films. Shown in Figure 27, the test structure consists of two parallel sputtered gold traces terminated with a pad on each end. The ink under study is then printed across the parallel traces, bridging the connection. The four pads can then be electrically connected to an ohmmeter or multiple source measurement units to perform four point measurements across the bridging material.

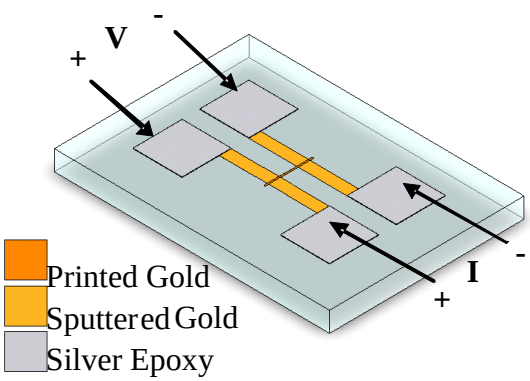

Figure 27 – "H" test structure for 4-point measurement of inkjet printed films. Instrument connections and printed device shown. The printed gold sample is the thin wire bisecting the sputtered gold traces in the center of the image.

Both a full and a simplified circuit model of the test structure are displayed in Figure 28 for measuring the resistance of a printed bridge (R_{DUT}). On each leg of the test structure there is an associated resistance due to the sputtered trace (R_{Au}), the metal pad (R_{pad}), and the connecting electrical probe (R_{probe}). For each leg of the test structure, these three resistances can be lumped into a single resistor representing the total resistance of that measurement probe. A current source can then be applied across one side of the bridge to energize the circuit while a voltmeter measures the voltage drop across R_{DUT} in order to measure bridge resistance.

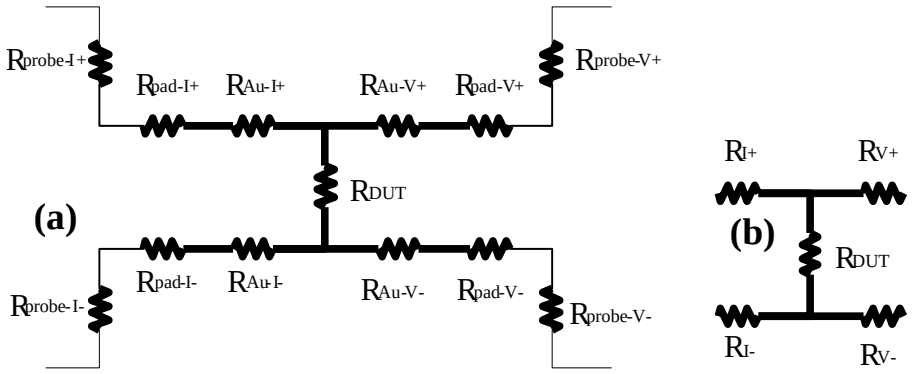

Figure 28 - Circuit models of "H "test structure (a) full model (b) lumped model.

"H" test structures were fabricated on soda lime glass (Corning 0215) or similar substrate by sputtering a 250nm thick layer of gold through a laser-cut polyimide tape shadow mask. The sputtered gold lines were 10 mm long by 600µm wide with 2.5mm by 2.5mm square pads on each end. The gap between the two gold lines, and therefore the length of an orthogonally printed bridge was nominally 1mm. The pads were coated with silver epoxy and cured for 1 hour at 250°C to enhance their robustness.

As resistance measurements were to be performed on a hot plate, a robust probing method was required to accommodate thermal expansion and uneven pad thickness. A compliant four-point probe was realized to reliably contact the "H" test structure on an arbitrary planar surface. The probe is fabricated using four spring loaded "pogo" pins, commonly used for microelectronics testing. The pogo pins used have a 1.4mm rounded tip and 6.3mm of linear travel, allowing for a reliable electrical connection to underlying pads during testing. The probe is mounted onto a boom arm to enable rapid positioning over a hotplate. Figure 29 shows the complete test setup with the spring loaded probe detailed in the two insets on the figure.

Resistive measurements using the test structure and probe were performed using a Keithley 2000 digital multimeter interfaced over GPIB to a laptop running Labview™ for data logging and control. A digital hot plate (Thermo Scientific Cimarec HP131225) provides temperature control of the sample under test.

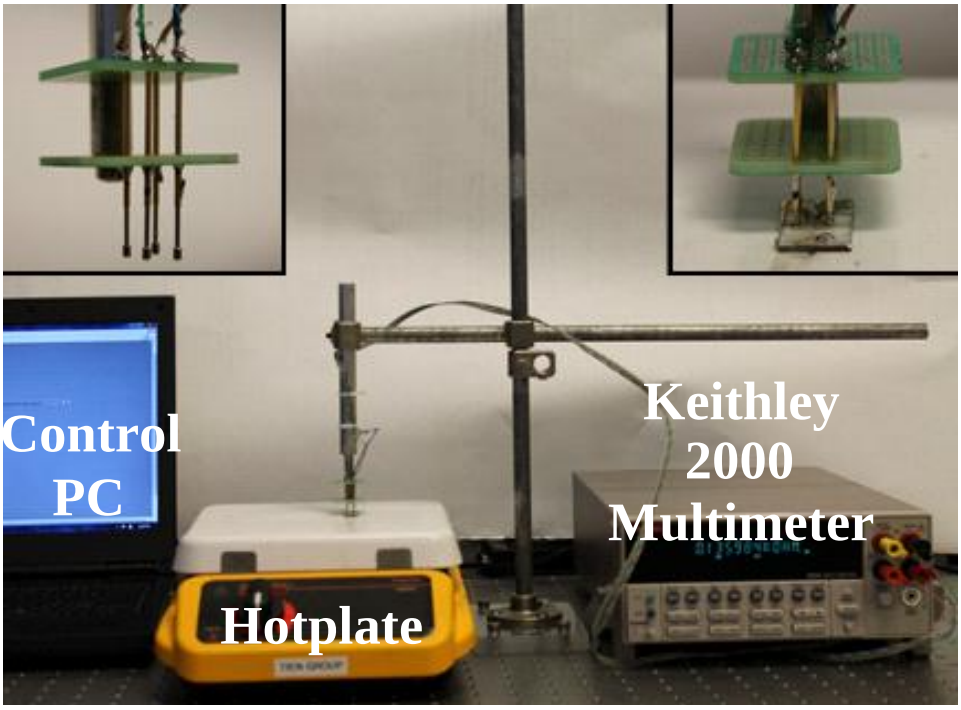

Figure 29 - Four-point resistance measurement setup over a hotplate. Insets show spring-loaded pogo-pin jig extended (L) and during operation (R).

6.2 – TCR Measurement Procedure

For this experiment, the thermoresistive response of inkjet printed Au bridges sintered under different temperature regimes was measured. 4-point resistance measurements were performed on a hotplate to characterize the thermoresistive response of the resulting microstructures between 25ºC and 150ºC. "H" test structures were

produced on two substrates: bare soda lime glass (Corning 0215) and high-temperature enamel, prepared using the standard procedure from Chapter 4. The "H" test structures were then patterned by sputtering a 250nm thick layer of gold through a laser-cut polyimide tape shadow mask of the dimensions described previously. The gap between the two gold lines was nominally 1mm. The pads were coated with silver epoxy and cured for 1 hour at 250°C.

Hexanethiol-encapsulated gold nanoparticles ink (15%wt in α-terpineol) was jet deposited using standard parameters to form a bridge across the test structures using two passes onto a 140°C platen. The as-printed devices were then pre-baked at 140°C for 10 minutes, and the hotplate was subsequently ramped to the final sintering temperature and held for 24 hours to sinter the Au NPs. The sintering temperature was fixed between 175°C and 225°C for different samples.

4-point resistive measurements were performed on each sample individual using the system described in Section 7.1. First, the sample was loaded onto the hotplate (Thermo Scientific Cimarec HP131225) and the spring-loaded probe was lowered onto the sample, making secure contact with the pads on the "H" test structure. Data acquisition (Labview^{TM}, National Instruments) was initiated at a 1Hz sample rate to record 4-point resistance measurements of the samples using a Keithley 2000 multimeter. After 10 minutes under ambient conditions the hot plate was ramped sequentially to 50°C, 100°C, and 150°C and held for 10 minutes at each temperature. After 10 minutes the hot plate was turned off and allowed to cool to ambient conditions.

6.3 – TCR Measurement Results

A photograph of an "H" test specimen with an inkjet printed gold bridge is shown in Figure 30. The line width was measured as 80µm and the bridge length was measured to be 900µm. The sintered gold bridges were imaged using scanning electron microscopy (Hitachi S-4500) to visualize the resulting film microstructure as shown in Figure 31 and Figure 32 for the sample sintered at 175°C and 225°C respectively. 4 point measurement results of the bridges were processed and plotted in Figure 33 through Figure 35. Figure 33 plots results for both the 175°C and 225°C sintered samples on Corning 0215 glass with hot plate temperature settings superimposed.

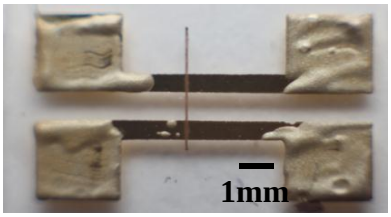

Figure 30 - Photograph of "H" test structure with 80µm wide inkjet printed gold bridge.

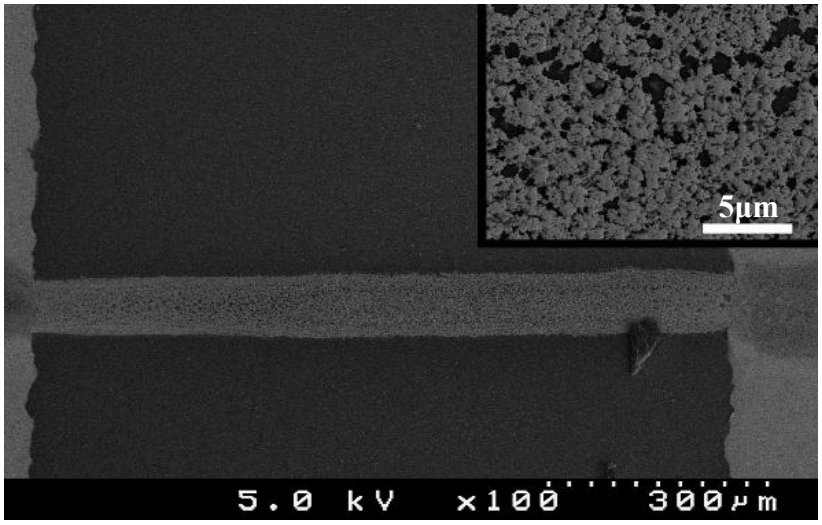

Figure 31 - Scanning electron micrographs of 750nm thick printed Au bridge on soda lime glass sintered at 175°C for 24 hours. Inset shows enhanced view film structure.

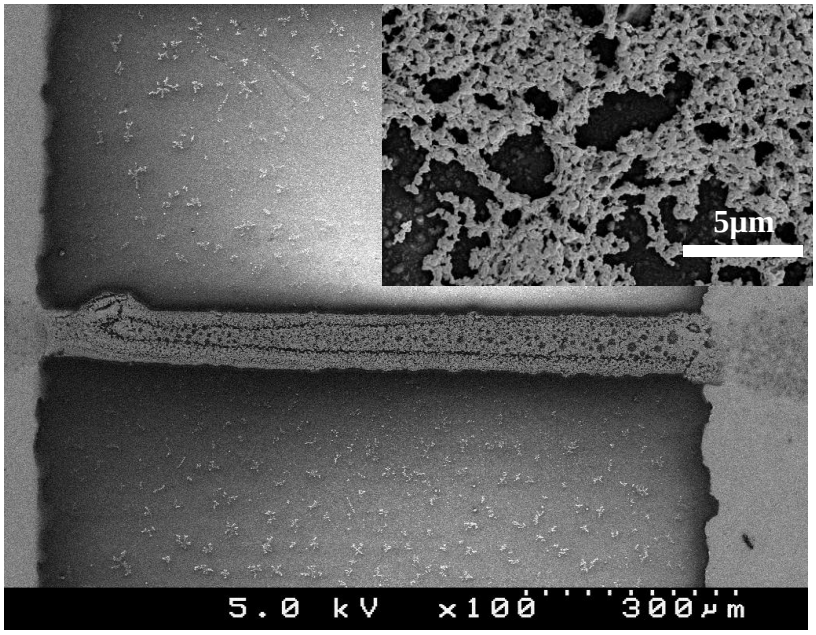

Figure 32 - Scanning electron micrographs of 750nm thick printed Au bridge on soda lime glass sintered at 225°C for 24 hours. Inset shows enhanced view of film structure.

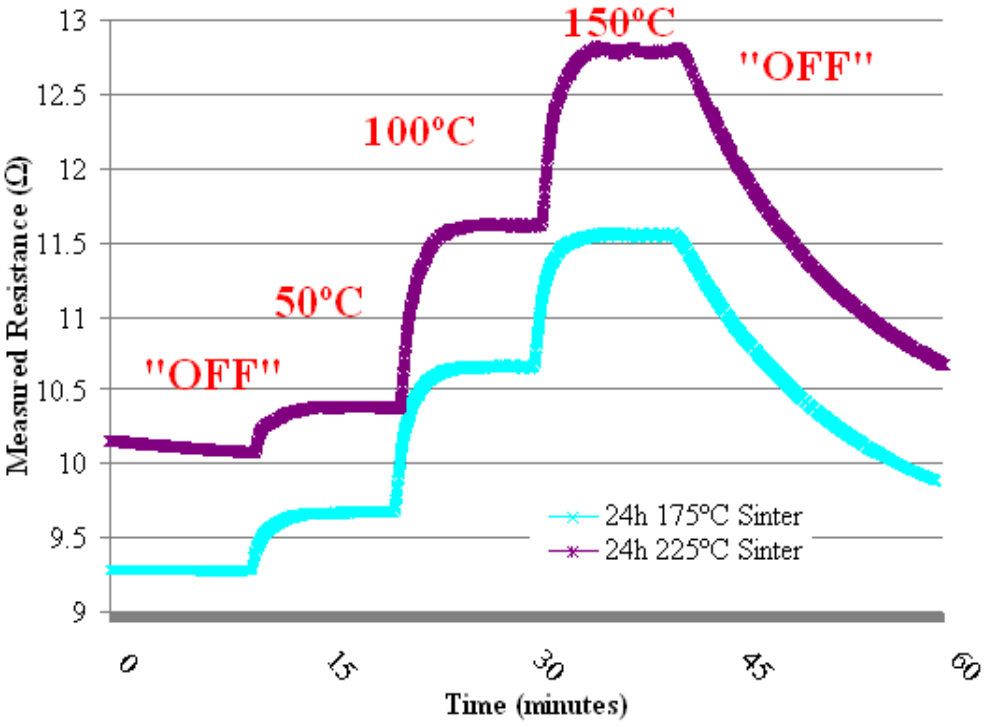

Figure 33 - Measured 4-point resistance of two different Au films ramped to three temperatures and held for 10 minutes. Hotplate settings are shown in red.

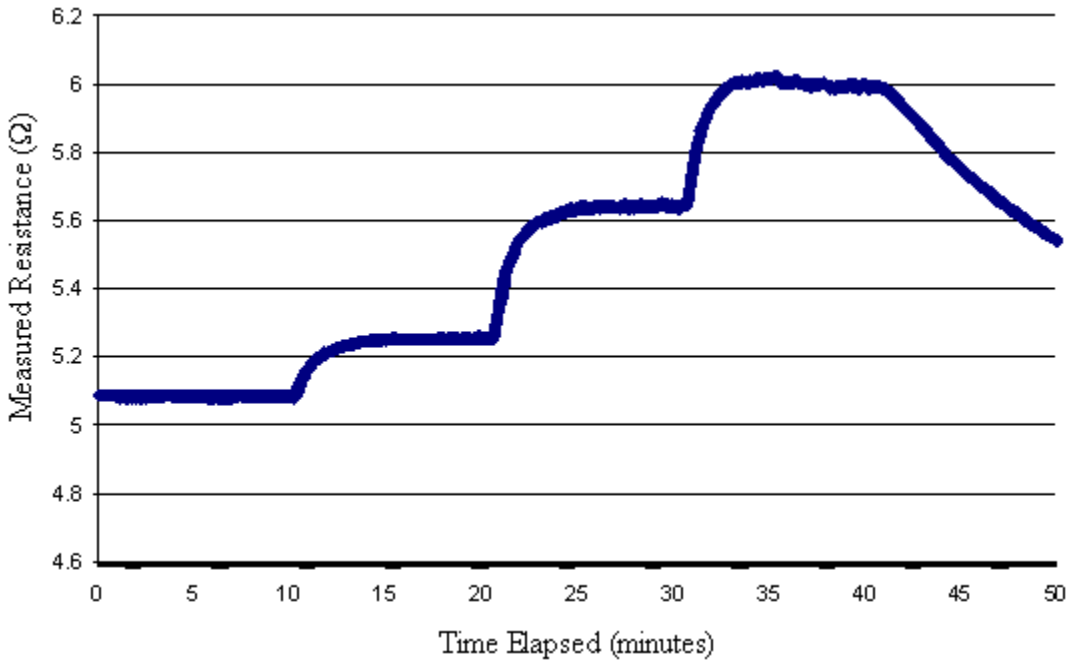

Figure 34 - Thermoresistive response of Au-NP film on aerosol deposited high-temperature enamel (24h 200°C sinter step) heated to 50, 100, and 150°C.

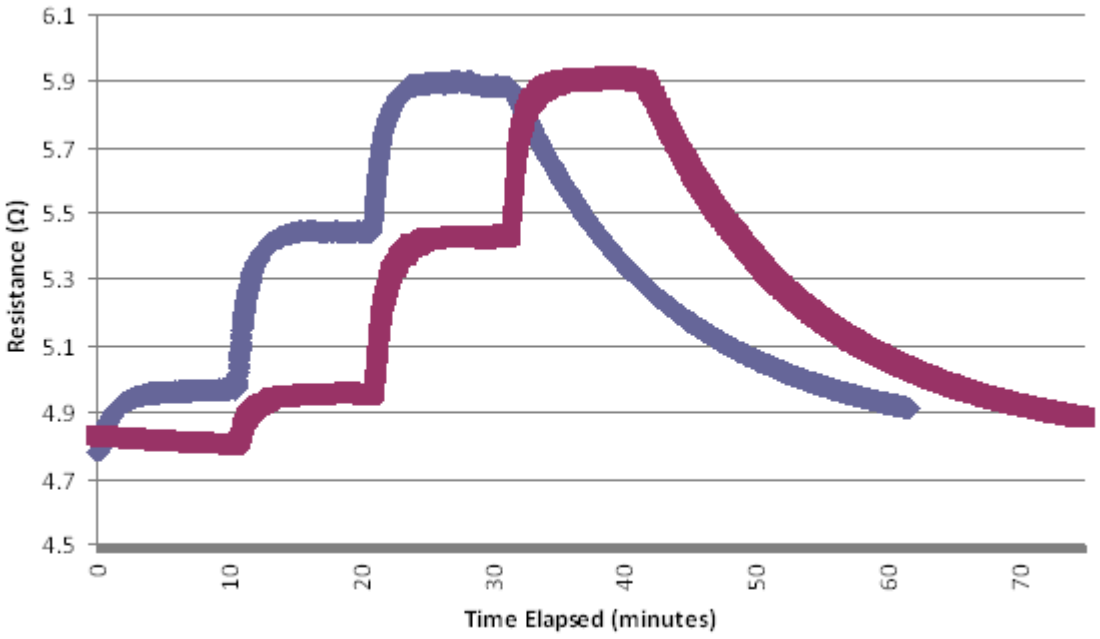

Figure 35 - Two consecutive measurement cycles demonstrating stability of printed Au thermoresistive response heated to 50, 100, and 150°C (1st cycle is blue).

The measurements demonstrate excellent thermoresistive response which is both stable and repeatable over the temperature range investigated. To quantify these responses, a 5 minute average was taken of the data during of each tier at 50, 100, and 150°C, respectively. The average resistances of the two Corning 0215 samples and the high-temperature enamel sample under varied annealing conditions are plotted in Figure 36. A linear fit was applied to each sample, and the results reveal excellent linearity of the thermoresistive response.

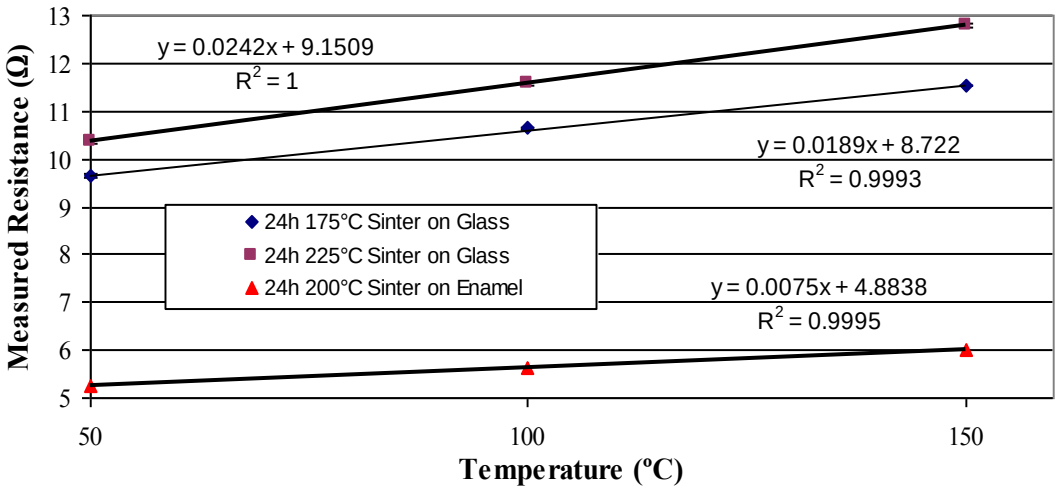

Figure 36 - Plot of measured resistance averaged over a 5 minute period versus the corresponding temperature. A fit of this data indicates a linear resistance change over this temperature range.

The temperature coefficient of resistance (TCR) α of a material is a measure of the normalized resistance change over a given temperature change. Given an initial resistance R_0 (Ω), and a change in resistance ΔR (Ω), for a change in temperature ΔT (°C or K), the TCR is computed as:

$$\frac{\Delta R}{R_0} = \alpha \Delta T$$

which is often displayed in units of ppm/°C. Using this relation the TCR of the resistive bridges are calculated and listed in Table 8.

Table 8 - Computed TCR of Sintered Au-NP Bridges

Substrate	Sintering Temperature (°C) for 24 hours in air	TCR (ppm/°C ±10%)
Corning 0215 Glass	175	2000
Corning 0215 Glass	225	2300
High-Temperature Enamel	200	1400

These TCR measurements are similar to those of sputtered low resistance gold film resistors, which have been reported with a TCR of 2500 ppm/°C ±10% [10]. Discontinuous gold thin films have also been reported with a TCR of 1400 ppm/°C [11].

6.4 – Summary

In this chapter, an "H" shaped test structure enabling simple the 4-point resistance measurements of inkjet deposited bridges has been developed and presented. An automated data acquisition setup to complement the test structure was realized using spring loaded pins for simple operation.

Gold bridges were patterned by inkjet print onto bare Corning 0215 soda lime glass and high-temperature enamel using from a hexanethiol-encapsulated gold nanoparticles (15%wt) ink, and sintered in air for 24 hours at temperatures ranging from 175-225°C. The resistance of these bridges was then measured using the 4 point technique at 50, 100, and 150°C. The thermoresistive response of all samples exhibits high stability, repeatability, and linearity over the measured temperature range. The temperature

coefficient of resistance was computed for the inkjet printed gold films with values similar to those of low resistance gold thin films found in the literature. While, the printed microstructures exhibit a TCR less than that of bulk gold (3400 ppm/°C) [12], their deposition technique still makes them attractive for temperature sensing applications. Gold films are normally either deposited vacuum by evaporation or sputtering, or through electro/electroless plating by immersion in a wet chemical bath. Patterned gold film deposited by inkjet printing using an organically encapsulated gold enables the application of temperature sensitive gold films for substrates whose size or composition is incompatible using conventional gold deposition techniques.

7. Passive RF Components

Conventional microelectromechanical systems have found numerous applications for radio frequency (RF) electronics. MEMS devices offer the potential for high performance, filters, phase shifters, low-loss switches, and as tunable reactive components [1]. MEMS devices for frequency control and timing have seen extensive development and commercialization efforts [2]. Currently, there is considerable interest for low-cost printed RF identification (RFID) tags [3, 4, 5]. Planar single-layer printed RF antennas and filters have been realized on paper substrates using silver [6]. These RF devices have been designed using thin conducting layers of metal with thicknesses typically below 1 micron without consideration of their mechanical properties [7]. Just as conventional electronics drove a strong demand for conventional RF MEMS devices, the field of printed electronics will certainly benefit from printed RF MEMS structures so development in this area is needed.

Accordingly, this chapter develops a new multilayer manufacturing process for the microfabrication of RF devices and microelectromechanical systems. A hybrid approach using both inkjet printing and shadow-masked aerosol deposition is demonstrated by building passive RF components. Inkjet printed Au-NPs are used to pattern structural layers with fine features. Dielectric passivation layers often do not require fine features, so a low-cost laser-cut polymer shadow mask is used to pattern a high-temperature dielectric enamel layer. Inkjet printing and shadow-masking are used in successive order to demonstrate this process through the development of a planar resistor and a parallel inductor/capacitor tank circuit.

7.1 – Hybrid Inkjet and Aerosol Fabrication Process

The devices presented in this chapter were microfabricated using the same process conditions in order to demonstrate the robustness of the process parameters selected. The high-temperature enamel introduced in Chapter 4 was selected as the base substrate such that this manufacturing process can be transferred to other base materials with minimum process adjustment. Substrates were prepared by first cleaning soda lime glass slides (Corning 0215) in acetone and ethanol and drying them with clean dry air. The enamel was then spray deposited onto the substrate until a smooth finish was observed (see Chapter 4) and air dried for 30 minutes at room temperature. The substrates were subsequently transferred to a hotplate and cured at 200ºC for 60 minutes yielding a thickness of 25±10µm.

Hexanethiol-encapsulated gold nanoparticles were synthesized and suspended in α-terpineol (15%wt) forming the ink which was subsequently loaded into an inkjet head with a 30µm diameter piezoelectric nozzle. The print-head was driven with a 20Hz bipolar waveform using 2/5/2/5/2µs timing parameters at ±30V. Each gold layer in the processed is patterned through two successive passes onto a 140°C platen yielding a film thickness of 1.9µm and a line width of 80±10µm. The velocity of the printer was set to overlap adjacent droplets by 50%. After deposition the bottom gold structures were held at 140°C for 30 minutes to fully drive off solvent and then ramped to 200°C and held for 60 minutes in air to sinter the Au-NPs into a gold film.

The shadow mask using for patterned dielectric layers was laser cut from a 125µm thick sheet of polyester film (3M CG3700) cut using a 50W CO_2 laser cutter (Versalaser,

Inc). The mask was aligned under by microscope and held in place with polyimide tape. Enamel was deposited onto the shadow mask using a 1 second burst at a distance of 300mm. After a 5 minute air dry, the shadow mask was removed, and the device baked for 1 hour at 200°C. Removal after 5 minutes allows the enamel to reflow, forming round dielectric edge suitable for printing.

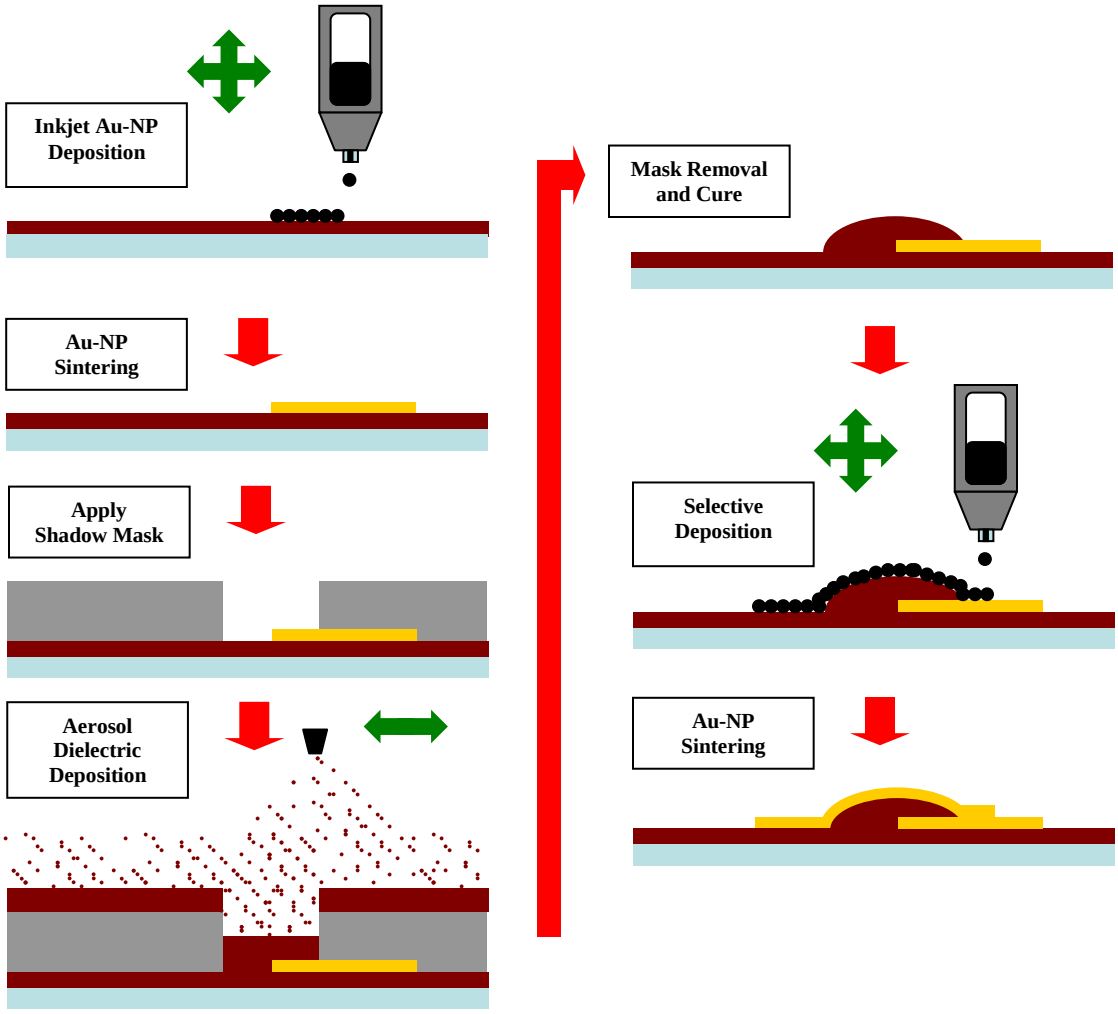

Figure 37 - Hybrid Inkjet and Shadow-Mask Deposition Process

Figure 37 illustrates the cross section of the hybrid microfabrication process for devices with two structural gold layers, and one patterned dielectric layer. First a suitable substrate material is prepared and the bottom device layer is patterned by inkjet printing

using Au-NP ink. The wafer is subsequently thermally processed to sinter the Au-NPs into a coherent conductive film. Next, a polyester shadow mask is aligned to the substrate and high-temperature enamel is aerosol deposited the substrate. The shadow mask is removed and the enamel cured, yielding a smooth insulating layer. Inkjet deposition and sintering is subsequently repeated to yield the final device. This process can be scaled to additional device layers and materials as necessary.

7.2 – Spiral Planar Inductor

A 4-turn planar spiral inductor was selected at the first device to test hybrid microfabrication using a high-temperature dielectric enamel and inkjet printed gold nanoparticle ink due to their widespread use in RF integrated circuits [8]. The relevant design parameters for this device are shown in Table 9 and a predicted inductance of 23.8nH was computed using the Modified Wheeler approximation [9].

Table 9 – Spiral Inductor Design Parameters

Design Parameter	Value
Number of Turns	4
Conductor Width	75µm
Outer Diameter	1.6mm
Center-Center Turn Spacing	150µm

500µm by 500µm pads were patterned at the end of each inductor trace to allow probing and measurement. Figure 38 is an optical micrograph test pattern of both printed gold device layers to verify fabricated dimensions and inter-layer alignment on the printer prior to full device manufacturing.

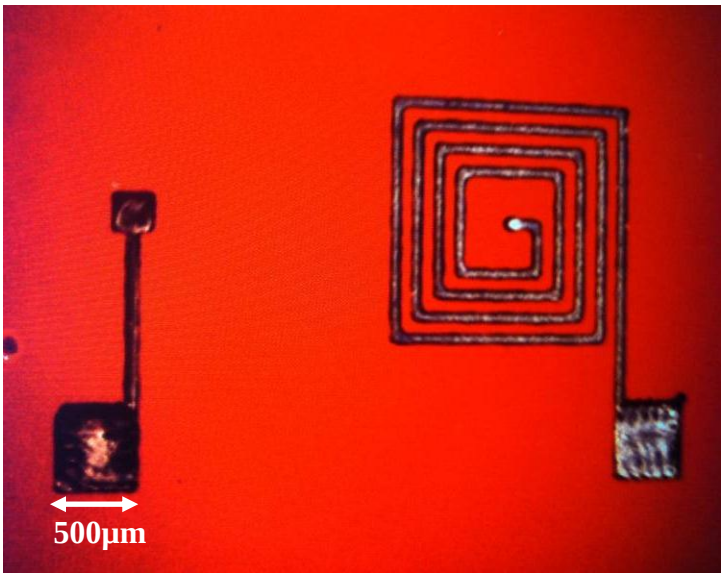

Figure 38 - Optical micrograph of two inductor structural layers printed separately to verify dimensions and alignment.

The bottom device layer was first patterned and sintered using the parameters outlined in the previous section of this chapter. A 400 by 750µm rectangular shadow mask was then aligned to the substrate and a layer of enamel deposited onto the device. After aerosol deposition (2 second burst) the shadow mask was removed and cured resulting in a patterned dielectric as shown in Figure 39. Stylus profilometry (KLA Tencor P-2) found the dielectric reaches a maximum thickness 18µm of and that the final dimensions of the dielectric layer spread by approximately 150µm in all lateral dimensions.

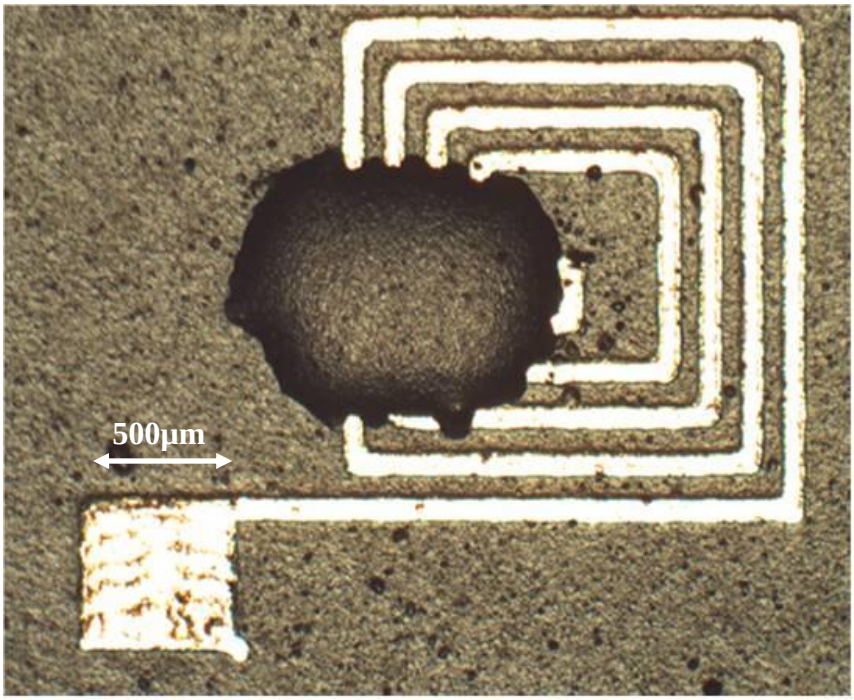

Figure 39 - Planar inductor after application of dielectric bridge.

Next, the device was aligned on the printer and the top device layer was patterned and sintered to yield an electrically conductive device. The center pad of the top trace is 200µm by 200µm to allow for misalignment between device layers as the substrate is removed from the printer for dielectric deposition. An optical micrograph of one realized inductor is shown in Figure 40. Stylus profilometry was subsequently used to characterize the device. Figure 41 shows a cross section of the device as measured approximately by vertically bisecting Figure 40. The four 1.9µm thick gold lines on each side of the bottom layer are clearly visible and appear uniform. The thick concave dielectric layer dominates the center of the cross section, with the top gold trace visible at the top of the image and measures 1µm thick.

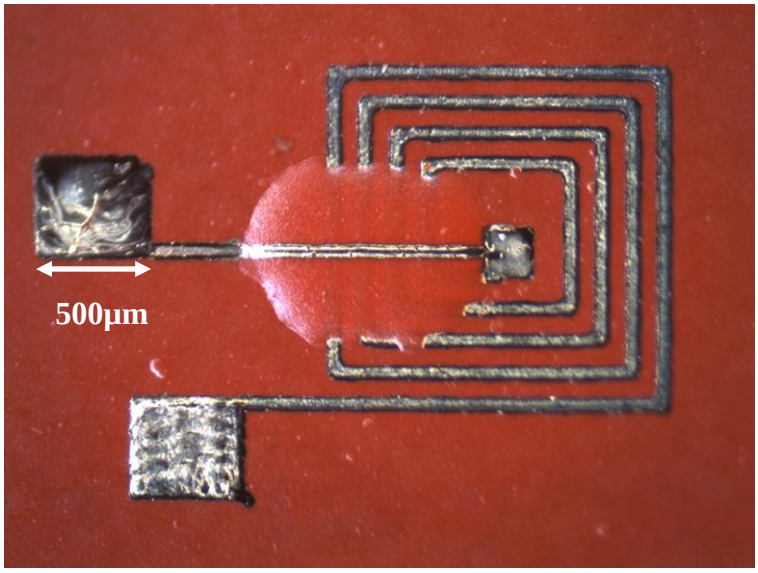

Figure 40 - Gold planar inductor realized in this work. Line width is 75µm and thickness is 1.9µm. The line spacing is 75µm and outer coil diameter is 1.67mm. The enamel dielectric was patterned via shadow mask and reaches a center height of 18µm.

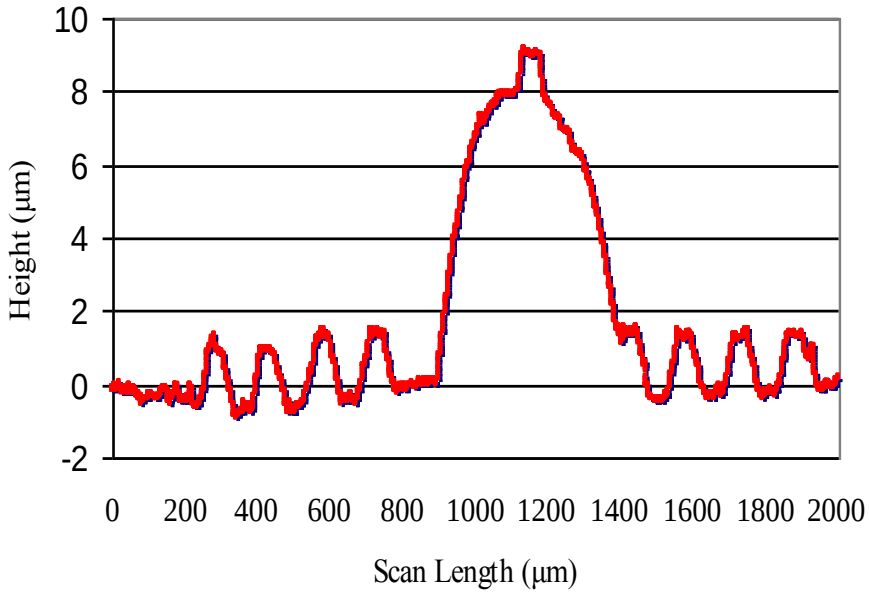

Figure 41 - Stylus profilometer (KLA-Tencor P2) scan of printed inductor taken vertically across the center of Figure 40. The eight coil wires and enamel dielectric are clearly visible. The upper trace is apparent at the top of the image. The dielectric reaches a maximum thickness of 18µm (not shown).

After physical dimensioning and imaging, the device was characterized electrically using an Agilent E4980A LCR meter. At 1MHz device was measured to have a series inductance (Ls) of 24.0±0.1nH and a series resistance (R_s) of 63.3±0.1Ω. The DC resistance (R_{dc}) of the coil was R_{dc}=65.5±0.1Ω. Due to the large inter-conductor spacing of the coil and the thick dielectric layer, the self-capacitance of the coil was expected to be quite small giving the inductor a self-resonance at a frequency higher than available measurement capabilities [10]. An integrated capacitor was then selected for addition in parallel to further test this deposition technology towards more complex printed gold microelectromechanical systems.

7.3 – Parallel L-C Tank

The spiral inductor was then extended to include a discrete printed capacitor integrated in parallel to form an LC tank in an effort to build a structure similar to RF MEMS components. This configuration differs from RFID L-C tanks which consist of a capacitor surrounded by an inductor to minimize die size [3]. The separate parallel component layout was selected for several reasons including that a discrete capacitor and inductor design enables the dimensions of either passive component to be resized without affecting the complementary component, enabling flexibility in customizing resonant frequency for timing applications. Additionally, a discrete capacitor design gives ample real estate for the addition of anchors and control lines towards the goal of building an air-gap tunable capacitor with an integrated inductor. In this section we present printed gold parallel LC tank deposited on enamel and using enamel as the parallel plate capacitor dielectric material.

The characterization of the discrete inductor found a sizable coil resistance which must be accounted for during modeling of the LC resonator. A schematic diagram of the equivalent circuit model of the device realized herein is shown in Figure 42. Table 10 lists the relevant governing equations as derived from [11]. The resistance will affect both the resonant frequency and the quality factor (Q) of the device.

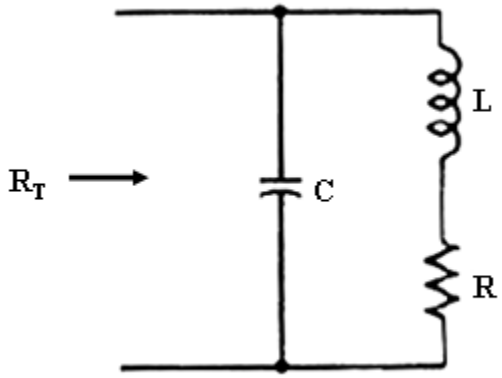

Figure 42 – Equivalent circuit model of RL//C circuit.

Table 10 - RL//C Resonant Circuit Design Formula (from [11])

Quantity	Expression	Units
ω_0	$=\left(\frac{1}{LC}-\frac{R^2}{L^2}\right)^{\frac{1}{2}}$	rad/s
Q	$=\frac{\omega_0 L}{R}=\omega_0 C R_T$	
$\omega_0 L$	$=\frac{1}{\omega_0 C}\left(\frac{Q^2}{Q^2+1}\right)$	Ohms
R_T	$=\frac{L}{CR}=\frac{Q}{\omega_0 C}=R\left(Q^2+1\right)$	Ohms

The design consists of a four turn inductor with identical dimensions as those shown in the previous section. The leads connecting to the 500µm by 500µm pads were extended and a 750µm by 750µm square parallel plate capacitor was fashioned adjacent to the

spiral inductor. The dielectric layer was patterned with a 1250µm by 1250µm square pad for the capacitor dielectric region and a 200µm wide trace to the center of the inductor. The dielectric was oversized to ease alignment requirements and minimize edge effects on the capacitor due to reflow. The devices were subsequently manufactured using the process outlined previously in this chapter. Optical micrographs of six realized devices are shown in Figure 44. The top center device is further detailed in Figure 45. The capacitor was measured to have dimensions of 840µm by 840µm. Stylus profilometry was used to measure the topology of the parallel plate capacitor; the thickness of the dielectric measured 6µm on one size and 8µm on the other, with a peak thickness of 12µm as shown in Figure 43.

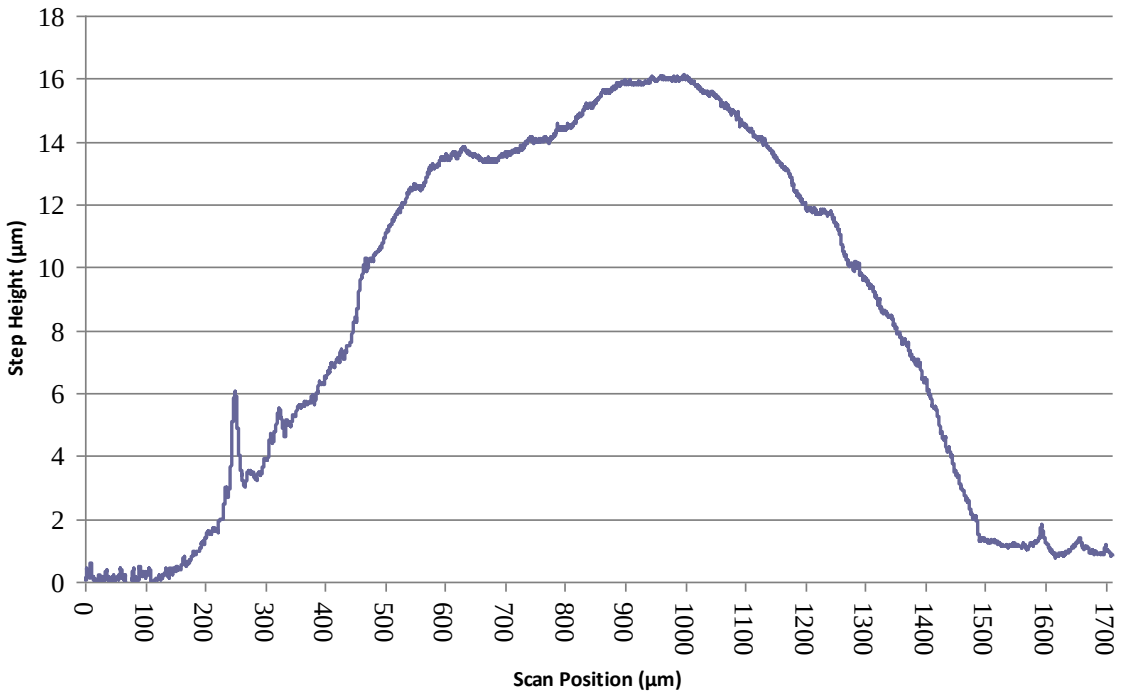

Figure 43 - Stylus profile of parallel plate capacitor (Figure 45) demonstrating thickness variation of spray deposited dielectric. Top electrode spans from 450µm to 1300µm.

The device was estimated to have a resonant frequency of 615MHz assuming an average dielectric thickness of 10μm, a dielectric constant of 3.0, and using the inductor values found in the previous section. Devices were then characterized using an Agilent 8720ES S-parameter analyzer on a Karl Suss PM-5 probe station. The test setup was first calibrated and the configured to measure the S12 parameters of the resonators. A parallel LC tank has a theoretical infinite impedance at resonance, and Figure 46 shows the frequency response of one LC Tank at resonance. The device operates at a resonant frequency of 596MHz, very close to the expected value. The quality factor of the resonator was computed by measuring the -3dB bandwidth and computed to be 60. The resistance at resonance was computed as 210kΩ.

Of the six devices fabricated during this run, three of them were electrically functional. Two devices suffered failures due to inconsistency of the dielectric deposition which can be solved through improved deposition equipment and masking techniques. The third device failed due to a break in the trace connecting the top gold trace to the bottom gold layer.

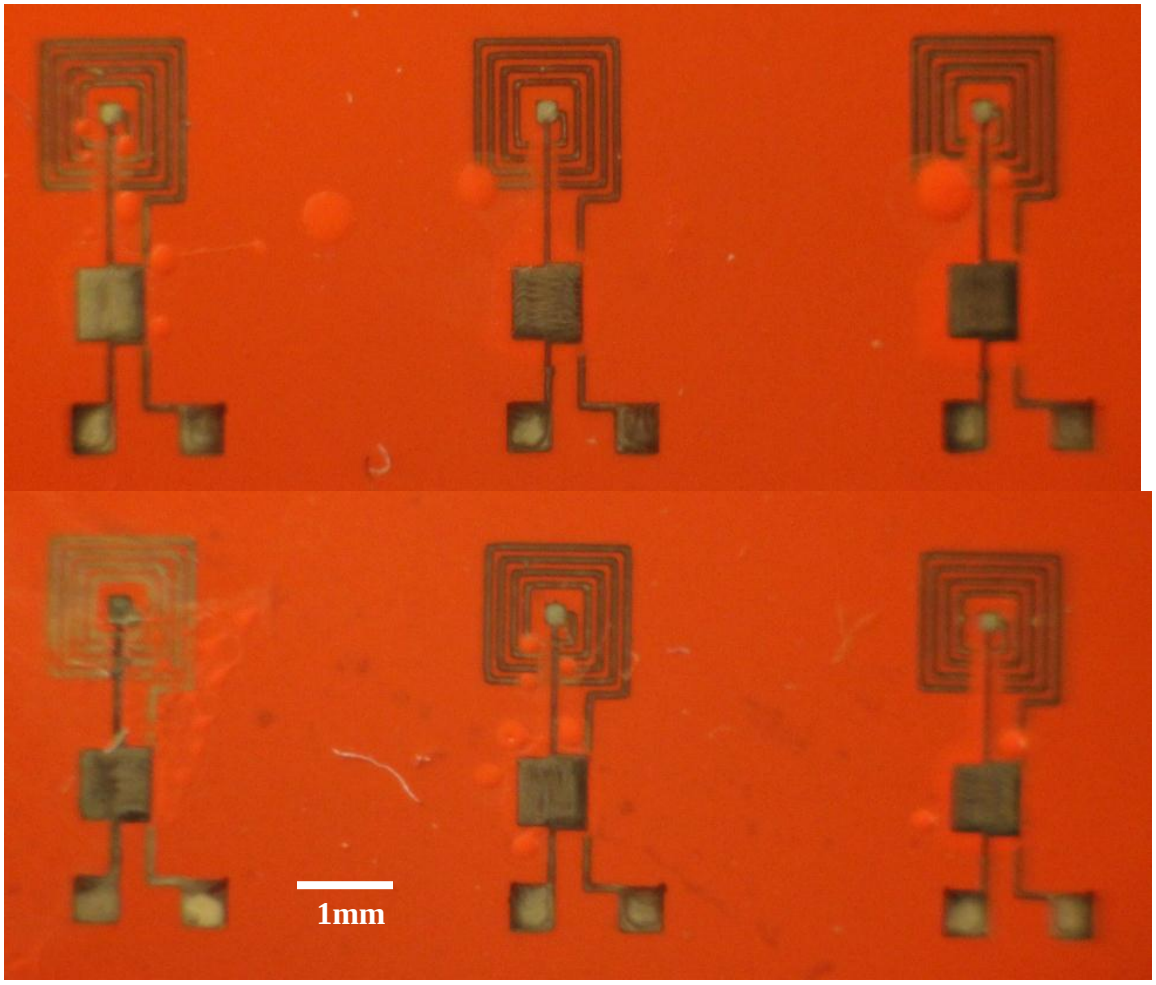

Figure 44 - Parallel LC Tanks realized in this work. Droplets are liquid enamel deposited onto substrate during shadow mask removal.

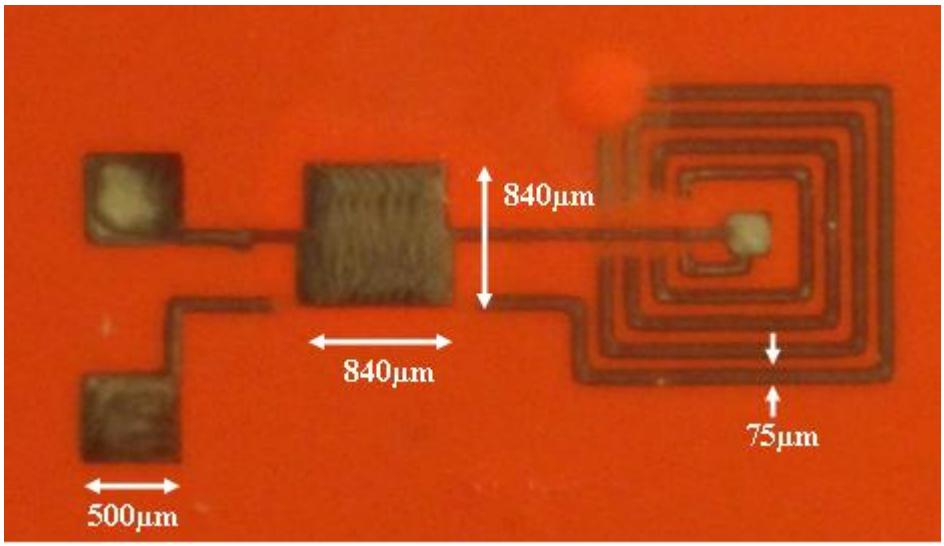

Figure 45 - Optical micrograph of parallel LC resonator.

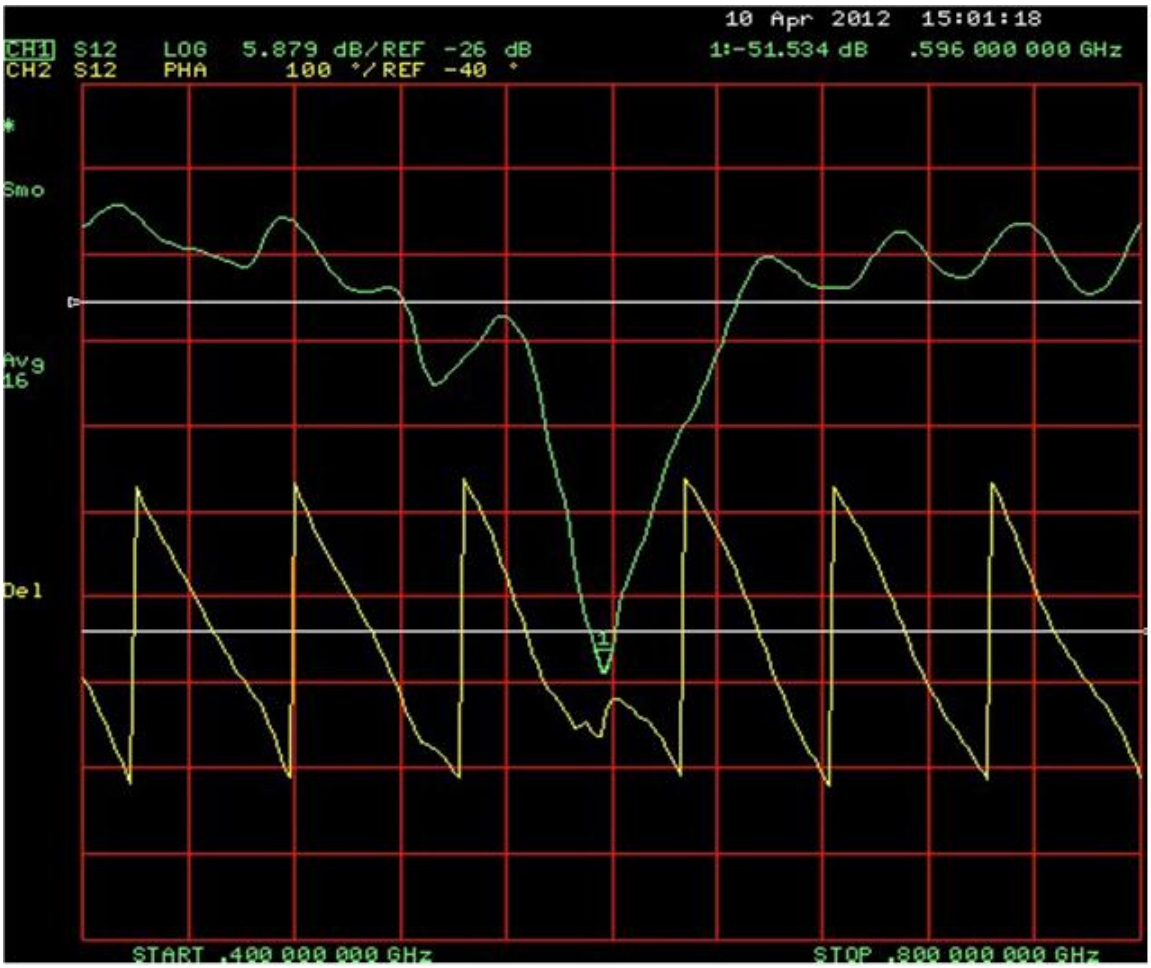

Figure 46 - S12 measurement of LC Tank showing magnitude (top) and phase (bottom) for -20dB drive input power. Q of 60 at 596MHz

7.4 – Summary

This chapter has introduced a novel microfabricated process using an aerosol deposited substrate and dielectric layer. Dielectric layers were patterned using a simple shadow-masking process. All conducting gold layers were deposited via inkjet printing from a hexanethiol-encapsulated gold nanoparticle ink and subsequently sintered. Using this process an inkjet printed gold inductor was realized using the high-temperature enamel as both the base substrate and the dielectric bridge was demonstrated and performed as predicted with a measured inductance of 24.0±0.1nH at 1MHz. This process was then further extended to realize the first inkjet printed gold parallel LC tank using discrete a discrete inductor and capacitor with an aerosol deposited dielectric. The device was characterized using an S-parameter analyzer and found to have a resonant frequency of 596MHz and a Q of 60.

These devices demonstrate the feasibility of these manufacturing techniques towards the realization of more complex printed gold microelectromechanical systems. The aerosol high-temperature enamel has shown utility as pattern-able dielectric material for printing multilevel gold layers. Further improvement of the aerosol deposition technique or developing the enamel as a jettable material will further improve the capabilities of the material and this prototype printed MEMS manufacturing process.

8. Conclusions & Future Work

8.1 - Conclusions

This dissertation has explored the properties and process techniques of sintered gold films deposited via inkjet printing towards the microfabrication of gold microelectromechanical systems. A precursor ink consisting of hexanethiol-encapsulated gold nanoparticles (Au-NP) suspended in α-terpineol has been identified from the printed electronics literature as a promising printed gold MEMS structural material. This ink was successfully synthesized along with a custom inkjet deposition system to enable the exploration of this ink for the development of printed gold microsystems. Using the inkjet printer, a set of deposition parameters was identified which yields a smooth, continuous as-deposited film.

A novel low-cost aerosol dielectric material has been identified and characterized. This enamel has shown utility as both a patternable dielectric, as well as a substrate base layer to isolate printed microstructures from the underlying bulk substrate material. The aerosol based nature of this material lends itself well for surface treatment of a multitude of substrate materials and topologies, rendering them suitable for subsequent inkjet patterning of microstructures. The use of a conformal surface treatment minimizes the effect of the bulk substrate, and should allow for process parameters to be tuned for the dielectric material independent of the underlying bulk substrate.

The sintering process of hexanethiol-encapsulated gold nanoparticles was explored through measurement of the resistance of sintered Au-NP films for multiple thicknesses, temperatures, and substrates, revealing changes in the resistance evolution as a function of all of these parameters. These measurements were compared to nanoindentation of

printed gold films sintered for differing durations, and revealed, for the first time, that the effective stiffness of the material continues to change for time periods beyond initial sintering onset. An extended sintering step is therefore required to ensure the sintered film properties stabilize for electromechanical applications. This differs from the current state of the art which stops Au-NP sintering upon observing a film color change or an initial drop in gold nanoparticle film resistance.

Scanning electron microscopy images reveal sintered Au-NPs on Corning 0215 can exhibit highly porous structures. While not suitable as a structural material for MEMS, these films were measured to have an enhanced temperature coefficient of resistance over densified Au-NP films, making them a promising material for inkjet deposited temperature sensors. This represents the first measurement of the temperature coefficient of resistance of gold films realized from sintered Au nanoparticles.

The TCR measurements were performed through the development of a robust 4-point methodology utilizing an “H” test structure and spring-loaded contact pins. This experimental configuration greatly simplifies printed sample preparation, as the “H” test structure accounts for alignment issues. The use of spring-loaded pin interface allows for excellent signal integrity during thermal cycling of the devices under test. This technique provides a robust solution for future studies on the electrical properties of inkjet printed materials.

Suitable process conditions were developed for printed microsystems for both the printed conductive gold films and the aerosol-based dielectric. These materials were then combined into a hybrid additive microfabrication process using inkjet printed gold structural layers and shadow-mask patterned aerosol deposited dielectric enamel for the

realization of multilayer devices. Using this technique, gold features with a minimum dimension of 75µm wide and 1.9µm thick were achieved. The utility of this fabrication process was then demonstrated through the realization of multilayer passive RF components. A planar spiral inductor has been realized using inkjet printing using aerosol based enamel as both the substrate and as the bridging dielectric. The 4 turn inductor measured 24.0±0.1nH at 1 MHz and the DC resistance of the coil was 65.5±0.1Ω.

Using the hybrid microfabrication process, the first instance of a discrete parallel LC tank circuit has been realized. This topology differs from the concentric designs employed in RF-ID research in that the inductor is not coaxial to the capacitor. The discrete nature of the LC tank is designed for the future addition of anchor springs and control lines for the realization of a tunable LC tank circuit. A resonant frequency of 596MHz with a Q of 60 was measured from a fabricated device. This performance compares favorably to other printed resonators in the literature including the 150MHz silver nanoparticle on polyimide printed coil (Q=20) [1]. Similarly, printed gold 13.56MHz RFID tags have been reported a best as-printed Q of ~5, with a maximum Q of 30-100 with the addition of gold electroplating steps to reduce printed film resistivity [2]. In comparison, the device realized using the process techniques developed in this work represents the highest Q of an *as-printed* LC resonator using sintered inkjet printed gold nanoparticles

8.2 – Future Work

The field of printed microelectromechanical systems is just emerging as a potential advanced additive manufacturing technique. Opportunities are widespread for the development of new process techniques and jettable materials. Further, there is a need

to characterize the electrical and mechanical properties of inkjet deposited materials to enable modeling and device design. This work has developed sintered gold films patterned from hexanethiol-encapsulated Au-NPs towards printed MEMS, but further effort is required to build freestanding and complex structures.

For the sintered hexanethiol Au-NP films, further investigations are necessary to extract the mechanical properties of the films for use in device design and modeling. Ideally, freestanding structures should be used for this effort, where possible, to gain an understanding of the mechanical properties, such as the Young's modulus, Poisson's ratio, film stress, and density, for microelectromechanical systems.

Further refinement in the spray deposition techniques should be investigated in an effort to yield films with uniform thickness. Inkjet deposition of the dielectric material should also be investigated to enable the deposition of dielectric material without the need for shadow masks and for the patterning of fine feature. Further study aerosol deposited dielectric enamel on other base substrate materials should also be performed to assess whether the material can fully isolate the effects of the bulk substrate from the inkjet printed layers. A surface coating which accomplishes this goal will enable "substrate invariant" printed microfabrication, removing the need to tune deposition parameters for each type of substrate and greatly enhancing the utility of this microfabrication modality.

Microelectromechanical systems typically involve a released element for sensing and/or actuation, so a sacrificial material compatible with the solvents and temperatures required for processing of the gold and dielectric layers should be identified and studied.

Poly(methyl methacrylate) is one candidate sacrificial material with promising attributes to complement the structural and dielectric materials developed herein.

Finally, additional sintering techniques should be explored to enable the deposition of gold MEMS structures on substrates where bulk heating is undesirable. Ultraviolet and laser sintering are two candidate techniques which should be explored further. The use of an integrated laser for sintering can additionally improve the resolution of inkjet printed films as only desired portions of the inkjet deposited material can be sintered, and the excess ink can be removed in solvent. Further, with proper laser selection, the as-deposited and processed films can be trimmed in situ, allowing for improved film sidewalls and fine features.

Appendix A – Temperature Compensated Differential-Mode Hydrogen Sensor

This device was fabricated by the author using conventional microfabrication techniques and is an example of a MEMS device which can be manufactured using inkjet printing.

A.1 – Abstract

This appendix presents the first instance of a microfabricated differential-mode capacitive gas sensor utilizing temperature compensation. Typical capacitive cantilever sensors offer promise of both high sensitivity and large measurement range. Unfortunately, functionalized cantilevers form a bimorph system, resulting in temperature variations due to the stress gradient induced by the sensor material mismatch. Taking advantage of the reference cantilever commonly employed in differential-mode capacitive sensing, the design presented herein functionalizes the reference cantilever to match the thermal stresses of the sense cantilever, making the temperature dependence common-mode to remove it from the measurement. A surface micromachined polysilicon hydrogen sensor using 50nm of palladium on the sense cantilever, and 40nm of silver on the reference cantilever demonstrates the concept and reduces the temperature induced capacitance error to 4.9fF/ºC compared to 16.6fF/ºC for a bare reference.

A.2 – Introduction

The detection and measurement of gaseous chemicals is a burgeoning field on which the sensing field has focused a great deal of interest. A wide variety of sensing techniques

have been explored including semiconducting, optical, and resistive [1]. Commonly, these gas sensors utilize a functional material whose properties change in the presence of a particular chemical species. A gas sensor should ideally be chemically selective, highly sensitive, offer a large concentration detection range, and be immune to environmental variations such as temperature. While the selectivity is a property of the functional material used for measurement, the remaining parameters are typically dependent on the sensor configuration.

One popular and well-established microelectromechanical systems (MEMS) based sensing modality measures the deflection of a functionalized cantilever beam, allowing high sensitivity and large measurement range [2]. These deflections can be measured as a change in capacitance, enabling measurements changes. Unfortunately, this configuration forms a bimorph system, resulting in temperature dependence induced by the mismatch of the thermal expansion coefficients of the sensor materials. This temperature variation is typically accounted for by either thermal regulation, or data post-processing to correct for the error [3, 4].

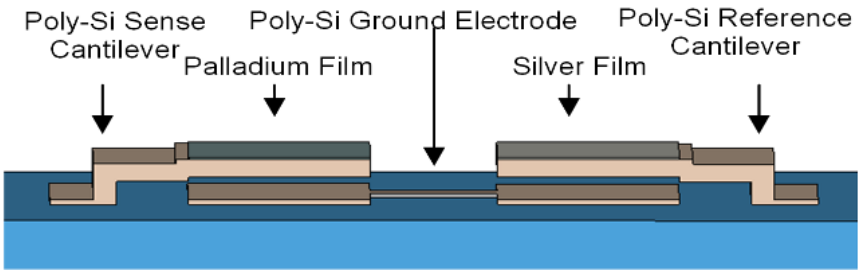

Figure 47 - Perspective view illustration of the fundamental components of the differential mode capacitive gas sensor.

Bare reference cantilevers are commonly used in capacitive cantilever sensors to account for process variation, changes in the dielectric constant, and to eliminate parasitic capacitance from the system [4]. When a differential measurement is performed between the sense and reference cantilevers, common-mode values are eliminated. For a cantilever based sensor, the bare reference cantilever does not form a bimorph system and remains stationary, so both the sense signal and temperature variation will be present on the output.

A microfabricated capacitive cantilever based hydrogen sensor has been reported in the literature by Baselt *et al.* which uses a thin film of palladium (Pd) as a functional material [5]. An estimated 10nm/°C deflection error is reported due to the large thermal mismatch between the Pd film and the polysilicon cantilever, which requires correction using a temperature sensor and a calibrated lookup table.

This paper reports on the functionalization of the reference cantilever of a microfabricated capacitive cantilever gas sensor to provide temperature compensation. By balancing the thermal stresses exerted on both the sense and reference structures, the temperature response will become common-mode and can be removed with a differential measurement. The concept is demonstrated by the realization of a microfabricated hydrogen sensor utilizing thin films of Pd as the sense material, and silver (Ag) to functionalize the reference cantilever.

A.3 – Microfabricated Gas Sensor

Design Overview

A perspective illustration of the proposed hydrogen sensor to demonstrate the temperature compensation concept is shown in Figure 47. The device consists of two

pairs of 2µm thick polysilicon cantilever beams sharing a common fixed polysilicon ground electrode with a thickness of 500nm. The cantilevers and ground electrode are separated by a 2µm nominal air gap. Each cantilever consists of six 110µm wide beams connected near the tip similar in design to [5] to form a single 710um wide cantilever. The lengths of the cantilevers are varied from 125 to 250µm, and sensors are fabricated as single pairs and as four pair arrays.

One cantilever is functionalized with a palladium film, as Pd is capable of reversibly absorbing high concentrations of hydrogen which results in a volumetric expansion of the film [6]. This expansion induces a stress on the cantilever beam, resulting in a deflection and capacitance change. The second, reference, cantilever is functionalized with a silver thin film in order to make it temperature sensitive, but inert to hydrogen. The thickness of the Ag is engineered to match the thermal response of the Pd film.

Temperature Compensation

A bimorph or bimetal system has been extensively studied and has been used to form thermal MEMS actuators [7]. The bending of the polysilicon/metal cantilever can be modeled as a bimetal strip, and the bending radius of curvature R (m) has been derived as [8]:

$$\frac{1}{R} = \frac{6(1+m)^2 B}{t\left[3(1+m)^2 + (1+mk)\left(m^2 + 1/mk\right)\right]} \qquad (1)$$

Where $m = t_{metal} / t_{Si}$, $k = E_{metal} / E_{Si}$, $t = t_{metal} + t_{Si}$, (total device thickness). t_{metal}, t_{Si} are the thicknesses of the two layers (m), and E_{metal}, E_{Si} are their respective Young's Moduli

(N/m^2). B is the linear expansion coefficient and relates to the thermal expansion coefficients α_{metal}, α_{Si}, as [3]:

$$B = (\alpha_{metal} - \alpha_{Si})\Delta T \qquad (2)$$

ΔT is the temperature difference (°C) from the nominal temperature where no thermal bending occurs. Substituting (2) into (1) the radius of curvature for a given temperature change depends only on the Young's modulus, linear thermal expansion coefficient, and thickness of the two materials.

If (1) and (2) are populated with the material properties and thicknesses for the sense cantilever, a radius of curvature R_{sense} can be calculated. Equating R_{sense} to (1) and (2) populated with the respective properties of the reference cantilever materials, the thickness of the reference cantilever material can then be calculated. Table 11 displays the relevant material properties for this work.

Furthermore, for a beam of length L (m) at a small angle, the cantilever deflection Δy (m) can be approximated as:

$$\Delta y = L^2 / 2R \qquad (3)$$

This indicates that the deflection of each cantilever is related to the radius of curvature. Since the thickness of the reference material equates these radii, both cantilevers will deflect equally. Using this information, the thickness of Ag is computed to be 40nm, given a 50nm thick Pd film, and a 2μm thick polysilicon cantilever.

Table 11 – Select Material Properties [9]

	Young's Modulus (E)	***Coefficient of Thermal Expansion (α)***
Si	169 GPa[a]	2.9 x 10^{-6}/°C (25°C)
Pd	121 GPa	11.8 x 10^{-6}/°C (25°C)
Ag	83 GPa	18.9 x 10^{-6}/°C (25°C)

[a.] Approximation for polysilicon, all other values from reference.

Hydrogen Sensing

Equations (1) and (3) are useful for relating the hydrogen concentration to cantilever deflection. The absorption of hydrogen has been shown to obey Sievert's law for lower gas concentrations and the linear expansion coefficient B for (1) has been shown to be related to hydrogen partial pressure (pH_2) as [3]:

$$B = \frac{(\Delta V / V_0)}{3K}\sqrt{pH_2} \qquad (4)$$

Where K is Sievert's constant which has been experimentally shown to be 350 Torr^{½} [10]. $\Delta V / V_0$ is determined experimentally and has been shown to have values between 0.01-0.19 [3]. By substituting (4) into (1), and using (3), the gap change of the cantilever beam can be related to the partial hydrogen pressure.

Differential Capacitive Sensing

In the configuration presented, each cantilever can be approximated as a parallel plate capacitor for small deflections. In the presence of hydrogen, only the Pd film will expand, imparting a stress on the beam bending it downwards. This motion will result in an increase in capacitance of only the sense cantilever. Measuring the difference in capacitance between the two cantilevers will also result in a measured increase in capacitance.

When the temperature changes, both the Pd and Ag films will expand/contract equally, resulting in an equal capacitance change for both cantilevers. As the temperature dependence of both cantilevers in now common-mode, these changes will cancel out when measuring the capacitance difference between the two cantilevers.

A.4 – Fabrication

The sensor realized in this work is constructed utilizing standard polysilicon surface micromachining techniques. A diagram of the fabrication cross section is illustrated in Figure 48. First, a 300nm thick stoichiometric Si_3N_4 passivation layer is first deposited on a 100 mm-diameter boron doped <100> silicon wafer. This is followed with 500nm of *in situ* phosphorus doped polysilicon which is subsequently patterned and etched by reactive ion etching (RIE) to form the bottom electrodes. Next, a 2μm low temperature oxide (LTO) sacrificial layer is deposited and anchor holes are opened using buffered oxide etch (BOE). A 2μm thick *in situ* phosphorus doped polysilicon layer is next deposited and patterned by RIE to form the cantilever structures. The wafer is then annealed in N_2 for one hour at 1050°C for dopant activation and film stress relaxation. 250nm of nickel is sputtered and patterned by lift-off to form bond pads on the wafer which is subsequently sintered to create ohmic contacts.

Both of the functionalization metals are next sputtered onto the cantilevers. Before each sputter step a 30s RF pre-clean is performed. First, a 10nm adhesion layer of chromium (Cr) is sputtered onto the wafer followed immediately by 50nm of Pd to functionalize the sense cantilevers. These metals are then patterned by lift-off. Next, 10nm of Cr and 40nm of Ag are sputtered onto the reference cantilevers and patterned by lift-off.

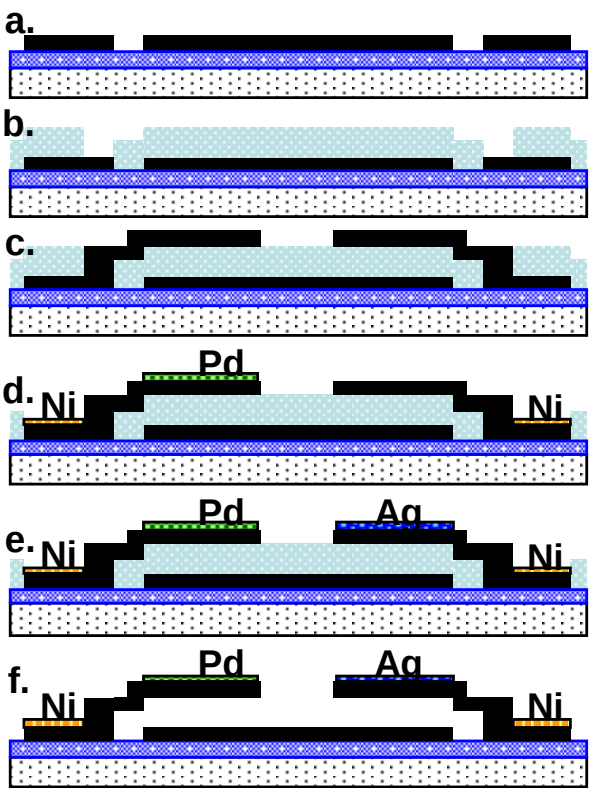

Figure 48 - Fabrication cross-section of the gas sensor. (Polysilicon shown in black, oxide in light blue, and nitride in dark blue.)

The wafer is then diced into 10.2mm by 10.2mm dies each containing 54 cantilever pairs. Release was performed in a two-step process. Each chip is etched in Silox Vapox III (Transene Inc.) for 35 minutes and then dried using supercritical CO_2. The wafers were allowed to sit for several days in dry N_2, and then the etch/dry process was repeated a second time to yield released devices. Failure to allow the devices to sit resulted in polysilicon degradation and metal delamination. Optical micrographs of the fabricated device are shown in Figure 49.

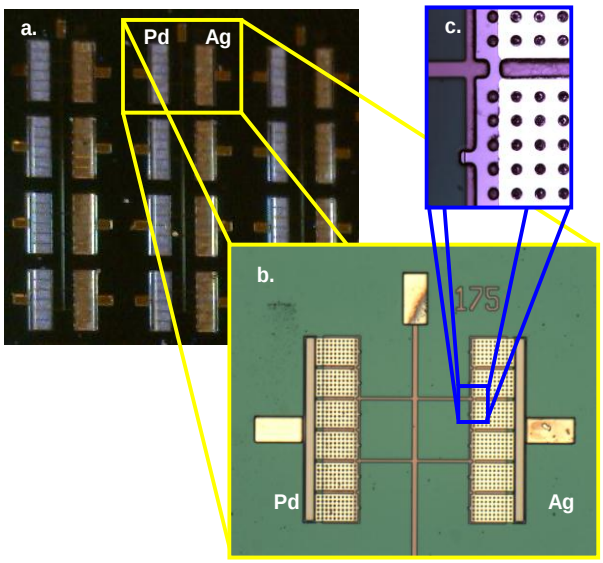

Figure 49 - Optical micrographs of (a) Sensor arrays (b) A single differential pair (c) Beam detail showing metal and polysilicon layers.

A.5 – Results

Capacitance measurements have been performed using the test setup shown in Figure 50. Each die is loaded onto a probe station containing a polyimide heater. Hydrogen is generated by electrolysis of water using graphite electrodes and stored in an inverted 10ml syringe. The syringe is plumbed to the probe station using 1/8 inch rubber tubing with a valve to close the tubing located near the probe station. Capacitance measurements are performed using an Agilent E4980A LCR Meter.

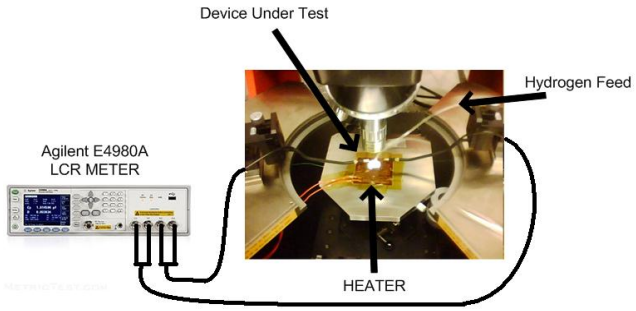

Figure 50 - Test configuration on a Karl Suss PM5 Probe Station. A polyimide heater controls temperature. Hydrogen is generated by electrolysis and supplied as a small impulse burst to test device functionality.

Sensor functionality and hydrogen selectivity of the gas sensor were first verified experimentally. Measurements are taken at 10 kHz and after 10 seconds, the valve is opened exposing the sensor to an impulse of hydrogen. Figure 51 shows the sensor impulse response of a 175µm cantilever pair to hydrogen exposure. The sense cantilever capacitance increases by 75fF, while the reference cantilever output remains constant. This experiment demonstrates the functionality of the hydrogen sensor and verifies that the Ag film on the reference cantilever is insensitive to hydrogen. An improved test configuration is currently being implemented to allow for controlled concentrations of H_2 to more fully characterize the sensing characteristics.

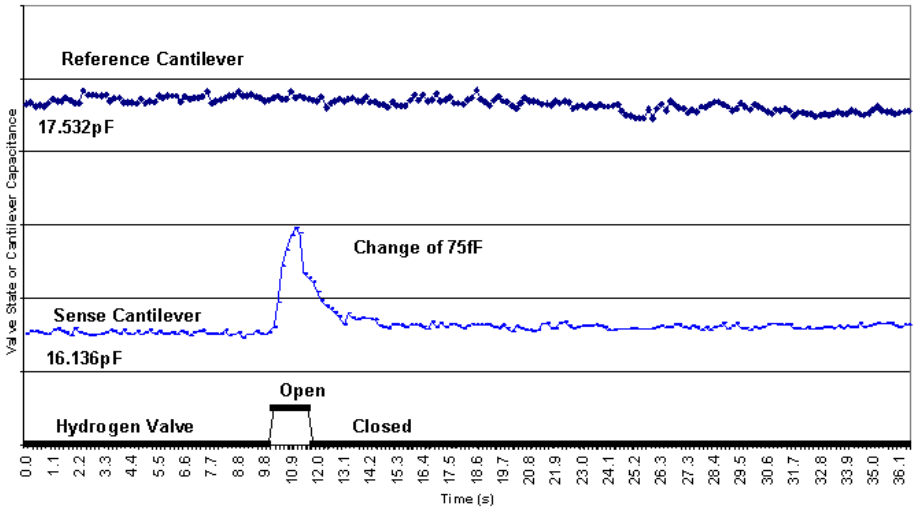

Figure 51 - Plot of 175µm long reference and sense cantilevers showing their response when exposing the sensor to a small burst of hydrogen (Horizontal lines are 50fF apart).

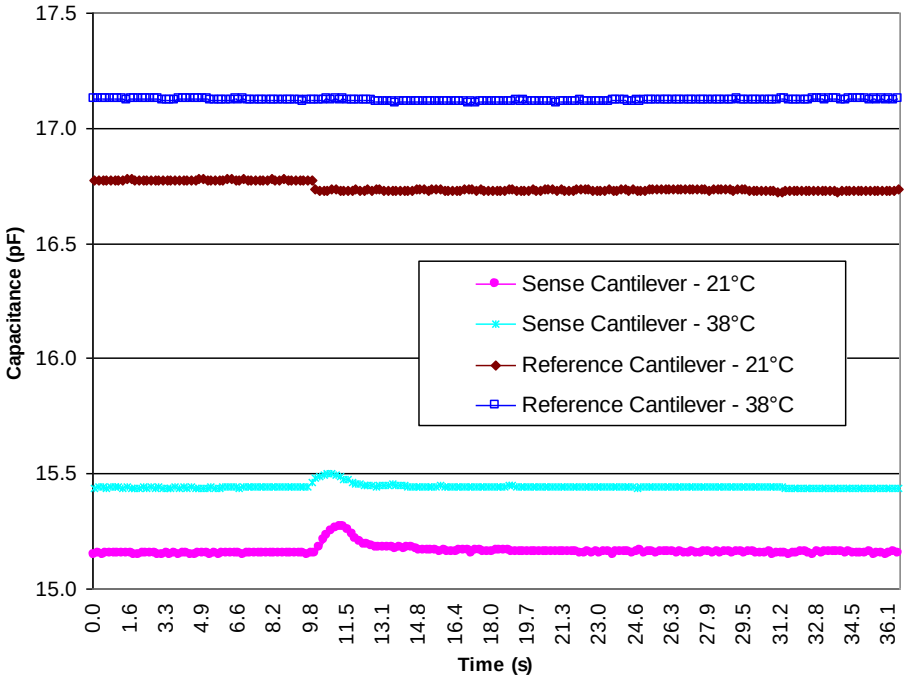

Figure 52 - Graph showing both 175µm long cantilevers operating at two temperatures to demonstrate temperature compensation. The small change on the reference cantilever at 21°C can be attributed to the testing setup shifting slightly when the hydrogen is released

.

Next, the temperature of the sensor is varied with the heater to demonstrate the common-mode temperature change of both cantilevers. Measurements are taken using the same conditions as the previous experiment, and each cantilever is exposed to impulse of hydrogen. Measurements were first performed at ambient (21°C). Next, the temperature was raised to 38°C and held. Measurements were repeated and the results are shown in Figure 52. The Pd functionalized cantilever capacitance increased by 289fF, while the reference cantilever capacitance increased by 375fF. The observed difference is likely due to a slight thickness error of the metal films, as the process was controlled by hand. As measured, the differential capacitance error due to temperature is reduced to 4.9fF/ºC compared with 16.6fF/ºC using a bare reference cantilever. This error can be further optimized with tighter control over the metal deposition process. This experiment successfully demonstrates the temperature compensation technique.

A.6 – Conclusions

The first instance of a microfabricated differential-mode hydrogen sensor has been realized which demonstrates the concept of temperature compensation using a functionalized reference cantilever. Measurements performed on the device verify the functionality of the sensor and selective response is demonstrated from the sense cantilever. The ambient temperature of the sensor was varied and the temperature induce differential capacitance error was reduced to 4.9fF/ºC compared with 16.6fF/ºC for a bare reference. This temperature compensation technique is applicable to many applications where a bimorph system exists and a reference measurement can be performed. By engineering a reference structure with an appropriate material to apply equal thermal

stresses, the temperature dependence of a sensor can be made common mode and removed during measurement. This compensation removes the need for additional temperature correction circuitry, lowering the cost, complexity, and power consumption of the sensor.

This work is published as:

R.C. Roberts**,** N.C. Tien "Microfabricated differential-mode gas sensor utilizing temperature compensation," *Technical Digest , The 9th IEEE Conference on Sensors (Sensors 2010),* Waikoloa, Hawaii, November, 2010, pp. 1530-1533.

Appendix B – Gold-NP Synthesis

The hexanethiol-encapsulated gold nanoparticles used in this work were synthesized using a procedure adapted by Molesa [1]. This two phase synthesis process was originally developed by Brust *et al.* [2] and refined by Hostetler *et al.* [3]. The method was further developed Huang *et al.* [4] for printed electronics applications. For completeness, details on changing the nanoparticle encapsulating surfactant are included based on the work of Molesa and shown in Table 12. For this work, all experiments were performed using gold nanoparticles synthesized with hexanethiol in a 4:1 molar ratio.

B.1 – Equipment Used

- 500mL beaker
- 1000mL Erlenmeyer flask
- 1000mL Erlenmeyer vacuum flask
- Fine glass frit
- 1000mL separatory funnel
- 1000mL rotary flask
- Large stir bar
- Rotary evaporator
- Ultrasonic bath
- Laboratory scale
- Stirring hot plate
- 5mL pipette

B.2 – Chemicals Required

- Hydrogen tetrachloroaurate(III) hydrate ($HAuCl_4 \cdot xH_2O$)
- 1-Hexanethiol ($C_6H_{13}SH$) or alternative alkanethiol
- Sodium borohydride ($NaBH_4$)
- Tetraoctylammonium Bromide ($C_{32}H_{68}BrN$)
- Toluene (C_7H_8)
- Deionized water (H_2O)
- Ethanol (C_2H_5OH)
- Acetone ($(CH_3)_2CO$)
- Dry Ice (CO_2)

B.3 – General Procedure

The laboratory procedure can be divided into two phases; synthesis and purification. During synthesis, alkanethiol-encapsulated gold nanoparticles are formed by first dissolving the ionic gold precursor in water and then transferred it to toluene using tetraoctylammonium bromide, an organic transfer reagent. The organic phase of this solution is then isolated, and the alkanethiol-encapsulate is added in the appropriate molar ratio to achieve the desired nanoparticle size. The alkyl chain length is selected to achieve the desired sintering temperature of the resulting nanoparticles. The resulting solution is then reduced using sodium borohydride and stirred for several hours.

Purification is then performed by first isolating the organic phase of the solution and then evaporating of the toluene using rotary evaporation. The resulting nanoparticles are then dissolved in ethanol and chilled in a freezer in preparation for filtering. Finally,

the nanoparticles are extracted using vacuum evaporation, rinsed, and are then ready for use.

B.5 – Detailed Procedure

A detailed laboratory procedure of the gold nanoparticle synthesis process is described below for a 2.5g quantity of hydrogen tetrachloroaurate(III) hydrate. It should be noted that hydrogen tetrachloroaurate(III) hydrate is sensitive to light and air, so it should be stabilized by quick dissolution in water (step 2 below). Hydrogen tetrachloroaurate(III) hydrate is commonly procured in 5g increments, so it is recommended that two synthesis procedures are either run in parallel or sequentially to maximize gold usage.

Synthesis:

1) 645mL toluene and a large stir bar are added to a 1000mL Erlenmeyer flask. 12.10g of tetraoctylammonium bromide is then added and stirred vigorously (700-800 rpm), forming the organic phase.
2) Using a 500 mL beaker, add 2.5g of $HAuCl_4 \cdot xH_2O$ to 200mL deionized water to form a pale yellow aqueous phase. If starting with 5g of $HAuCl_4 \cdot xH_2O$, dissolve it using 400mL deionized water immediately and then run two synthesis procedures.
3) Add 200mL of the gold aqueous solution to the vigorously stirred organic phase from step 1. After mixing, turn off the stir bar and the two phases will begin to separate into a clear aqueous phase and an orange-brown organic phase.

4) Transfer the solution into the 1000mL separatory flask and allow for the two phases to fully separate. Next, isolate the orange-brown organic phase and transfer it to a 1000mL Erlenmeyer flask.
5) Using the pipette, add the desired molar ratio of hexanethiol (or other alkanethiol) for the formation of nanoparticles of the desired size and thermal properties. For this work, a 4 to 1 thiol to gold molar ratio of hexanethiol (4.125mL) was selected to achieve 1.5-2.5nm nanoparticles. The solution is then stirred vigorously (700-800 rpm) at room temperature for 15 minutes as nanoparticles form and the solution transforms to a pale yellow/clear in color.
6) In a 500mL beaker, form the reduction solution by mixing 3.065g of $NaBH_4$ in 200mL deionized water.
7) While continuing to vigorously stir nanoparticle solution (organic phase), slowly pour in the reduction solution from the previous step over a 20 second period. This reaction will become very dark in color.
8) Cover the top of the Erlenmeyer flask with aluminum foil and stir the solution for 3.5 hours or more at room temperature.

Purification:

1) Turn of the stir bar and then transfer the solution into the 1000mL separatory flask and allow for the two phases to fully separate.
2) Isolate the dark organic phase as before and transfer it to a 1000mL rotary flask.

3) Using a rotary evaporator, extract the solvent from the organic phase. Make sure to add dry ice to the trap to condense the volatiles. Keep the water bath temperature below 35°C to avoid nanoparticle degradation
4) Suspend the nanoparticles in 250mL ethanol. Sonicate the solution in the rotary flask for 5 minutes to ensure full dissolution of nanoparticles, then transfer it to a 500mL bottle with an air tight lid.
5) Place the solution in a freezer overnight to allow the nanoparticles to agglomerate for vacuum extraction.
6) Using a 1000mL vacuum flask and a fine glass frit, filter the nanoparticle solution and then rinse it with at least 645mL ethanol (750mL used in practice) and 1210mL acetone (1250mL used here). The vacuum flask will need to be emptied during this process, so watch the filtration steps carefully.
7) Leave the nanoparticles on the frit under vacuum for at least 15 minutes to allow them to dry.
8) The nanoparticles are now ready for use. They can be stored in a refrigerator or freezer in an air-tight bottle. For this work, they were weighed an immediately suspended in the desired solvent to form a gold nanoparticle ink.

Table 12 - Alkanethiol Quantity for Au Nanoparticle Synthesis (adapted from [1])

Chemical	**Thiol Encapsulant to Gold Molar Ratio for 2.5g Hydrogen tetrachloroaurate(III) hydrate (0.0073575 mol)**							
	1:1		**3:1**		**4:1**		**1/12:1**	
Dodecanethiol	1.489g	1.762mL	4.466g	5.285mL	5.954g	7.046mL	0.1241g	0.1468mL
Octanethiol	1.076g	1.277mL	3.228g	3.830mL	4.304g	5.106mL	0.0897g	0.1064mL
Hexanethiol	0.870g	1.038mL	2.609g	3.114mL	3.478g	4.152mL	0.7245g	0.0865mL
Butanethiol	0.664g	0.788mL	1.991g	2.364mL	2.654g	3.152mL	0.0553g	0.0657mL

Table 13 - Important Chemical Properties for Nanoparticle Synthesis (from [1])

Chemical	Formula	MW (amu)	Mp (°C)	Bp (°C)	d (g/mL)
Hydrogen tetrachloroaurate(III) hydrate	$HAuCl_4$•xH2O	339.79	--	--	3.9
1-Dodecanethiol	$C_{12}H_{25}SH$	202.4	-7	266-283	0.845
1-Octanethiol	$C_8H_{17}SH$	146.3	-49	197-200	0.843
1-Hexanethiol	$C_6H_{13}SH$	118.24	-80	150-154	0.838
1-Butanethiol	C_4H_9SH	90.19	-116	98	0.842
Sodium Borohydride	$NaBH_4$	37.83	36	400	0.945
Tetraoctylammonium Bromide	$(C_8H17)_4BrN$	546.82	97-99	--	--
Toluene	$C_6H_35CH_3$	92.1402	-93	110.6	0.867
Deionized water	H_2O	18.0152	0	100	0.955
Ethanol	C_2H_5OH	58.0798	-94.3	56.2	0.7857
Acetone	C_3H_6O	46.0688	-114.1	78.3	0.789

Appendix C – Stiffness versus Sintering Conditions

In order to gain an understanding on the evolution of the mechanical characteristics of gold films realized by sintering hexanethiol-encapsulated gold nanoparticles, initial stiffness measurements were performed. The mechanical properties of these films have not been studied in the literature, so there is great opportunity to characterize this material for use in inkjet printed microelectromechanical systems.

In order to build prototype printed MEMS, suitable process conditions must be selected which yield a favorable material. The resistance measurements presented previously in chapter 5 have shown that the electrical properties continue to evolve well after the onset of sintering resulting in an electrically conductive gold film. Understanding how the mechanical properties evolve is of similar interest in order to select suitable sintering parameters.

The stiffness of a material is the measure of resistance to deformation when a force is applied. This is an extrinsic property of a sample that relates to the elastic modulus of a material but also depends upon both the shape and boundary conditions used. This measure is useful for design as it allows for a practical measure of aggregate material flexibility without accounting for many complex parameters affecting the stiffness of a material. The stiffness can then be used to estimate the elastic modulus of a sample given suitable sample conditions.

Accordingly, the stiffness of sintered gold nanoparticle films will be examined to look at the changes in this property as a result of varied sintering durations. In doing so, the stability of the aggregate material properties relating to stiffness can be visualized. Understanding this effective stiffness will then allow for the selection of appropriate sintering conditions such that electrically

and mechanically stable films can be realized for the future development and study of inkjet printed MEMS.

The effective stiffness has been measured using an Agilent G200 Nano Indenter operating in continuous stiffness measurement (CSM) mode with a Berkovich tip for the sintered gold films. In CSM mode, the nanoindenter tip oscillates with a magnitude of several nanometers taking measurements of the stiffness of the material during each oscillation. The nanoindenter then further penetrates into the material and takes the next measurement, allowing for the stiffness measurements versus depth of materials. The nanoindenter stiffness measurement profiles can then be analyzed to select appropriate sintering conditions for further development of inkjet printed MEMS.

C.1 – Effective Stiffness on <100> Silicon

Hexanethiol-encapsulated gold nanoparticle wires (10%wt, 60µm diameter nozzle) were printed on both clean borosilicate glass (Corning 0215), and bare <100> silicon, to provide substrates of differing stiffness as reported previously by Saha and Nix [1]. After deposition the solvent was evaporated for 10 minutes at 130°C before being transferred to the 200°C hotplate for sintering. Samples were sintered for three durations; just before the resistance drop (7 minutes), just after the resistance drop (13 minutes), and after a full 60 minutes. CSM nanoindentation measurements of the effective stiffness of the sintered gold films on a <100> silicon substrate are shown in Figure 53.

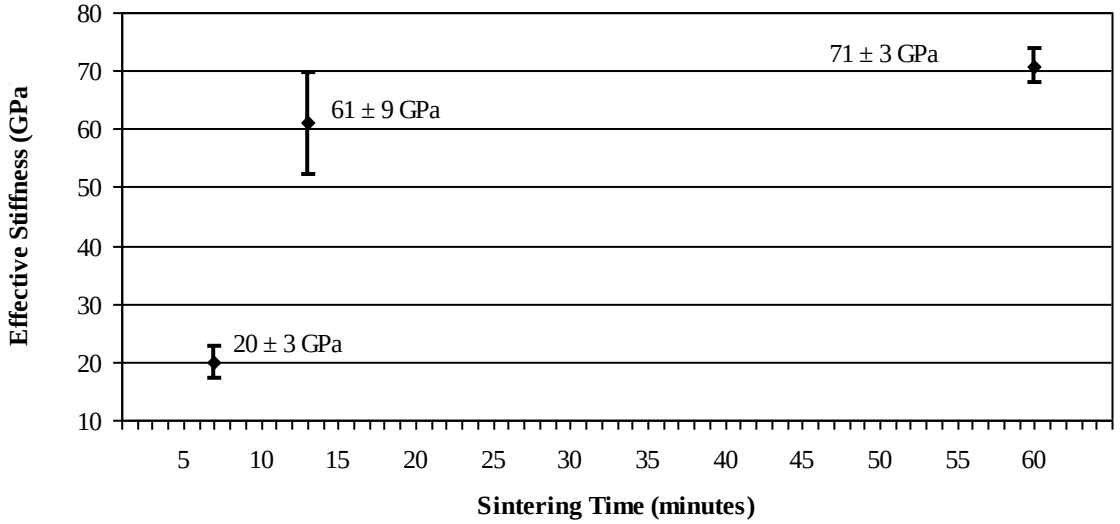

Figure 53 – Effective stiffness of the gold films on silicon after sintering at 200ºC in air for 7, 13, and 60 minutes respectively. The resistance decrease for this gold film, indicating the onset of sintering, was measured to be at 11 minutes.

As the Young's modulus of <100> silicon is much greater than gold, detection of when the nanoindenter reached the substrate was simplified. After 60 minutes of sintering, the measured effective stiffness of the gold film was 71 ± 3GPa, which is approaching the expected modulus of bulk gold, 79GPa. The measured effective stiffness after 7 minutes of 20 ± 3GPa is much softer, as expected, as this should be before sintering of the gold begins. At the 13 minute mark, two minutes after the predicted onset of gold sintering, a large increase in modulus was observed, 61 ± 9GPa. The variation in modulus of this sample was much larger than at the other time points. The larger variation in modulus likely indicates that the gold film is still inhomogeneous and undergoing structural changes.

C.2 – Effective Stiffness on High-Temperature Enamel

As SEM images of the sintered gold films exhibited different microstructure under identical deposition and sintering conditions when printed onto different substrates, CSM nanoindentation measurements were performed on sintered gold pads deposited onto the high-temperature dielectric enamel used throughout this work.

Hexanethiol-encapsulated gold nanoparticles were synthesized and suspended in α-terpineol (15%wt) forming the ink which was subsequently loaded into an inkjet head with a 30μm diameter piezoelectric nozzle. The print-head was driven with a 20Hz bipolar waveform using 2/5/2/5/2μs timing parameters at ±30V. Each gold layer in the processed is patterned through two successive passes onto a 140°C platen yielding 750μm by 750μm square pad. The feed rate on the printer was set to overlap the previous droplet by 50%. After deposition the gold structures were held at 140°C for 10 minutes to drive off solvent and then ramped to 200°C.

Samples were then removed from the hotplate after 1 minute, 3 minute, 10 minutes, and 60 minutes and quickly placed on a large block of aluminum to rapidly cool the samples. The resistivity and color of the printed nanoparticle films were observed to detect the onset of sintering, which occurred 2 minutes after ramping up the hotplate temperature to 200°C, as expected.

CSM nanoindentation of each of the samples was performed using the Young's Modulus measurement setting as an estimator of the effective stiffness of the samples and the data is shown in Figure 54. Additionally, stiffness measurements were made on the bare substrate and the calibration standard for reference.

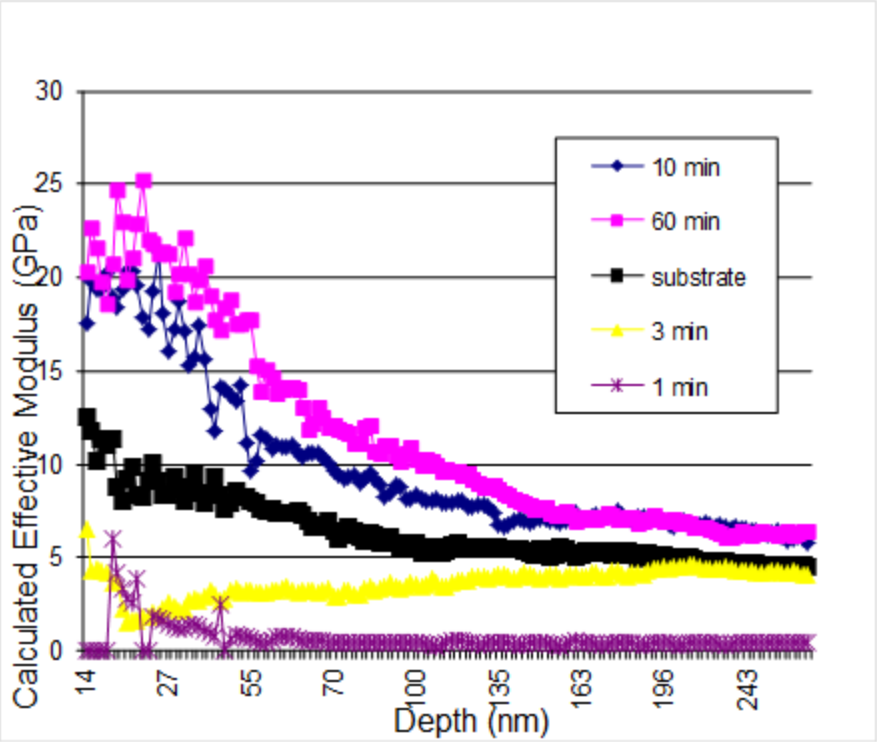

Figure 54 - CSM Nanoindentation Data of sintered Au-NP films on enamel

The data reveals interesting trends as the nanoindenter tip penetrates the material. As expected, the loose gold nanoparticles are quite soft before the onset of sintering at the two minute point during sintering. Interestingly, the stiffness of the gold film still appears soft at the 3 minute sintering duration indicate that the gold film may still be undergoing structural changes. Of most interest in this study however, is an examination of the two effective stiffness measurements at the 10 and 60 minute marks, respectively. While close in value, the 60 minute measurement yields a higher measured stiffness versus depth, indicating that the gold film being measured has likely continued to evolve and densify. This agrees well with measurements performed on the silicon substrate.

C.3 – Summary

Continuous stiffness monitoring (CSM) nanoindentation measurements were performed on gold films patterned onto <100> Silicon substrates and the dielectric enamel used in this work. In both cases, the stiffness of this material was found to continue to increase for periods beyond the onset of sintering. These observations trend well with changes in resistance. Accordingly, it is advisable to sinter gold nanoparticles for an extended period of time beyond the onset of sintering as observed by a color or conductivity changes as is currently suggested in the literature in order to minimize material variation due to subsequent temperature process steps. The mechanical properties of sintered gold films have not been studied in the literature. Accordingly, further study should be performed to measure the stiffness of freestanding microfabricated sintered gold structures.

Bibliography

Chapter 1

[1] J.C. Eloy, *"(2010) Status of the MEMS industry." Yole Développement, MIS, Available at: http://www.i-micronews.com/reports/Status-MEMS-Industry/159/ (Accessed Sept. 18, 2011)*

[2] Subramanian, V.; Chang, P.C.; Lee, J.B.; Molesa, S.E.; Volkman, S.K.; , "Printed organic transistors for ultra-low-cost RFID applications," *Components and Packaging Technologies, IEEE Transactions on* , vol.28, no.4, pp. 742- 747, Dec. 2005

[3] Rogers, J. A. and Bao, Z. (2002), "Printed plastic electronics and paperlike displays." *Journal of Polymer Science Part A: Polymer Chemistry*, 40: 3327–3334. doi: 10.1002/pola.10405

[4] Parashkov, R.; Becker, E.; Riedl, T.; Johannes, H.-H.; Kowalsky, W.; , "Large Area Electronics Using Printing Methods," *Proceedings of the IEEE* , vol.93, no.7, pp.1321-1329, July 2005

[5] E. Mounier, and B.Smith, *"(2011) Printed Electronics: Reality vs. Hype." Yole Développement, MIS, Available at:* http://www.i-micronews.com/reports/Printed-Electronics-vs-Hype/212/ *(Accessed Sept. 28, 2011)*

[6] The printed world: 3D printing. The Economist, 12-18 Feb 2011, Volume: 398 Issue: 8720 pp.75-77

[7] Anna Bellini, Selçuk Güçeri, (2003),"Mechanical characterization of parts fabricated using fused deposition modeling", Rapid Prototyping Journal, Vol. 9 Iss: 4 pp. 252 – 264

[8] Mukesh Agarwala, David Bourell, Joseph Beaman, Harris Marcus, Joel Barlow, (1995),"Direct selective laser sintering of metals", Rapid Prototyping Journal, Vol. 1 Iss: 1 pp. 26 – 36

[9] A. Anderson, "Report to the President on Ensuring American Leadership in Advanced Manufacturing," (Executive Office to the President and President's Council of Advisors on Science and Technology, June 2011), available at http://www.whitehouse.gov/sites/default/files/microsites/ostp/pcast-advanced-manufacturing-june2011.pdf

[10] K. E. Petersen, "Silicon as a mechanical material," Proceedings of the IEEE, vol. 70, pp. 420-457, 1982.

[11] G.T.A. Kovacs, *Micromachined Transducers Sourcebook*; WCB/McGraw-Hill: Boston, 1998

[12] M. Madou, *Fundamentals of Microfabrication*, CRC Press, Boca Raton, FL 1997.

[13] J. Perelaer and U.S. Schubert, "Inkjet Printing and Alternative Sintering of Narrow Conductive Tracks on Flexible Substrates for Plastic Electronic Applications, Radio Frequency Identification Fundamentals and Applications Design Methods and Solutions," Cristina Turcu (Ed.), ISBN: 978-953-7619-72-5, InTech, 2010

[14] K-S. Kwon, "Waveform Design Methods for Piezo Inkjet Dispensers Based on Measured Meniscus Motion," *J. Microelectromechanical Systems*, 18 (5), pp. 1118-1125, 2009.

Chapter 2

[1] S. Busato, A. Belloli, P. Ermanni, "Inkjet printing of palladium catalyst patterns on polyimide film for electroless copper plating," *Sensors and Actuators B: Chemical*, Volume 123, Issue 2, 21 May 2007, Pages 840-846.

[2] B-J. de Gans, and U.S. Schubert, “Inkjet Printing of Well-Defined Polymer Dots and Arrays,” *Langmuir* 2004, *20,* 7789-7793.

[3] B. J. de Gans, P. C. Duineveld, and U.S. Schubert,”Inkjet Printing of Polymers: State of the Art and Future Developments,” *Adv. Mater.,* Vol. 16, No. 3. (2004), pp. 203-213.3883236

[4] P. Calvert, “Inkjet Printing for Materials and Devices,” *Chem. Mater.* 2001, *13,* 3299-3305.

[5] K. Crowley, E. O'Malley, A. Morrin, M.R. Smyth, and A.J. Killard, "An aqueous ammonia sensor based on an inkjet-printed polyaniline nanoparticle-modified electrode," *Analyst* 133 (2008) 391-399.

[6] E. Chow, J. Herrmann, C.S. Barton, B. Raguse, and L.Wieczorek, ”Inkjet-printed gold nanoparticle chemiresistors: Influence of film morphology and ionic strength on the detection of organics dissolved in aqueous solution,” *Analytica Chimica Acta* 632 (2009) 135–142.

[7] C.M. Hong and S.Wagner (1999). “Jet Printing of Copper Lines at 200°C Maximum Process Temperature.” *MRS Proceedings*, 558 , 387 doi:10.1557/PROC-558-387

[8] C. M. Hong, and S.Wagner, "Inkjet printed copper source/drain metallization for amorphous silicon thin-film transistors," *Electron Device Letters, IEEE* , vol.21, no.8, pp.384-386, Aug 2000

[9] C.M. Hong, “Jet printed copper metallization, Ph.D. Dissertation,” Princeton University, 2000.

[10] Y. Wu,Y. Li, and B.S. Ong, “A Simple and Efficient Approach to a Printable Silver Conductor for Printed Electronics,” *Journal of the American Chemical Society* 2007 129 (7), 1862-1863

[11] Y. Wu,Y. Li, and B.S. Ong, "Printed Silver Ohmic Contacts for High-Mobility Organic Thin-Film Transistors," *Journal of the American Chemical Society* 2006 128 (13), 4202-4203

[12] T. Sekitani, M. Takamiya, Y. Noguchi, S. Nakano, Y. Kato, T. Sakurai, and T. Someya, "A large-area wireless power-transmission sheet using printed organic transistors and plastic MEMS switches," *Nature Materials*, Vol. 6, Iss. 6, pp. 413-417, 2007.

[13] V. Subramanian, J.M.J. Frechet, P.C. Chang, D.C. Huang, J.B. Lee, S.E. Molesa, A.R. Murphy, D.R. Redinger, and S.K. Volkman, "Progress Toward Development of All-Printed RFID Tags: Materials, Processes, and Devices," *Proceedings of the IEEE* , vol.93, no.7, pp.1330-1338, July 2005

[14] S. Fuller, E.J. Wilhelm, and J.M. Jacobson, "Ink-Jet Printed Nanoparticle Microelectromechanical Systems," J. Microelectromechanical Systems, 11 (54), pp. 54-60, 2002.

[15] E.W. Lam, H. Li, and M.A. Schmidt, **"**Silver Nanoparticle Structures Realized By Digital Surface Micromachining," TRANSDUCERS 2009. International Conference on, pp. 1698-1701, 2009.

[16] E.W. Lam, and M.A. Schmidt, *"A Surface Micromachining Process by Direct Printing: An Alternative MEMS Fabrication Method,"* Technologies for Future Micro-Nano Manufacturing (MFG2011), August 8-10, 2011, Napa, Ca.

[17] M. Cruz, O. Azucena, J. Kubby (2007). *Inkjet Printer for Use in Fabrication of MEMS* [PowerPoint slides]. Retrieved from http://mems.soe.ucsc.edu/media/test_inkjet.pdf

[18] E.B. Duoss, B. Yeop Ahn, T.F. Malkowski, J.J. Adams, J.T. Bernhard, and J.A. Lewis, "Direct-Write Assembly of Functional Inks for Planar and 3D Microstructures,"

Technologies for Future Micro-Nano Manufacturing (MFG2011), August 8-10, 2011, Napa, Ca.

[19] M.T. Demko, J.C. Cheng and A.P. Pisano,"High-resolution direct patterning of gold nanoparticles by the microfluidic molding process," *Langmuir*, *26* (22), pp. 16710-16714, 2010.

[20] S.H. Ko, J. Chung, N. Hotz, K.H. Nam, and C.P. Grigoropoulos, "Metal nanoparticle direct inkjet printing for low-temperature 3D micro metal structure fabrication," *J. Micromech. Microeng.*, 20, 125010, 2010.

[21] M-C. Daniel and D. Astruc, "Gold Nanoparticles: Assembly, Supramolecular Chemistry, Quantum-Size-Related Properties, and Applications toward Biology, Catalysis, and Nanotechnology," *Chem. Rev.* 104 (2004) 293-346

[22] M. M. Maye, W. Zheng, F.L. Leibowitz, N.K. Ly, and C-J. Zhong, "Heating-Induced Evolution of Thiolate-Encapsulated Gold Nanoparticles: A Strategy for Size and Shape Manipulations," *Langmuir* 2000 16 (2), 490-497

[23] O.V. Salata, "Review:Applications of nanoparticles in biology and medicine," *Journal of Nanobiotechnology* 2004, **2**:3

[24] R.Weissleder, G. Elizondo, J. Wittenburg, C.A. Rabito, H.H Bengele, L. Josephson, "Ultrasmall superparamagnetic iron oxide: characterization of a new class of contrast agents for MR imaging," *Radiology* 175 (1990) 489-493.

[25] J. Yoshida, and T. Kobayashi, "Intracellular hyperthermia for cancer using magnetite cationic liposomes," *J Magn Magn Mater* 194 (1999) 176-184

[26] P. Buffat and J. P. Borel, "Size effect on the melting point of gold particles," *Physic. Rev. A*, vol. 13, pp. 2287–2298, 1976.

[27] M.J. Hostetler, J.E. Wingate, C-J. Zhong, J.E. Harris, R.W. Vachet, M.R. Clark, J.D. Londono, S.J. Green, J.J. Stokes, G. D. Wignall, G. L. Glish, M.D. Porter, N.D. Evans, and R.W. Murray, 'Alkanethiolate Gold Cluster Molecules with Core Diameters from 1.5 to 5.2 nm: Core and Monolayer Properties as a Function of Core Size," *Langmuir* 1998 14 (1), 17-30

[28] Subramanian, V.; Chang, P.C.; Lee, J.B.; Molesa, S.E.; Volkman, S.K.; , "Printed organic transistors for ultra-low-cost RFID applications," *Components and Packaging Technologies, IEEE Transactions on* , vol.28, no.4, pp. 742- 747, Dec. 2005

[29] S.E. Molesa, "Ultra-Low-Cost Printed Electronics," Ph.D. Dissertation, U.C. Berkeley, 2006.

[30] D. Huang, F. Liao, S. Molesa, D. Redinger and V. Subramanian, "Plastic-Compatible Low Resistance Printable Gold Nanoparticle Conductors for Flexible Electronics," *J. Electrochemical Society,* 150, pp. G412–G417, 2003.

[31] D. Soltman and V. Subramanian, "Inkjet-Printed Line Morphologies and Temperature Control of the Coffee Ring Effect," *Langmuir* 2008 24 (5), 2224-2231

[32] D. Redinger, S. Molesa, Y. Shong , R. Farschi, V. Subramanian, An ink-jet-deposited passive component process for RFID, *Electron Devices, IEEE Transactions on* , vol.51, no.12, pp. 1978- 1983, Dec. 2004

[33] S.K. Volkman, Y. Pei, D. Redinger, S. Yin, and V. Subramanian, *Ink-Jetted Silver/Copper Conductors for Printed RFID Applications*, Flexible Electronics 2004—Materials and

Device Technology, edited by Norbert Fruehauf, Babu R. Chalamala, Bruce E. Gnade, and Jin Jang (Mater. Res. Soc. Symp. Proc.814, Warrendale, PA , 2004), I7.8

[34] J. Chung, S. Ko, N. R. Bieri, C. P. Grigoropoulos, and D. Poulikakos,"Conductor microstructures by laser curing of printed gold nanoparticle ink," *Appl. Phys. Lett.* 84, 801 (2004); doi:10.1063/1.1644907

[35] M.T. Demko, University of California at Berkeley, Private Communication. August 2011.

Chapter 3

[1] S.H Ko, *et al*., "All-inkjet-printed flexible electronics fabrication on a polymer substrate by low-temperature high-resolution selective laser sintering of metal nanoparticles," Nanotechnology 18,345202, 2007.

[2] C. M. Hong, and S.Wagner, "Inkjet printed copper source/drain metallization for amorphous silicon thin-film transistors," *Electron Device Letters, IEEE* , vol.21, no.8, pp.384-386, Aug 2000

[3] Y. Wu,Y. Li, and B.S. Ong, "A Simple and Efficient Approach to a Printable Silver Conductor for Printed Electronics," *Journal of the American Chemical Society* 2007 129 (7), 1862-1863

[4] S.K. Volkman, Y. Pei, D. Redinger, S. Yin, and V. Subramanian, *Ink-Jetted Silver/Copper Conductors for Printed RFID Applications,* Flexible Electronics 2004—Materials and Device Technology, edited by Norbert Fruehauf, Babu R. Chalamala, Bruce E. Gnade, and Jin Jang (Mater. Res. Soc. Symp. Proc.814, Warrendale, PA , 2004), I7.8

[5] Cabot Conductive Ink CCI-300; Data Sheet; Cabot Printed Electronic Materials: Albuquerque, NM, USA, 2009.

[6] Q. Liu, D.T. McCormick, R.C. Roberts, N.C. Tien, "Nanoscale Al-Al and Cu-Cu Contacts," *Solid-State Sensors, Actuators and Microsystems Conference, 2007. TRANSDUCERS 2007. International* , pp.1593-1596, 10-14 June 2007

[7] C.M. Hong, "Jet printed copper metallization, Ph.D. Dissertation," Princeton University, 2000.

[8] S. Kal, A. Bagolini, B. Margesin, and M. Zen, "Stress and resistivity analysis of electrodeposited gold films for MEMS application," Microelectronics Journal, Vol, 37 Iss, 11, 2006, pp. 1329-1334.

[9] V. Subramanian, J.M.J. Frechet, P.C. Chang, D.C. Huang, J.B. Lee, S.E. Molesa, A.R. Murphy, D.R. Redinger, and S.K. Volkman, "Progress Toward Development of All-Printed RFID Tags: Materials, Processes, and Devices," *Proceedings of the IEEE* , vol.93, no.7, pp.1330-1338, July 2005

[10] Subramanian, V.; Chang, P.C.; Lee, J.B.; Molesa, S.E.; Volkman, S.K.; , "Printed organic transistors for ultra-low-cost RFID applications," *Components and Packaging Technologies, IEEE Transactions on* , vol.28, no.4, pp. 742- 747, Dec. 2005

[11] N.R. Bieri, J. Chung, D. Poulikakos and C.P. Grigoropoulos, "An experimental investigation of microresistor laser printing with gold nanoparticle-laden inks," Applied Physics A: Materials Science & Processing, Vol. 80, Num. 7 (2005), pp. 1485-1495.

[12] D. Huang, F. Liao, S. Molesa, D. Redinger and V. Subramanian, "Plastic-Compatible Low Resistance Printable Gold Nanoparticle Conductors for Flexible Electronics," *J. Electrochemical Society,* 150, pp. G412–G417, 2003.

[13] P. Buffat and J. P. Borel, "Size effect on the melting point of gold particles," *Physic. Rev. A*, vol. 13, pp. 2287–2298, 1976.

[14] S. Fuller, E.J. Wilhelm, and J.M. Jacobson, "Ink-Jet Printed Nanoparticle Microelectromechanical Systems," *J. Microelectromechanical Systems,* 11 (54), pp. 54-60, 2002.

[15] K. Wang, "Effect of Multiple Alkanethiol Ligands on Solubility and Sintering Temperature of Gold Nanoparticles," M.S. Research Project Report, University of California at Berkeley, 2010.

[16] S.E. Molesa, "Ultra-Low-Cost Printed Electronics," Ph.D. Dissertation, U.C. Berkeley,2006.

[17] M. Brust, M. Walker, D. Bethell, D. J. Schiffrin, and R. Whyman, "Synthesis of thiol-derivatised gold nanoparticles in a two-phase Liquid-Liquid system." *Journal of the Chemical Society Chemical Communications* 1994.7 (1994) : 801.

[18] R.C. Roberts, and N.C. Tien, "Hexanethiol Encapsulated Gold Nanoparticle Ink For Printed Metal MEMS," Technologies for Future Micro-Nano Manufacturing (MFG2011), August 8-10, 2011, Napa, Ca.

[19] Linuxcnc.org, "EMC2 User Manual V2.5, 2012-01-18" [pdf], available online at http://www.linuxcnc.org/docs/EMC2_User_Manual.pdf

[20] Microfab, "Technote 99-02: Fluid Properties Effects," Microfab Technologies Inc., 1999. Available at: http://www.microfab.com/images/pdfs/technote99-02.pdf

[21] Microfab, "Technote 99-04: Orifice Diameter Effects," Microfab Technologies Inc., 1999. Available at: http://www.microfab.com/images/pdfs/technote99-04.pdf

[22] Microfab, "Technote 99-05: Performance of Four Fluids," Microfab Technologies Inc., 1999. Available at: http://www.microfab.com/images/pdfs/technote99-05.pdf

[23] Microfab, "Technote 99-03: Drive Waveform Effects," Microfab Technologies Inc., 1999. Available at: http://www.microfab.com/images/pdfs/technote99-03.pdf

[24] Microfab, "Satellites occurrence and approaches to eliminate them," Microfab Technologies Inc., 2007. Available at: http://www.microfab.com/images/pdfs/Satellites_version_09_26_07.pdf

[25] C. Rensch, "Creation of Small Microdrops," Microfab Technologies Inc., 2006. Available at: http://www.microfab.com/images/pdfs/smalldrops_Nov06_v3.pdf

[26] R.L. Smith, "Oxygen Plasma Surface Activation of Polynorbornene for Bonding to Glass with Applications to Microfluidic Systems," M.S. Thesis, Case Western Reserve University, 2011.

[27] Cornell Nanobiotechnology Center, "Parylene Conformal Coating Specifications & Properties," Cornell University, available at: http://www.nbtc.cornell.edu/facilities/downloads/Parylene%20Information%20Sheets.pdf

[28] S. Jinno, H.C. Moeller, C.L. Chen, B. Rajalingam, B.G. Chung, *et al*., "Microfabricated multilayer parylene-C stencils for the generation of patterned dynamic co-cultures," J Biomed Mater Res A 86: 278–288, 2008.

[29] V. Sharma, "Characterization and Optimization of Photonic Devices Fabrciated Using Femtosecond Laser Micro-Machining," M.S. Thesis, Massachusetts Institute of Technology, 2005.

[30] R.L. DeRosa, P.A. Schader, and J.E. Shelby, "Hydrophilic nature of silicate glass surfaces as a function of exposure condition," Journal of Non-Crystalline Solids, Vol. 331, Iss. 1–3,, pp. 32-40, 2003.

[31] DuPont, “Technical Data Sheet: DuPont™ Kapton® HN polyimide film”. Available at http://www2.dupont.com/Kapton/en_US/assets/downloads/pdf/HN_datasheet.pdf

[32] Ghosh, I. *et al*. “Surfaces Properties of Chemically Modified Polyimide Films.” Journal of Adhesion Science and Technology. Vol 11. no.6. 1997. Abstract.

[33] "94% Alumina Material Properties," Accuratus Ceramic Corporation. Available at: http://accuratus.com/pdf/94aluminaprops.pdf

[34] E.W. Lam, “Fabrication and material characterization of silver cantilevers via direct surface micromachining,” M.S. Thesis, Massachusetts Institute of Technology, 2008.

Chapter 4

[1] K. E. Petersen, “Silicon as a mechanical material,” Proc. IEEE, vol.70, pp. 420–457, May 1982.

[2] G. T. A. Kovacs, Micromachined Transducers Sourcebook. New York: McGraw-Hill, 1998.

[3] D. A. Koester, R. Mahadevan, A. Shishkoff, and K. W. Markus, "SmartMUMP's design handbook including MUMP's introduction and design rules", *MEMS Technology Applications Center*, pp.1 -8 1996

[4] M. Madou, Fundamentals of Microfabrication, 1st ed. Boca Raton, FL: CRC Press, 1997.

[5] H. Chen, W. Sheng, N. Xi, M. Song, and Y. Chen , "Automated robot trajectory planning for spray painting of free-form surfaces in automotive manufacturing," *Robotics and Automation, 2002. Proceedings. ICRA '02. IEEE International Conference on*, vol.1, pp. 450- 455, 2002

[6] P.N. Atkar, A.Greenfield, D.C. Conner, H. Choset, and A.A. Rizzi, “Uniform Coverage of Automotive Surface Patches,” *The International Journal of Robotics Research November 2005 24:* pp. 883-898.

[7] H. Greenbaum and D. Rubinstein (November 4, 2011). "The Origin of Spray Paint". *The New York Times Magazine*. Retrieved from: http://www.nytimes.com/2011/11/06/magazine/who-made-spray-paint.html

[8] SU-8 MicrosprayTM Datasheet. Microchem. 5/25/2012. Available at: http://www.microchem.com/pdf/MicroSprayTMSU-8datasheetver1_1.pdf

[9] J. K. Antonio, R. Ramabhadran, and T. L. Ling, "A framework for optimal trajectory planning for automated spray coating", *Int. J. Robot. Automat.*, vol. 12, no. 4, pp.124 - 134 1997

[10] R. Lambourne and T. A. Strivens (eds.), Paint and Surface Coatings: Theory and Practice. 2nd Edition. New York: Woodhead Publishing Ltd, 1999.

[11] C.K. Schoff, "Organic coatings: the paradoxical materials," Progress in Organic Coatings, Vol. 52, Iss. 1, 1 January 2005,pp. 21-27.

[12] E.W. Flick, Prepaint Specialties and Surface Tolerant Coatings. New Jersey: William Andrew Publishing/Noyes, 1991.

[13] Rust-Oleum Corporation, Technical Data Sheet - 248941 AUTORF SSPR 6PK ENGINE CHEVY ORANGE. Downloaded 5/25/12, Available at: http://www.rustoleum.com/CBGResourceCenter.asp?sn=ms2&msdstyp=PROCBG&msdsprc=372

[14] D. Stoye, W.Freitag, and G.Beuschel , Resins for Coatings: Chemistry, Properties, and Applications, Germany: Hanser Gardner Publishing, 1996.

[15] Rust-Oleum Corporation, Material Safety Data Sheet - 248941 AUTORF SSPR 6PK ENGINE CHEVY ORANGE. Downloaded 5/25/12, Available at:

http://www.rustoleum.com/CBGResourceCenter.asp?sn=ms2&msdstyp=PROCBG&msdsprc=372

[16] R. van Gorkum, and E. Bouwman, "The oxidative drying of alkyd paint catalysed by metal complexes," Coordination Chemistry Reviews, Vol. 249, Iss. 17–18, September 2005, pp. 1709-1728, 2005.

[17] D.C. Duffy, J.C. McDonald, O.J.A. Schueller, and G.M. Whitesides, "Rapid prototyping of microfluidic systems in poly(dimethylsiloxane)," *Anal. Chem.* **70** 4974-84, 1998/

[18] S. J. Hwang *et al*.," Dry etching of polydimethylsiloxane using microwave plasma," Journal of Micromechanics and Microengineering,19 095010, 2009.

[19] K.W. Meacham, R.J. Giuly, L. Guo, S. Hochman, S.P. DeWeerth, "A lithographically-patterned, elastic multi-electrode array for surface stimulation of the spinal cord," Biomed Microdevices, 10(2) pp. 259-269, 2008.

[20] J. Garra, T. Long, J. Currie, T. Schneider, R. White, M. Paranjape, "Dry Etching of Polydimethylsiloxane for Microfluidic Systems", Journal of Vacuum Science and Technology, A20, pp. 975-982, 2002.

[21] S.R. Oh, "Thick single-layer positive photoresist mold and poly(dimethylsiloxane) (PDMS) dry etching for the fabrication of a glass–PDMS–glass microfluidic device," *J. Micromech. Microeng.* **18** 115025, 2008.

[22] J. Baker-Jarvis, *et al*. (2004) Measuring the Permittivity and Permeability of Lossy Materials: Solids, Liquids, Metals, Building Materials, and Negative-Index Materials. NIST Technical Note Volume, 149

[23] L.M. Sewall, “Dielectric Characterization: A 3D EM Simulation Approach,” MS Thesis, Virginia Polytechnic Institute and State University, 2006.

[24] F.T. Ulaby, Fundamentals of Applied Electromagnetics. 2001, Upper Saddle River, NJ: Prentice Hall. 433.

[25] Agilent Technologies, “Application Note: Basics of Measuring the Dielectric Properties of Materials.” 2005, Agilent Technologies, Inc.: U.S.A.

[26] T.T. Grove, M.F. Masters, and R.E. Miers, “Determining Dielectric Constants Using a Parallel Plate Capacitor,” American Journal of Physics, 2005. 73(1): pp.52-56.

[27] Agilent Technologies, “Agilent E4980A Precision LCR meter User’s Guide.” 2007, Agilent Technologies, Inc.: U.S.A.

[28] Specialty Coating Systems "SCS Parylene Properties," 2010.

[29] Dupont Corporation, “Dupont Kapton Polyimide Film General Specifications, Bulletin GS-96-7”. http://www.dupont.com/kapton/general/H-38479-4.pdf

Chapter 5

[1] D. Huang, F. Liao, S. Molesa, D. Redinger and V. Subramanian, “Plastic-Compatible Low Resistance Printable Gold Nanoparticle Conductors for Flexible Electronics,” *J. Electrochemical Society,* 150, pp. G412–G417, 2003.

[2] S.E. Molesa, “Ultra-Low-Cost Printed Electronics,” Ph.D. Dissertation, U.C. Berkeley, 2006.

[3] S.H. Ko, *et al*., "All-inkjet-printed flexible electronics fabrication on a polymer substrate by low-temperature high-resolution selective laser sintering of metal nanoparticles," Nanotechnology 18,345202, 2007.

[4] M.J. Coutts, M.B. Cortie, M.J. Ford, and A.M. McDonagh, "Rapid and Controllable Sintering of Gold Nanoparticle Inks at Room Temperature Using a Chemical Agent," The Journal of Physical Chemistry C 2009 113 (4), 1325-1328

[5] Sun, S.; Mendes, P.; Critchley, K.; Diegoli, S.; Hanwell, M.; Evans, S. D.; Leggett, G. J.; Preece, J. A.; Richardson, T. H.Fabrication of Gold Micro- and Nanostructures by Photolithographic Exposure of Thiol-Stabilized Gold Nanoparticles *Nano Lett.* **2006**, 6, 345–350

[6] S. Fuller, E.J. Wilhelm, and J.M. Jacobson, "Ink-Jet Printed Nanoparticle Microelectromechanical Systems," *J. Microelectromechanical Systems*, 11 (54), pp. 54-60, 2002.

[7] H. Wang, L. Huang, Z. Xu, C. Xu, R.J. Composto, and Z. Yang, "Sintering Metal Nanoparticle Films,"Flexible Electronics and Displays Conference and Exhibition, 2008, pp. 1-3.

[8] Seonhee Jang, Jaewoo Joung, Yongsoo Oh, Microstructure changes in nanoparticulate gold films under different thermal atmospheres and the effects on bondability, Acta Materialia, Volume 57, Issue 18, October 2009, Pages 5613-5620

[9] M. Jose-Yacama, C. Gutierrez-Wing, M. Miki, D.-Q. Yang, K. N. Piyakis, and E. Sacher, "Surface Diffusion and Coalescence of Mobile Metal Nanoparticles," J. Phys. Chem. B 2005, 109, 9703-9711

[10] K.E.J. Lehtinen and M.R. Zachariah, "Effect of coalescence energy release on the temporal shape evolution of nanoparticles," PHYSICAL REVIEW B, VOLUME 63, 205402

[11] T. Hawa, M.R. Zachariah, ”Coalescence kinetics of unequal sized nanoparticles,” J Aerosol Sci 2006;37:1.

[12] S. Arcidiacono, N.R. Bieri, D. Poulikakos, C.P. Grigoropoulos," On the coalescence of gold nanoparticles," International Journal of Multiphase Flow 30 (2004) 979–994

[13] H.B. Liu, M. José-Yacaman, R. Perez, J.A. Ascencio, "Studies of nanocluster coalescence at high temperature," Applied Physics A: Materials Science & Processing, Vol. 77, Iss. 1 pp. 63-67, 2003.

[14] H. Röder, E. Hahn, H. Brune, J.-P. Bucher and K. Kern ,” Building one- and two-dimensional nanostructures by diffusion-controlled aggregation at surfaces,” Nature 366, 141 - 143 (11 November 1993)

[15] M.L. Eggersdorfer, D. Kadau, H.J. Herrmann, and S.E. Pratsinis, “Multiparticle Sintering Dynamics: From Fractal-Like Aggregates to Compact Structures,” Langmuir 2011 27 (10), 6358-6367

Chapter 6

[1] H.Wohltjen and A. W. Snow, “Colloidal Metal−Insulator−Metal Ensemble Chemiresistor Sensor,” Analytical Chemistry 1998 70 (14), 2856-2859

[2] E. Chow, J. Herrmann, C.S. Barton, B. Raguse,and L. Wieczorek, “Inkjet-printed gold nanoparticle chemiresistors: Influence of film morphology and ionic strength on the detection of organics dissolved in aqueous solution,” Analytica Chimica Acta, vol. 632, iss. 1, pp. 135-142, 2009.

[3] Y. Joseph, A. Peić, X. Chen, J. Michl, T. Vossmeyer, and A. Yasuda,“ Vapor Sensitivity of Networked Gold Nanoparticle Chemiresistors: Importance of Flexibility and Resistivity of the Interlinkage,” The Journal of Physical Chemistry C 2007 111 (34), 12855-12859

[4] S.L. Leung, M. Li, F.T. Lau, and W. J. Li, "Fabrication of Gold Nano-Particle Based Sensors Using Microspotting and DEP Technologies," Proceedings of SICE Annual Conference 2008, The University Electro-Communications, Japan, August 20-22, 2008, pp.3031-3037

[5] Keithley, "Four-Probe Resistivity and Hall Voltage Measurements with the Model 4200-SCS", App. Note 2475, 2002.

[6] C.-H. Cho , R. C. Jaeger , J. C. Suhling , Y. Kang and A. Mian "Characterization of the temperature dependence of the pressure coefficients of n- and p-type silicon using hydrostatic testing", *IEEE Sensors J.*, vol. 8, pp.392 2008.

[7] Yicai Sun, *et al*., "Measurement of sheet resistance of cross microareas using a modified van der Pauw method," Semicond. Sci. Technol. 11 805, 1996.

[8] S. Enderling, C.L. Brown III, S. Smith, M.H. Dicks, J.T.M. Stevenson, M. Mitkova, M.N. Kozicki, and A.J. Walton, "Sheet Resistance Measurement of Non-Standard Cleanroom Materials Using Suspended Greek Cross Test Structures," IEEE Trans. Semiconductor Manufacturing, vol. 19, 1, 2-9, (2006).

[9] M. G. Buehler, S. D. Grant, and W. R. Thurber, "Bridge and van der Pauw sheet resistors for characterizing the line width of conducting layers," J. Electrochem. Soc.: Solid-State Science and Technology, vol.125, no. 4, pp. 650–654, April 1978.

[10] M. JONAS, AND A. PELED, "The equivalent temperature coefficient of resistance of thin film resistor-conductor structures." Thin Solid Films, 90 (1982) 385-390

[11] B. Barwiński, "Temperature coefficient of resistance in discontinuous gold films on sapphire substrate near percolation threshold," Surface Science, Vol. 231, Iss. 1–2, pp. 165-167, 1990.

[12] K.L. Chopra, Thin Film Phenomena (McGraw-Hill, New York, 1969).

Chapter 7

[1] G. M. Rebeiz: "RF MEMS, Theory, Design and Technology," John Wiley & Sons, 2003.

[2] C. Nguyen: “MEMS Technology for Timing and Frequency Control,” IEEE Trans. Ultrason., Ferroelect., Freq. Contr., vol. 54, no. 2, pp. 251–270, Feb. 2007

[3] D. Redinger, R. Farshchi, and V. Subramanian, “Inkjetted passive components on plastic substrate for RFID,” in 2003 IEEE Device Research Conf. Dig., 2003, pp. 187–188.

[4] S. K.Volkman, S.Yin, andV. Subramanian, “Ink-jetted silver/copper conductors for printed RFID applications,” in Proc. 2004 Materials Research Soc. Spring Meeting, vol. 814, Paper I7.8.

[5] L. Yang, A. Rida, T. Wu, S. Basat, and M. M. Tentzeris, "Integration of Sensors and Inkjet-Printed RFID Tags on Paper-based Substrates for UHF “Cognitive Intelligence” Applications," *Antennas and Propagation Society International Symposium, 2007 IEEE* , vol., no., pp.1193-1196, 9-15 June 2007

[6]Li Yang; Rida, A.; Vyas, R.; Tentzeris, M.M.; , "RFID Tag and RF Structures on a Paper Substrate Using Inkjet-Printing Technology," *Microwave Theory and Techniques, IEEE Transactions on* , vol.55, no.12, pp.2894-2901, Dec. 2007

[7] D. Redinger, S. Molesa, S. Yin, R. Farschi, and V. Subramanian, "An Ink-Jet-Deposited Passive Component Process for RFID," IEEE TRANSACTIONS ON ELECTRON DEVICES, VOL. 51, NO. 12, pp. 1978-83, 2004

[8] C.P. Yue, and S.S. Wong, “Physical Modeling of Spiral Inductors on Silicon,” IEEE Transactions on Electron Devices, Vol. 47, No. 3, pp. 560-568,2000.

[9] S.S. Mohan, M. Hershenson, S.P. Boyd and T.H. Lee Simple Accurate Expressions for Planar Spiral Inductances *IEEE Journal of Solid-State*

Circuits, Oct. 1999, pp. 1419-24.

[10] A. Massarini, and M.K. Kazimierczuk, "Self-Capacitance of Inductors," IEEE Transactions on Power Electronics, Vol. 12, No. 4, pp. 671-675, 1997.

[11] H.L. Krauss, C.W. Bostian, and F.H. Raad, Solid State Radio Engineering. New York: John Wiley & Sons, 1980. pg 76

Chapter 8

[1] V. Subramanian, J.M.J. Frechet, P.C. Chang, D.C. Huang, J.B. Lee, S.E. Molesa, A.R. Murphy, D.R. Redinger, and S.K. Volkman, "Progress Toward Development of All-Printed RFID Tags: Materials, Processes, and Devices," *Proceedings of the IEEE* , vol.93, no.7, pp.1330-1338, July 2005

[2] S. Fuller, E.J. Wilhelm, and J.M. Jacobson, "Ink-Jet Printed Nanoparticle Microelectromechanical Systems," *J. Microelectromechanical Systems*, 11 (54), pp. 54-60, 2002.

Appendix A

[1] G. Sberveglieri, ed., Gas Sensors: Principles, Operation and Developments. Boston: Kluwer, 1992.

[2] N. V. Lavrik, M. J. Sepaniak, and P. G. Datskos, "Cantilever transducers as a platform for chemical and biological sensors," Review of Scientific Instruments, vol. 75, pages 2229-2253, 2004.

[3] S. Okuyama, Y. Mitobe, K. Okuyama, and K. Matsushita, "Hydrogen gas sensing using a Pd-coated cantilever," Jpn. J. Appl. Phys., vol. 39, pages 3584-3590, 2000.

[4] F. M. Battiston, J. -P. Ramseyer, H. P. Lang, M. K. Baller, Ch. Gerber, J. K. Gimzewski, E. Meyer, and H. -J. Guntherodt, “A chemical sensor based on a microfabricated cantilever array with simultaneous resonance-frequency and bending readout,” Sensors and Actuators B: Chemical, vol. 77, pages 122-131, 2001.

[5] D.R. Baselt, B. Fruhberger, E. Klaassen, S. Cemalovic, C.L. Britton, S.V. Patel, T.E. Mlsna, D. McCorkle, and B. Warmack, "Design and performance of a microcantilever-based hydrogen sensor," Sensors and Actuators B, vol. 88, pages 120-131, 2003.

[6] J.R. Lacher, "A Theoretical Formula for the Solubility of Hydrogen in Palladium," Proceedings of the Royal Society of London, Series A: Mathematical and Physical Sciences, vol. 161, iss. 907, pages 525-545, 1937.

[7] W-H. Chu, M. Mehregany, and R.L. Mullen, “Analysis of tip deflection and force of a bimetallic cantilever microactuator,” J.Micromech. Microeng. vol. 3, pages 4–7, 1993.

[8] P.J. Shaver, "Bimetal Strip Hydrogen Gas Detectors," The Review of Scientific Instruments, vol. 40, iss. 7, pages 901-905, 1969.

[9] M.B. Bever (ed), Encyclopedia of Materials Science and Engineering, New York: Pergamon Press, page 1059, 1986.

[10] M. Tabib-Azar,and B. Sutapun, "Novel hydrogen sensors using evanescent microwave probes," Review of Scientific Instruments, AIP, vol. 70, iss. 9, pages 3707-3713, 1999.

Appendix B

[1] S.E. Molesa, “Ultra-Low-Cost Printed Electronics,” Ph.D. Dissertation, U.C. Berkeley,2006.

[2] M. Brust, M. Walker, D. Bethell, D. J. Schiffrin, and R. Whyman, “Synthesis of thiol-derivatised gold nanoparticles in a two-phase Liquid-Liquid system.” *Journal of the Chemical Society Chemical Communications* 1994.7 (1994): 801.

[3] M. Hostetler, J. Wingate, C. Zhong, J. Harris, R. Vachet, M. Clark, J. Londono, S. Green, J. Stokes, G. Wignall, G. Glish, M. Porter, N. Evans, R. Murray, "Alkanethiolate Gold Cluster Molecules with Core Diameters from 1.5 to 5.2 nm: Core and Monolayer Properties as a Function of Core Size," *Langmuir,* vol. 14, pp. 17-30, 1998.

[4] D. Huang, F. Liao, S. Molesa, D. Redinger, V. Subramanian, "Plastic-Compatible Low-Resistance Printable Gold Nanoparticle Conductors for Flexible Electronics," *Journal of the Electrochemical Society,* vol. 150, pp. 412, 2003.

Appendix C

[1] R. Saha, and W.D. Nix, *Acta Materialia,*, 50, pp. 23-28, 2002.